Numerical modelling of intrinsic self-healing in fibre reinforced composite structures

Brezetić, Dominik

University of Zagreb

FACULTY OF MECHANICAL ENGINEERING
AND NAVAL ARCHITECTURE

Dominik Brezetić

NUMERICAL MODELLING OF INTRINSIC SELF-HEALING IN FIBRE REINFORCED COMPOSITE STRUCTURES

DOCTORAL THESIS

Zagreb, 2023

University of Zagreb

FACULTY OF MECHANICAL ENGINEERING
AND NAVAL ARCHITECTURE

Dominik Brezetić

NUMERICAL MODELLING OF INTRINSIC SELF-HEALING IN FIBRE REINFORCED COMPOSITE STRUCTURES

DOCTORAL THESIS

Supervisor:
Prof. DSc. Ivica Smojver

Zagreb, 2023

Sveučilište u Zagrebu

FAKULTET STROJARSTVA I BRODOGRADNJE

Dominik Brezetić

NUMERIČKO MODELIRANJE INHERENTNOGA SAMOOBNAVLJANJA U VLAKNIMA OJAČANIMA KOMPOZITNIM KONSTRUKCIJAMA

DOKTORSKI RAD

Mentor:
Prof. dr. sc. Ivica Smojver

Zagreb, 2023.

BIBLIOGRAPHY DATA

UDC:	519.6:620:629.7
Keywords:	intrinsic self-healing, composite structures, multiscale analysis, Rule Of Mixtures, micro-damage, plasticity.
Scientific area:	Technical sciences
Scientific field:	Aeronautical engineering, rocket and space technologies
Institution:	Faculty of Mechanical Engineering and Naval Architecture
Supervisor:	Prof. DSc. Ivica Smojver
Number of pages:	120
Number of figures:	54
Number of tables:	10
Number of references:	97
Date of public defense:	5 June 2023
Committee members:	Assoc. Prof. DSc. Darko Ivančević, University of Zagreb, Croatia Prof. DSc. Tatjana Haramina, University of Zagreb, Croatia Prof. DSc. Vassilis Kostopoulos, University of Patras, Greece
Archive:	Faculty of Mechanical Engineering and Naval Architecture, University of Zagreb

Acknowledgements

First of all, I would like to thank Prof. Smojver for giving me the opportunity to work on the research project which resulted in this thesis. Furthermore, I want to thank him for his guidance through the research journey during which many difficulties were overcome, for his professionalism, kindness and understanding. Second of all, I want to thank Assoc. Prof. Darko Ivančević for all the help with debugging of FORTRAN codes, modelling issues in Abaqus and practical advices given throughout this period. I want to thank my office colleagues Darko, Marijan and Marko for making a great working atmosphere. Then, a big "Thank you!" goes to my spouse Angela for all the understanding, support and love provided during this demanding period. Furthermore, I want to thank all of my friends and colleagues PhD students who I shared with all of my ups and downs. Last, but not the least, I want to thank my family, especially my parents Josip and Ljiljana for giving me the opportunity for higher education and for all the love and support in life, without which none of this would be possible.

I dedicate this thesis to our firstborn - our son Toma.

Preface

I have written this Thesis during my work as a research assistant at the Department of Aeronautical Engineering, Faculty of Mechanical Engineering and Naval Architecture, University of Zagreb. The research activities have been performed employing the knowledge obtained during my undergraduate, graduate, and postgraduate studies at the Faculty of Mechanical Engineering and Naval Architecture and using the cited references. The research presented in this Thesis was supported by the Croatian Science Foundation (HRZZ) within the scientific research project "AdvanCed CompositE Self-healing Simulation" (ACCESS), contract number IP-HRZZ-2018-01-2248, led by Prof. DSc. Ivica Smojver.

Zagreb, March 2023 Dominik Brezetić

Contents

List of Figures

List of Tables

List of Symbols

Abbreviations

3PB Three-Point Bending . . . 10
ATOX Atomic Oxygen Degradation . . . 14
BMI Bismaleimide . . . 9
BVID Barely Visible Impact Damage . . . 4
CDHM Continuum Damage Healing Mechanics . . . 28
CDM Continuum Damage Mechanics . . . 28
CFRP Carbon Fibre Reinforced Polymer . . . 11
DCB Double Cantilever Beam . . . 9
DMA Dynamic Mechanical Analysis . . . 62
EMAA poly(ethylene-co-methacrylic acid) . . . 47
FRP Fibre Reinforced Polymer . . . 1
GCR Galactic Cosmic Rays . . . 14
GFRP Glass Fibre Reinforced Polymer . . . 22
ISOX Isocyanurate-oxazolidone . . . 11
LVI Low Velocity Impact . . . 12
MMOD Micrometeoroids and Orbital Debris . . . 14
PMMA Poly(methyl methacrylate) . . . 15
ROM Rule of Mixtures . . . 8
RP Reference Point . . . 74
SBS Short Beam Shear . . . 11
SMA Shape Memory Alloy . . . 26
SPE Solar Particle Events . . . 14
SPH Smooth Particle Hydrodynamics . . . 90
UD Unidirectional . . . 11
UMAT User-material Subroutine . . . 47
VUMAT User-material Subroutine . . . 67

Summary

This research is focused on development and validation of efficient numerical methodology for modelling of intrinsically self-healing fibre reinforced composite structures. A multiscale approach is used which enables modelling of each constituent and its features at the microscale. For that purpose, the Rule Of Mixtures (ROM) has been employed for the homogenisation, whereas the Voigt (iso-strain) and Reuss (iso-stress) approximations have been used as a means for localisation. The intrinsically self-healing polymer matrix constituent has been modelled as an isotropic material using a micro-damage-healing model and a von Mises linear isotropic hardening plasticity model. The damage variable causes the reduction of the matrix constituent's elasticity modulus whereas the healing variable is responsible for its restoration. The continuous reinforcing fibres have been modelled as transversely isotropic linear elastic material with maximum stress failure criterion and a progressive damage model. The developed constitutive model has been implemented into Abaqus/Standard and Abaqus/Explicit user material subroutines UMAT and VUMAT, respectively. Initially, the model for the pure polymer material has been validated. The cases of uniaxial static tensile loading and two-cycle uniaxial tensile loading have been employed for that purpose. Subsequently, the model of a self-healing composite is validated for static loading conditions using 3PB test results, and for dynamic loading conditions by means of LVI test. Finally, the model is applied to simulation of bird strike damage and healing in composite aircraft wing structure.

Keywords: intrinsic self-healing, composite structures, multiscale analysis, Rule Of Mixtures, micro-damage, plasticity.

Prošireni sažetak

Kod polimera i vlaknima ojačanih polimernih kompozita razlikuju se dva principa samoobnavljanja: ekstrinzični i intrinzični. Kompozitni sustavi sa ugrađenim mikrokapsulama i šupljim vlaknima koja sadrže sredstvo za samoobnavljanje, predstavljaju materijale s ekstrinzičnim svojstvom samoobnavljanja. Drugu skupinu čine materijali s intrinzičnim svojstvom samoobnavljanja kod kojih proces samoobnavljanja započinje uslijed vanjskih pobuda: UV zračenje, toplina itd. Procesi koji uzrokuju samoobnavljanje su posljedica kemijske strukture. Budući da su takvi procesi reverzibilni, moguće je ponavljajuće samoobnavljanje, što ove materijale čini izuzetno perspektivnima. Govoreći o kompozitima s ekstrinzičnim i intrinzičnim svojstvom samoobnavljanja, samoobnavljanje se odnosi na materijal matrice, pri čemu se ono manifestira kao oporavak modula elastičnosti, reduciranog tijekom procesa oštećivanja [Cohades et al., 2018].

U području materijala sa svojstvom samoobnavljanja istraživanja su pretežno usmjerena na eksperimentalna ispitivanja i razvoj novih materijalnih sustava. Supramolekularni polimeri su potvrdili svoju sposobnost zacjeljivanja primjenom u vlaknima ojačanim kompozitima u obliku međuslojeva [Kostopoulos et al., 2016b] na način da je povećana lomna žilavost nakon DCB (engl.: *Double Cantilever Beam*) eksperimenta. U [Gordon et al., 2016] je navedeno nekoliko samoobnavljajućih polimernih mješavina čija je uspješna primjena dokazana zacjeljivanjem kompozitnih ploča nakon balističkih ispitivanja. Primjena plastomernog kopolimera čija se sposobnost samoobnavljanja temelji na Diels-Alder reakcijama je opravdana njihovom upotrebom u obliku međuslojeva u vlaknima ojačanim kompozitima [Kostopoulos et al., 2019]. Pokazano je da se nakon procesa zacjeljivanja povećala lomna žilavost koja je reducirana pojavom delaminacije.

Prethodno spomenuti radovi se bave primjenama samoobnavljajućih polimera u konvencionalnim kompozitima, u obliku međuslojeva ili mješavina polimera. Učinkovitost zacjeljivanja aditivno proizvedenog vlaknima ojačanog kompozita sa kopolimernom matricom je ispitana u [Calderón-Villajos et al., 2019]. Pokazano je da je učinkovitost zacjeljivanja prije i nakon 3D printanja ostala ista. Nekoliko radova bavi se određivanjem mehaničkih svojstava vlaknima ojačanih kompozita s intrinzično samoobnovljivim materijalom matrice. U [Park et al., 2010] je na savijanje u tri točke ispitivan kompozit sa 2MEP4F (engl.: *bis-maleimide tetrafuran*) kao materijalom matrice i jednosmjernim ugljičnim vlaknima. Nadalje, u [Post et al., 2017] i [Feng and Li, 2021] su samoobnavljajući kompoziti zacjeljivani nakon udara malom brzinom. Pokazano je da s porastom energije udara učinkovitost zacjeljivanja opada zbog pojave loma vlakana koja nemaju svojstvo samoobnavljanja. Pri nižim energijama udara je učinkovitost viša, budući je dominantno oštećenje u matrici.

Numeričko modeliranje samoobnavljajućih materijala temelji se na mehanici kontinuuma oštećenja (CDM, engl.: *Continuum Damage Mechanics*). Proširenje CDM-a za primjene na samoobnavljanje je predloženo u [Barbero et al., 2005] gdje je razvijen termodinamički konzistentan konstitutivni model za ekstrinzično samoobnavljajuće kompozite na makro razini. Time su postavljeni temelji CDHM-a (engl.: *Continuum Damage Healing Mechanics*).

Većina konstitutivnih modela dostupnih u literaturi je razvijena ili za asfaltne materijale: [Darabi et al., 2012a], [Davies and Jefferson, 2017], [Sanz-Herrera et al., 2019] ili za polimerne materijale: [Alsheghri and Abu Al-Rub, 2015], [Voyiadjis et al., 2011], [Voyiadjis et al., 2012b]. U [Voyiadjis et al., 2011] je razvijen model za izotropna mikrooštećenja i zacjeljivanje u elastičnom i plastičnom području. Taj model je kasnije nadograđen u [Voyiadjis et al., 2011] dodavanjem funkcije ovisnosti varijabli oštećenja i zacjeljivanja o vremenu i brzini deformiranja. Anizotropne varijable oštećenja i zacjeljivanja su uvedene u [Voyiadjis et al., 2012a].

Znatan broj radova se bavi modeliranjem samoobnavljanja u asfaltnim materijalima. U [Darabi et al., 2012a] je razvijen konstitutivni model oštećenja i zacjeljivanja za linearno elastičan asfaltni materijal, pri čemu je model oštećivanja preuzet iz [Darabi et al., 2011], a iz [Abu Al-Rub et al., 2010] jednadžba za razvoj varijable oštećenja. Spomenuti model je u [Abu Al-Rub and Darabi, 2012] nadograđen viskoelastičnošću i viskoplastičnošću pri čemu je dan detaljan teoretski pregled samog modela.

Numerička implementacija spomenutog modela opisana je u [Darabi et al., 2012b]. Spomenuti radovi promatraju materijal na makro razini, a u [Davies and Jefferson, 2017] je razvijen mikromehanički model za dvofazni asfaltni materijal koji predviđa trajne deformacije uslijed ispunjavanja mikropukotina novo formiranim zacjeljujućim materijalom.

Od modela iz [Barbero et al., 2005], razvijeno je svega nekoliko konstitutivnih modela koji predviđaju pojavu i razvoj oštećenja i zacjeljivanja u kompozitnim materijalima. Jedan od tih modela je predstavljen u [Shabani et al., 2020] koji se koristi za modeliranje inicijacije pukotine i zacjeljivanja iste u kompozitima s intrinzično samoobnavljajućom matricom. Nadalje, u [Udhayaraman et al., 2020] je razvijen višerazinski konstitutivni model koji predviđa pojavu pukotina i njihovog zacjeljivanja u kompozitima s pletenim vlaknima. Konačno, u [Subramanian and Mulay, 2020] je predložen općeniti konstitutivni model za modeliranje oštećenja i zacjeljivanja u samoobnavljajućim materijalima.

Mikromehanički model

U inicijalnoj fazi je razvijen konstitutivni model za čisti polimerni materijal matrice sa svojstvom samoobnavljanja. Pritom je za modeliranje oštećenja odabran model razvijen u [Darabi et al., 2011], jednadžbe 3.58 i 4.3. Za modeliranje zacjeljivanja je odabran model predstavljen u [Abu Al-Rub et al., 2010], definiran jednadžbama 3.94, 4.4 te 4.17 i 4.17. Varijabla oštećenja je ovisna o brzini deformiranja i iznosu deformacije i definirana je skalarnom diferencijalnom jednadžbom. Varijabla zacjeljivanja je također definirana skalarnom diferencijalnom jednadžbom, a ovisna je o vremenu zacjeljivanja pri čemu je omogućeno oštećivanje prethodno zacijeljenog materijala. Također, jednadžbom 4.5 je definirana varijabla efektivnog oštećenja koja opisuje međusobni utjecaj varijabli oštećenja i zacjeljivanja. Nadalje, za opisivanje trajnih deformacija odabran je von Mises model plastičnosti s linearnim izotropnim očvršćenjem, jednadžbe 4.9 i 4.13. Budući je ovaj model namijenjen za višerazinsko modeliranje kompozita, von Mises model plastičnosti je procijenjen kao prikladan. Primjenjivost von Mises modela u ovu svrhu je potvrđena u radovima [Batra et al., 2012, Doghri et al., 2011]. Razvijeni model je validiran statičkim vlačnim i cikličkim vlačnim testovima. Rezultati validacije su prikazani u odjeljku 4.3. poglavlja 4.

Opisani model za materijal matrice je nakon uspješne validacije ugrađen u višerazinsku metodologiju za modeliranje samoobnavljajućih jednosmjernih kompozita. Spomenuti

model je za modeliranje materijala matrice korišten na mikro razini. Ojačavajuća vlakna su modelirana kao transverzalno izotropan linearno elastičan materijal, također na mikro razini. Primijenjeni mikromehanički model je pravilo mješavina. Osim toga, korišten je i kriterij popuštanja temeljen na maksimalnom naprezanju te progresivni model oštećenja za vlakna preuzet iz [Lapczyk and Hurtado, 2007], što je opisano u odjeljku 5.1.1. poglavlja 5. Prijelaz s mikro na makro razinu, tj. homogenizacija je provedena korištenjem izraza pravila mješavina za izračun mehaničkih svojstava homogeniziranog kompozita, odjeljak 5.1.2. poglavlja 5. S druge strane, prijelaz s makro na mikro razinu, tj. lokalizacija je ostvarena korištenjem Voigt (*iso-strain*) i Reuss (*iso-stress*) aproksimacija prema [Goldberg, 1999], odjeljak 5.1.3. poglavlja 5. Za potrebe validacije korišteni su eksperimentalni rezultati iz dostupne literature. Za potrebe validacije u slučaju statičkog opterećivanja iskorišteni su eksperimentalni rezultati savijanja u tri točke, odjeljak 5.2. poglavlje 5., a u slučaju dinamičkog opterećivanja eksperimentalni rezultati udara malom brzinom, odjeljak 5.3. poglavlje 5.

Rezultati

Materijalni model za čisti samoobnavljajući polimer je validiran statičkim vlačnim i cikličkim vlačnim testovima provedenima na Fakultetu strojarstva i brodogradnje, Sveučilišta u Zagrebu, Zavod za materijale, Laboratorij za polimere i kompozite. Statičkim vlačnim testom je validiran model mikro-oštećenja, slika 4.6. Također, na slici 4.7 je prikazan razvoj varijable oštećenja i efektivne plastične deformacije u ovisnosti o ukupnoj deformaciji tijekom statičkog vlačnog testa. Ciklički vlačni test se sastoji od dva ciklusa opterećivanje-rasterećivanje, pri čemu je između ciklusa dozvoljeno zacjeljivanje materijala, slika 4.8 Cikličkim testovima su validirani model zacjeljivanja i plastičnosti, slika 4.8 Model zacjeljivanja je validiran oporavkom modula elastičnosti tijekom procesa zacjeljivanja, koji je mjerljiv tijekom drugog ciklusa opterećivanja. Za validaciju modela plastičnosti je upotrijebljena trajna deformacija ispitnih tijela zaostala nakon prvog ciklusa. Kako bi se postigli navedeni zahtjevi, definiran je skup parametara konstitutivnog modela kojim se postiže podudaranje rezultata analize i eksperimentalnih rezultata. Dodatno, na slici 4.9 je prikazan razvoj varijable oštećenja i varijable efektivnog oštećenja u ovisnosti o ukupnoj deformaciji tijekom cikličkog testa. Slika 4.10 prikazuje razvoj varijable zacjeljivanja i efektivne plastične deformacije u ovisnosti o ukupnoj deformaciji

za vrijeme cikličkog testa.

Konstitutivni model samoobnavljajućeg kompozita je validiran eksperimentalnim rezultatima dostupnima u literaturi. Model je ponajprije validiran za slučaj statičkog opterećivanja korištenjem rezultata eksperimenta savijanja u tri točke, preuzetih iz [Park et al., 2010]. U eksperimentu je upotrebom aluminijske pločice smještene između cilindra za opterećivanje i ispitnog tijela spriječena pojava loma vlakana čime je omogućeno oštećivanje isključivo materijala matrice, slika 5.1 Također, upotrebom pločice spriječeno je i popuštanje kompozita uslijed gnječenja površine cilindrom za opterećivanje. Ispitno tijelo je podvrgnuto trima ciklusa opterećivanja pri čemu je nakon prvog i drugog ciklusa zacijeljeno te je time testirana učinkovitost procesa zacjeljivanja. Odabirom odgovarajućih parametara konstitutivni model je precizno opisao realno ponašanje kompozitnih ispitnih tijela, dobiveno eksperimentom. Rezultati simulacije i eksperimentalni rezultati su uspoređeni u dijagramu sila-pomak, slika 5.3 Na slikama 5.5 i 5.6 su prikazani slojevi kompozitnih ispitnih tijela prije i nakon prvog, odnosno drugog zacjeljivanja. Također, na slici 5.7 je prikazan razvoj modula elastičnosti materijala matrice u konačnom elementu u sredini ispitnog tijela. Nadalje, varijacijom vrijednosti parametara modela oštećenja materijala matrice, prikazan je utjecaj pojedinog parametra na rezultate u dijagramu sila-pomak, slika 5.8. Također, na slici 5.9 su prikazani rezultati dobiveni variranjem vrijednosti parametara modela zacjeljivanja materijala matrice. Ovime je pokazan utjecaj pojedinog parametra na rezultate u dijagramu sila-pomak. Konačno, na slici 5.10 su prikazani rezultati dobiveni variranjem vremena zacjeljivanja. Pokazano je da je u prvom procesu zacjeljivanja efekt procesa zacjeljivanja najveći, a sa svakim idućim ciklusom se smanjuje, odnosno asimptotski teži ka određenoj vrijednosti.

Nakon uspješne validacije za slučaj statičkog opterećivanja, model je validiran za slučaj dinamičkog udarnog opterećivanja. U tu svrhu su iskorišteni eksperimentalni rezultati udara kompozita malom brzinom dostupni u [Cohades and Michaud, 2017b]. U [Cohades and Michaud, 2017b] su kompozitni uzroci sa pletenim staklenim vlaknima udarani sa tri različite brzine udarača koje su rezultirale kinetičkim energijama od 8.5, 17 i 34 J. Nakon udara su pomoću ultrazvuka snimljeni razmjeri oštećenja u pločama. Potom su ploče podvrgnute procesu zacjeljivanja te su ponovno snimljene ultrazvukom da bi se odredila učinkovitost samoobnavljanja. Nadalje, uslijed udara energijom od 34 J došlo je do loma vlakana na gornjoj i donjoj površini ispitnog tijela. Opisani eksperimentalni postupak je reproduciran numeričkim modelom. Mikrostruktura jednog

sloja kompozita sa pletenim vlaknima je aproksimirana s dva sloja jednosmjernih vlakana. Time je omogućena primjena razvijene metodologije i na pletene kompozite. Model oštećivanja i zacjeljivanja matrice je validiran usporedbom oštećenih površina, prije i poslije zacjeljivanja, izmjerenih eksperimentalno i oštećenih površina izračunatih u analizi, slike 5.14 i 5.15. Model oštećivanja vlakana i matrice je dodatno validiran usporedbom kontaktne sile između udarača i ispitnog tijela, slika 5.12. Također, na slici 5.16 je prikazana raspodjela varijable efektivnog oštećenja prije i poslije zacjeljivanja u području udara, za svaku energiju udara posebno. Slika 5.17 prikazuje raspodjelu efektivne plastične deformacije nakon udara, za svaku energiju udara posebno. Konačno, korištenjem kriterija popuštanja temeljenog na maksimalnom naprezanju i progresivnog modela oštećenja, lom vlakana je simuliran u skladu sa eksperimentalnim rezultatima, slika 5.18.

Naposlijetku je, nakon uspješne validacije modela za slučaj statičkog i dinamičkog opterećivanja, simuliran udar ptice u konstrukciju avionskog krila. Analiza je provedena za tri različita udara: (1) frontalno i centralno, (2) frontalno i izvan centra te (3) pod kutom od 30 stupnjeva, slika 5.21. Nakon udara je provedeno zacjeljivanje konstrukcije te je zatim procijenjena učinkovitost zacjeljivanja. Budući u dostupnoj literaturi ne postoje eksperimentalni rezultati zacjeljivanja avionske konstrukcije nakon udara velikom brzinom, ovo istraživanje je numerički eksperiment, temeljen na prethodnoj uspješnoj validaciji modela. Ovim simulacijama su analizirane i prednosti samoobnavljajućih kompozitnih konstrukcija u odnosu na konvencionalne. Na slikama 5.23 i 5.24 je prikazana raspodjela varijable efektivnog oštećenja materijala matrice u konstrukciji krila. Dodatno, na slici 5.25 je prikazana raspodjela iste varijable u poprečnom presjeku krila. Ovi rezultati su kvantificirani dijagramom na slici 5.26 koji prikazuje učinkovitosti zacjeljivanja za dvije različite granične vrijednosti varijable efektivnog oštećenja, $\phi_{eff} < 0.1$ i $\phi_{eff} < 0.05$. Učinkovitosti su računate korištenjem jednadžbe 1.1 pri čemu su vrijednosti f zamijenjene brojem konačnih elemenata sa vrijednošću ϕ_{eff} unutar zadanih granica. Osim oštećenja u matrici, prisutno je i oštećenje vlakana što je prikazano na slici 5.28. Rezultati pokazuju da su slojevi sa orijentacijom vlakana pod 0 stupnjeva najosjetljiviji na udarna oštećenja.

Zaključak

U ovoj disertaciji je za modeliranje samoobnavljajućih vlaknima ojačanih kompozita razvijena višerazinska metodologija temeljena na mikromehaničkom modelu pravilo mješavina. Na mikro razini je materijal matrice modeliran korištenjem von Mises modela plastičnosti sa linearnim izotropnim očvršćenjem, modelom mikro-oštećenja ovisnim o brzini deformiranja i modelom zacjeljivanja oštećenja. Vlakna su modelirana kao linearno elastičan transverzalno izotropan materijal sa kriterijem popuštanja temeljenim na maksimalnom naprezanju i progresivnim modelom oštećenja. Namjena razvijene višerazinske metodologije je predviđanje zacjeljivanja u vlaknima ojačanim polimernim kompozitnim materijalima sa svojstvom samoobnavljanja. Zacjeljivanje ovdje podrazumijeva oporavak modula elastičnosti materijala matrice, koji je degradiran oštećenjem.

Razvijena metodologija je uspješno validirana za slučaj statičkog i dinamičkog (udarnog) opterećivanja kompozitnih konstrukcija, pri čemu je prethodno validiran model za čisti polimerni materijal matrice sa svojstvom samoobnavljanja. U svrhu validacije korištena su tri različita samoobnavljajuća polimera - Surlyn 8940 pri validaciji modela za čisti polimer, bis-maleimide tetrafuran (2MEP4F) pri statičkoj validaciji modela za kompozit te poly(ε-caprolactone) (PCL) pri dinamičkoj validaciji modela za kompozit. U sva tri slučaja validacija je uspješno provedena. Slijedom toga je zaključeno da je razvijeni model fleksibilan po pitanju primjenjivosti na različite materijale matrice. Nadalje, korištene su i dvije različite vrste ojačavajućih vlakana - jednosmjerna ugljična vlakna pri statičkoj validaciji modela za kompozit i pletena staklena vlakna pri dinamičkoj validaciji modela za kompozit. Odziv konstrukcije sa pletenim staklenim vlaknima je precizno simuliran aproksimacijom jednog sloja pletenih vlakana sa dva sloja jednosmjernih vlakana. Konačno, može se zaključiti da se određivanjem odgovarajućih parametara konstitutivnog modela i uvođenjem odgovarajućih aproksimacija, razvijeni model može koristiti za preciznu procjenu oštećivanja i zacjeljivanja samoobnavljajućih vlaknima ojačanih polimernih kompozita.

Slijedom navedenoga, u sljedećoj fazi je razvijeni konstitutivni model primjenjen na modeliranje oštećenja tijekom udara ptice u konstrukciju kompozitnog avionskog krila te na modeliranje zacjeljivanja oštećenja nastalih tijekom udara. U tu svrhu su analizirana tri slučaja udara modela ptice u krilo, kao što je ranije navedeno. Analizama je pokazano da su na udarna oštećenja najosjetljiviji slojevi sa orijentacijom vlakana

pod 0 stupnjeva te je zaključeno da se pri konstruiranju takvih konstrukcija treba voditi računa o rasporedu slojeva. Nadalje, pokazano je da se zacjeljivanjem konstrukcije postižu učinkovitosti zacjeljivanja 96-98 % za slučaj frontalnog udara, odnosno 79-87 % za slučaj udara pod kutom od 30 stupnjeva.

Samoobnavljajući kompoziti pokazuju velik potencijal za primjenu u zrakoplovnim i svemirskim konstrukcijama obzirom da mogu autonomno locirati i zacijeliti mikrooštećenja poput: BVID (engl.: *Barely Visible Impact Damage*), delaminacije i popuštanje matrice. Daljnji razvoj samoobnavljajućih kompozita i njihovih primjena mogao bi značajno doprinijeti sigurnosti zrakoplovnih konstrukcija, ali i revolucionarizirati metode njihovog održavanja. Važnu ulogu u tome imat će pouzdan i precizan konstitutivni model za samoobnavljajuće materijale, budući će omogućiti raznovrsna ispitivanja zrakoplovnih i svemirskih konstrukcija bez potrebe za velikim brojem eksperimentalnih testova.

Razvijena metodologija se pokazala pouzdanom u predviđanju oštećivanja i zacjeljivanja u vlaknima ojačanim polimernim kompozitima sa svojstvom samoobnavljanja. Pritom su korišteni modeli zacjeljivanja i oštećivanja ovisni o vremenu i brzini deformacije. Nadalje, u modelu je pretpostavljeno da se oštećivanje i zacjeljivanje ne mogu događati istovremeno. Kao što je i ranije spomenuto, na procese oštećivanja i zacjeljivanja u polimerima i vlaknima ojačanim polimernim kompozitima utječu brojni faktori. Zacjeljivanje ponajviše ovisi o tlaku i temperaturi, zbog čega je implementacija ovisnosti modela o tim parametrima izuzetno važna. Da bi se odredio odgovarajući model ovisnosti o tlaku i temperaturi potrebna su opsežna eksperimentalna istraživanja za promatrani polimer. Nadalje, potrebno je ispitati i pretpostavku da se oštećivanje i zacjeljivanje ne događaju istovremeno. Za daljnja unaprjeđenja modela potreban je velik broj eksperimenata kako bi se kvantificirali utjecaji određenih parametara.

Dodatno proširenje razvijene metodologije jest simulacija zatvaranja i zacjeljivanja pukotine nastale uslijed proboja. Ovo je od posebnog interesa za primjene u modeliranju balističke zaštite i zaštite od udara svemirskih krhotina.

Konačno, u ovoj disertaciji su postavljeni opsežni temelji za daljnje istraživanje u području numeričkog modeliranja vlaknima ojačanih polimernih kompozitnih konstrukcija sa intrinzičnim svojstvom samoobnavljanja. Spomenuto područje je golemo i neistraženo, obzirom da postoji veoma ograničen broj znanstvenih radova na tu temu. Primjene samoobnavljajućih kompozitnih materijala su brojne. Jedna od takvih primjena je i

u konstrukciji avionskog krila, slučaj analiziran u ovoj disertaciji. Brojem primjena određene su i prilike kao i potrebe za unaprjeđenjem razvijene metodologije.

Cilj i hipoteza istraživanja

Cilj istraživanja je razvoj i validacija konstitutivnog modela za modeliranje razvoja oštećenja i procesa inherentnog zacjeljivanja u vlaknima ojačanim polimernim kompozitnim konstrukcijama.

Hipoteza:

Pojava, razvoj i zacjeljivanje oštećenja, u smislu oporavka mehaničkih svojstava narušenih tijekom procesa oštećivanja, u materijalu matrice vlaknima ojačanog polimernog kompozitnog materijala, može se pouzdano odrediti korištenjem razvijenog konstitutivnog modela, a koji u obzir uzima brzinu i iznos deformacije, nastalo oštećenje i vrijeme zacjeljivanja te omogućuje oštećivanje zacijeljenog materijala.

Pregled rada

U prvom, uvodnom poglavlju je opisana motivacija za ovo istraživanje, dan je opsežan pregled literature te su definirani ciljevi i hipoteza istraživanja. Pregledom literature je dodatno potkrijepljena motivacija i ciljevi istraživanja.

U drugome poglavlju je dan pregled materijala sa svojstvom samoobnavljanja te njihove primjene u zrakoplovnoj i svemirskoj tehnici. Pritom su opisani fizikalni procesi na kojima se temelji samoobnavljanje: (1) polimera i vlaknima ojačanih polimernih kompozita, (2) polimernih premaza, (3) metala i legura te (4) kompozita sa keramičkom matricom.

U trećem poglavlju su predstavljene osnove mehanike kontinuuma oštećenja (CDM) te proširenje na mehaniku kontinuuma oštećenja i zacjeljivanja (CDHM). Nadalje, počevši od temelja CDHM-a, prikazan je izvod konstitutivnih jednadžbi za modeliranje oštećenja i zacjeljivanja koje su korištene u ovoj disertaciji.

U četvrtom poglavlju je opisan konstitutivni model za čisti polimer sa intrinzičnim svojstvom samoobnavljanja. Detaljno su opisani svi teoretski aspekti modela, kao i numerička implementacija istog. Konačno, model je validiran prethodno dobivenim eksperimentalnim rezultatima.

Peto poglavlje se bavi modeliranjem vlaknima ojačanog kompozita kojem je matrica intrinzično samoobnavljajući polimer. Detaljan opis modela za matricu je ovdje izostavljen, budući je drugo poglavlje posvećeno upravo tome. Nadalje, opisan je upotrijebljeni mikromehanički model pravilo mješavina, kao i metode lokalizacije i homogenizacije. Nakon opisa metodologije, slijedi validacija razvijenog modela za statički i dinamički slučaj opterećivanja. Nakon validacije, model je primijenjen na simulaciju oštećivanja i zacjeljivanja kompozitnog avionskog krila pri udaru ptice pri brzini od 300 km/h, za tri različite početne konfiguracije.

U posljednjem poglavlju su navedeni zaključci, kao i preporuke za daljnja istraživanja u području modeliranja i primjene vlaknima ojačanih kompozita sa svojstvom samoobnavljanja.

Izvorni znanstveni doprinos

1. Razvoj novog konstitutivnog modela za modeliranje oštećenja i zacjeljivanja kompozitnih konstrukcija izrađenih od vlaknima ojačanih polimera, pri čemu se polimer, tj. materijal matrice, odlikuje svojstvom samoobnavljanja. Razvijeni model uzima u obzir promjenu varijable oštećenja ovisne o brzini i iznosu deformacije, kao i razvoj varijable zacjeljivanja ovisne o vremenu zacjeljivanja, pri čemu je omogućeno oštećivanje prethodno zacijeljenog materijala.
2. Validacija razvijenog konstitutivnog modela za čisti polimer za slučaj statičkog vlačnog i cikličkog vlačnog ispitivanja.
3. Validacija razvijenog konstitutivnog modela za kompozit za slučaj statičkog opterećivanja, savijanja u tri točke.
4. Validacija razvijenog konstitutivnog modela za kompozit za slučaj dinamičkog opterećivanja, udara malom brzinom.
5. Definiranje eksperimentalnih postupaka nužnih za validaciju razvijenog konstitutivnog modela.
6. Simulacija udara ptice i zacjeljivanja nakon udara konstrukcije avionskog krila izrađenog od kompozita sa svojstvom samoobnavljanja. Procjena prednosti primjene samoobnavljajućih kompozitnih konstrukcija u odnosu na konvencionalne.

Ključne riječi: intrinzično samoobnavljanje, kompozitne konstrukcije, višerazinska analiza, pravilo mješavina, mikro-oštećenja, plastičnost.

1 Introduction

The self-healing phenomenon was first discovered in 1836 at the French Academy of Science. It was observed that the calcium hydroxide exuded from the hydrated cement is converted to calcium carbonate when exposed to the atmosphere [Voyiadjis et al., 2020]. In engineering sense, self-healing is the approach that is emulating the biological systems, as they demonstrate the ability to repair their mechanical properties and recover full functionality using their internal resources.

When it comes to polymers and FRP (Fibre Reinforced Polymer) composites, two concepts of healing can be evaluated [Cohades et al., 2018]: extrinsic and intrinsic. Composite materials with embedded microcapsules, hollow fibres, or vascular systems, which contain the self-healing agent, are examples of materials with extrinsic self-healing ability. In Figure 1.1, examples of materials from each category are shown. In capsule-based self-healing materials have the healing agent dormant in isolated capsules until ruptured by damage and released into the damaged zone. However, this is a one-time event since no repeated healing is possible. Vascular materials consist of a two-dimensional mesh of hollow tubes or fibres containing healing agent until damage occurs. The advantage of these systems is that the network may be refilled by an external source or from the other virgin areas of the network, thereby enabling repeatability of the process.

On the other hand, supramolecular polymers [Kostopoulos et al., 2016b], ionomers [Reynolds, 2011] and Diels-Alder based polymers [Kotrotsos et al., 2019] are polymer materials with intrinsic self-healing ability. Intrinsic self-healing ability means that the healing process is triggered by means of external stimulus, e.g.: ultraviolet light, heat etc., and the self-healing mechanism is an integral part of the material. It is

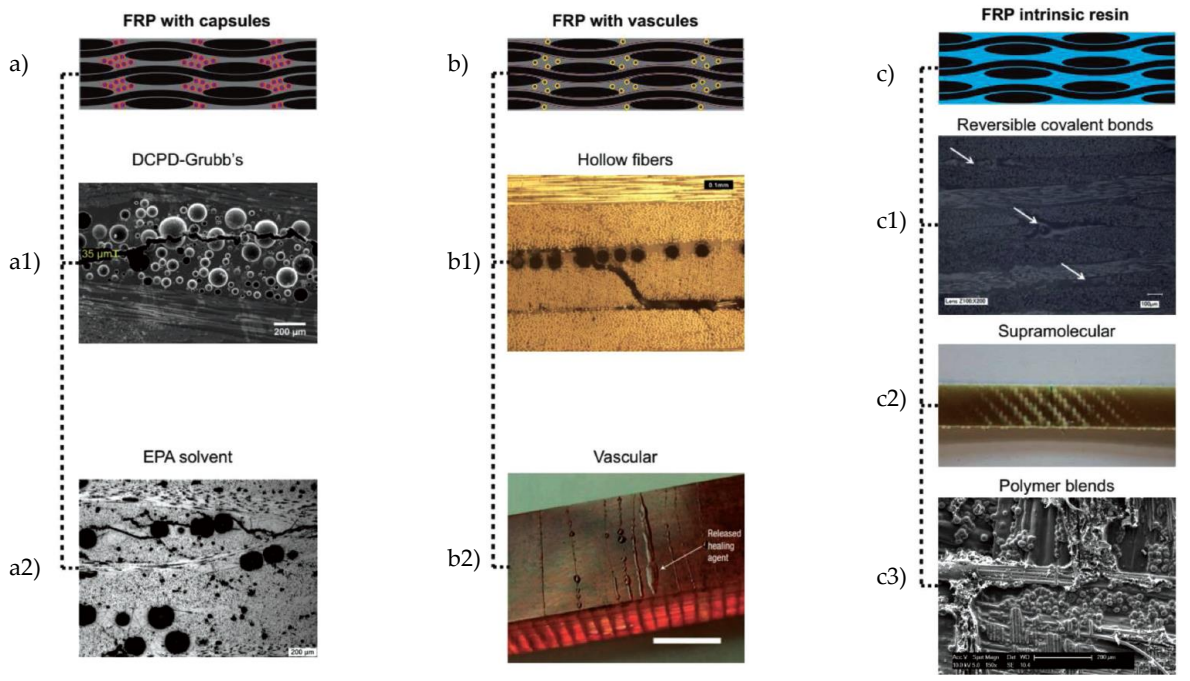

Figure 1.1: Classes of self-healing systems within structural polymer composites: a) capsule-based systems including a1) DCPD–Grubbs' and a2) ethyl phenyl acetate (EPA) solvent capsules; b) vascular systems including b1) hollow fibers and b2) 3D vascular network (scale bar = 5 mm); c) intrinsic healing systems including c1) reversible covalent bonds, c2) supramolecular resins and c3) polymer blends, [Cohades et al., 2018].

achieved through inherent reversibility of bonding of polymer chains. That means that the healing phenomenon results from the processes such as: polymer chain mobility and entanglement, thermally reversible polymerizations, hydrogen bonding, softening of thermoplastic phases, ionic interactions or molecular diffusion. Based on these processes, five types of intrinsically self-healing polymer systems can be evaluated:

- systems based on the reversibility of covalent bonds,
- systems based on supramolecular interactions,
- systems based on polymer blends,
- systems based on ionomeric coupling and
- systems based on molecular diffusion.

Systems based on reversibility of covalent bonds contain components which can be reversibly transformed from the monomeric state to the cross-linked polymeric state in an endothermal process. The most widely utilised are Diels-Alder (DA) and retro

Diels-Alder (rDA) reactions. An example of such polymer is used for healing of carbon fibre reinforced polymer composite in [Kotrotsos et al., 2019]. Systems based on supramolecular interactions are elastomers which are designed to form strong end-group or side-group associations by means of complementary and reversible hydrogen bonds. Supramolecular polymers have proven their healing ability in FRP composites by increasing fracture toughness after double cantilever beam tests in [Kostopoulos et al., 2016b]. Using polymer blends, intrinsic healing of thermoset materials can be achieved. Usually, epoxies are mixed with thermoplastic polymers. Self-healing is achieved by melting and subsequent dispersion of thermoplastic phase in the crack plane and by filling the crack. This type of healing has been approved in [Cohades and Michaud, 2017b] by healing of matrix cracks after low velocity impact tests. Ionomeric self-healing polymers are a class of polymers with ionic segments which are capable of forming clusters that act as reversible cross-links. These clusters can be activated by external stimuli such as heat or UV radiation. Delamination cracks in an FRP composite have been successfully healed by increasing fracture toughness of specimens in [Pingkarawat et al., 2012]. Molecular diffusion can be utilised for achieving intrinsic self-healing in polystyrene and polyurethane gel. For these polymers, dependency of healing process on time and temperature is reported and it occurred during void closure, crack surfaces contact and molecular entanglement between the damaged faces, [Blaiszik et al., 2010]. Since processes responsible for intrinsic self-healing are reversible, repeated healing is possible, what makes these materials highly prospective. Concerning both extrinsic and intrinsic self-healing composite materials, the self-healing behaviour is related only to the matrix constituent, whereas the recovery of fibre mechanical properties is not documented in the literature [Keller and Crall, 2018]. Furthermore, self-healing mostly affects matrix material's mechanical properties by restoring its elasticity modulus reduced due to damage [Cohades et al., 2018].

Finally, it is important to mention that the term *self-healing* should refer only to materials whose self-healing ability is a feature of one material component, i.e. to intrinsically self-healing materials [Fakirov, 2021]. Extrinsically self-healing materials, such as the ones with microcapsules or vascular networks, require two components for the healing process to take place and thus, cannot be referred to as self-healing materials. Instead, the term *chemically assisted healing* should be used according to [Fakirov, 2021].

1.1. Motivation

Demand for lightweight fibre reinforced composite structures has increased in the past few decades. The global market for these materials was valued at $90 billion in 2019 and is expected to grow to $113.6 billion by 2024 resulting from implementation of composites into sporting equipment, automobiles and protective equipment [An et al., 2021]. In aircraft composite structures small cracks and BVID, represent a major issue during maintenance since they are difficult to observe. According to [An et al., 2021], aircraft structural health monitoring and maintenance costs are expected to reach $5.5 billion by 2025. In addition, large-scale damage induced by bird or hail strike presents another issue in maintenance of aircraft structures. Application of self-healing polymer composites could reduce maintenance costs significantly by extending the lifetime of structural components. In Figure 1.2, service lifetime extension of self-healing materials in comparison with traditionally improved materials is schematically depicted in a performance-lifetime diagram. This diagram compares two basic principles of service lifetime extension:

- the traditional approach - improvement of material's initial mechanical properties which leads to enhanced damage tolerance, and
- the self-healing concept - development of materials which can autonomously identify and repair structural damage, thus enabling damage management.

Curve (a) represents an arbitrary material, whereas curve (b) represents its performance after increasing his damage tolerance by moving its damage initiation point further in time. On the other hand, curve (c) represents the material's self-healing alternative which, for the case of FRP composites, can be accomplished by one of the methods described in Figure 1.1. Finally, curve (d) represents a theoretically ideal self-healing material which offers multiple healing processes with no loss of initial mechanical properties.

Space structures represent another sphere of application for self-healing composites. The problem of debris damage in space structures is becoming more and more important, as the number of space vehicles, and thus debris related to their launch, accidental or deliberate destruction, increases. This also produces a number of man-made fragments moving in space at high speed, in addition to natural objects that clash with trajectories of existing space structures. Due to their high orbital velocities, which can reach up to 15 km/s, impacts with space vessels can be fatal for the mission. They can result in penetration of the vessel's skin and the loss of its integrity. To illustrate

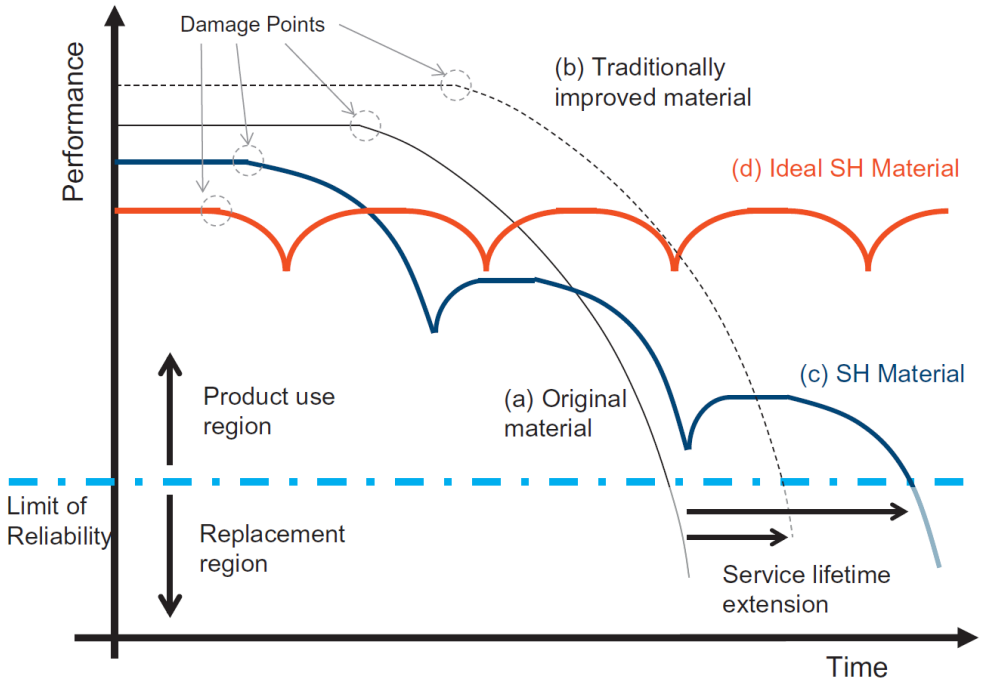

Figure 1.2: Representation of service lifetime extension for self-healing materials compared to traditionally improved materials, [Garcia, 2014].

the gravity of the situation, more than sixty years of space activity have resulted in 56,450 tracked objects in Earth's orbit whose total mass is estimated to 9,300 metric tonnes [European Space Agency, 2021]. Intrinsically self-healing fibre reinforced polymer composites show great potential for space debris impact protection designs since they can autonomously repair structural damage within the composite structure. Matrix material systems such as vitrimers exhibit thermo-mechanical properties close to conventional epoxy resins which makes them highly prospective for aerospace composite designs [Builes Cárdenas et al., 2022].

Self-healing polymers have already proven their applicability in FRP composite materials [Kanu et al., 2019]. For most of self-healing polymers, there is a positive linear correlation between the elasticity modulus and the healing temperature. Thus, a challenge in designing self-healing polymers and composites is in development of material systems with high elasticity moduli and low healing temperatures, Figure 1.3. With such mechanical properties, self-healing polymers could compete with conventional high-performance matrix systems. Their advantage is the ability to autonomously identify and repair potentially dangerous structural damage, which is, in most cases, invisible at the

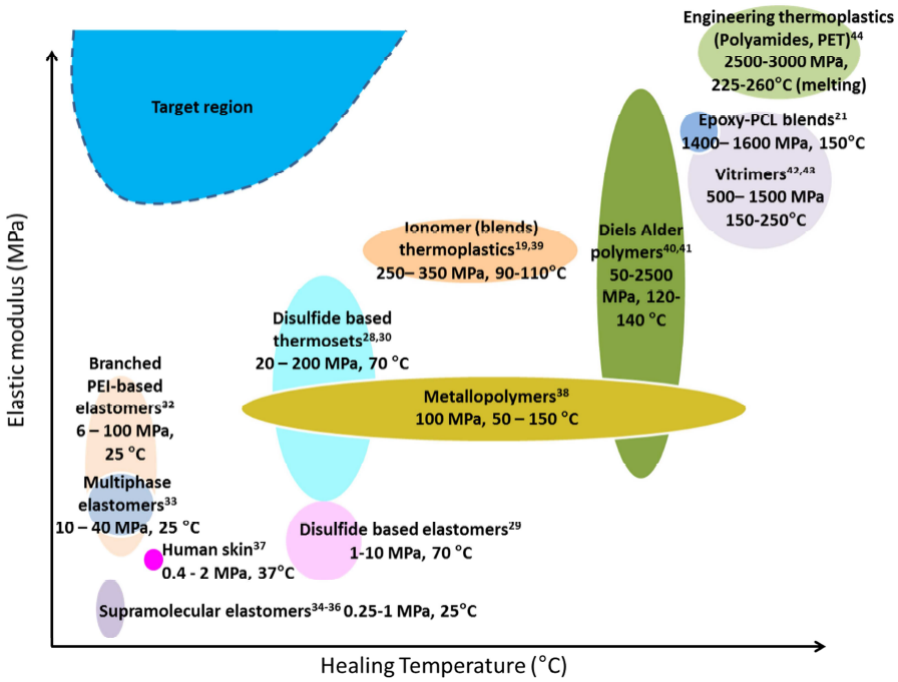

Figure 1.3: Overview of the ratio of elasticity modulus over healing temperature for a range of intrinsically self-healing polymer materials [Post et al., 2017].

surface of the damaged composite material. It occurs, due to a heterogeneous structure, at several length scales (laminate, lamina, fibre-matrix, interface etc.). Occurrence of damage presents a particular problem in the maintenance and operation of composite aeronautical structures which are exceptionally vulnerable to certain types of dynamic loading such as: (i) maintenance damage e.g., tool-induced rupture; and (ii) bird strikes or foreign object damage. These result in various types of damage modes such as:

- fibre breakage,
- matrix failure,
- delamination,
- fibre kinking,
- fibre/matrix debonding and
- BVID.

In [Miqoi et al., 2021] it is shown that at low velocity impacts, matrix cracking occurs first. Therefore, self-healing composite materials are expected to be able to successfully deal with matrix failure, BVID and delamination.

The effect of healing on mechanical properties affected by the healing process is

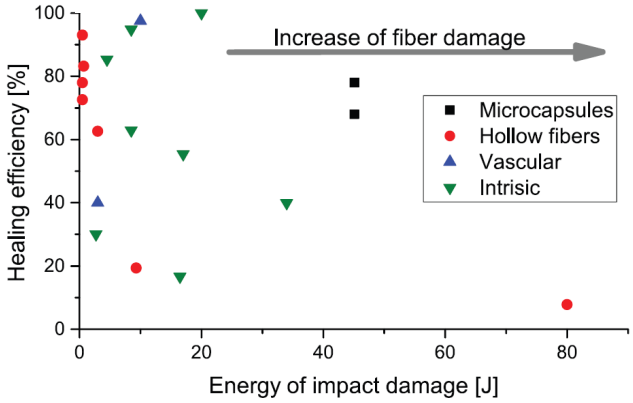

Figure 1.4: Healing efficiency as a function of the impact energy used to initiate damage [Cohades et al., 2018].

described in terms of a healing efficiency, η, which is defined as

$$\eta = \frac{f^{healed} - f^{damaged}}{f^{virgin} - f^{damaged}}, \tag{1.1}$$

where

$f^{damaged}$ is the examined property in the damaged state,

f^{virgin} is the property in the virgin (undamaged) state and

f^{healed} is the examined property in the healed state [Cohades et al., 2018].

Mechanical properties commonly used to quantify the healing efficiency are fracture toughness (mode I), strength (tensile, compressive, impact and flexural), elasticity modulus and strain energy [Paolillo et al., 2021]. However, self-healing systems excel at repairing microcracks. Thus, impact-based experiments are especially convenient for examination of healing efficiency and they are representative of realistic damage states. In [Cohades et al., 2018] it is found that healing efficiency decreases as the impact energy increases. This is because at higher impact energies fibre rupture occurs, see Figure 1.4. Furthermore, in Figure 1.5, dependency of healing efficiency on healing temperature for different intrinsic self-healing systems is given. Moreover, the efficiency is measured after various experimental tests which is also designated in the diagram in Figure 1.5. Efficiencies higher than 100 % can be observed in this diagram. The reason for this is in the type of experimental test, the DCB, and incorporation of the self-healing polymer. Namely, the self-healing agents in these cases were incorporated either as particles or as interlayers in conventional epoxy FRP composites. After the healing and pressurized

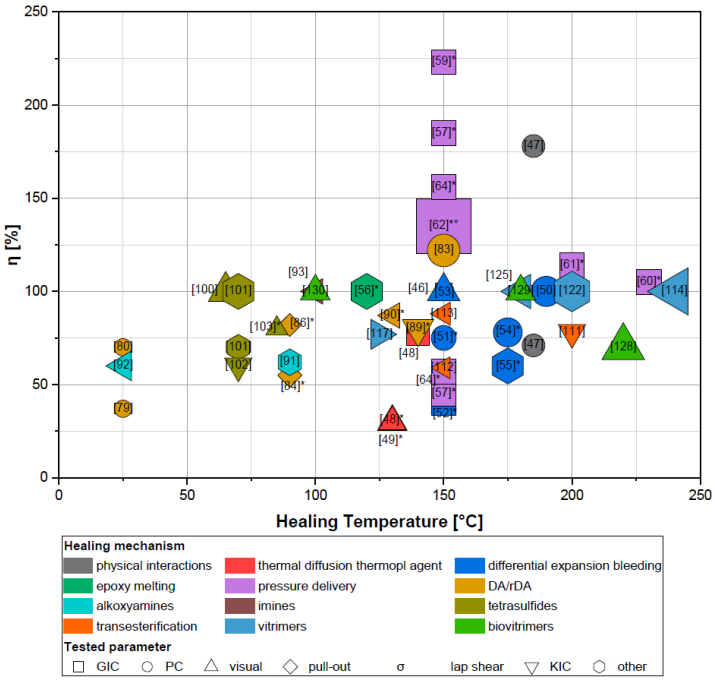

Figure 1.5: Overview of intrinsically self-healing systems, dependency of healing efficiency on healing temperature for different experimental testing procedures - colour coding for the healing mechanism, shape coding for experimental test utilised for assessing healing efficiency, and area inversely correlated with healing time, bigger area = shorter times. The asterisk (*) next to [ref.] indicates that the material is a composite, otherwise, it is a pure polymer, [Paolillo et al., 2021].

thermal activation of the self-healing polymer, the bridging mechanism, Figure 1.6, causes the increase in the fracture toughness.

The constitutive model proposed in this Thesis incorporates von Mises linear isotropic hardening plasticity model, micro-damage and healing variable evolution models for the matrix material, proposed in [Darabi et al., 2012c]. Reinforcing fibres are modelled as linear elastic transversely isotropic material with maximum stress fibre failure criterion and progressive damage model from [Lapczyk and Hurtado, 2007]. Heterogeneous structure of the composite is modelled using a three-dimensional micromechanical model based on the principles of the Rule of Mixtures (ROM). The Rule of Mixtures equations for calculation of mechanical properties of the homogenised composite are used as a means for homogenisation. On the other hand, localisation is carried out using the Voigt iso-strain and Reuss iso-stress approximations for decomposition of total strain increment into fibre and matrix strain increments.

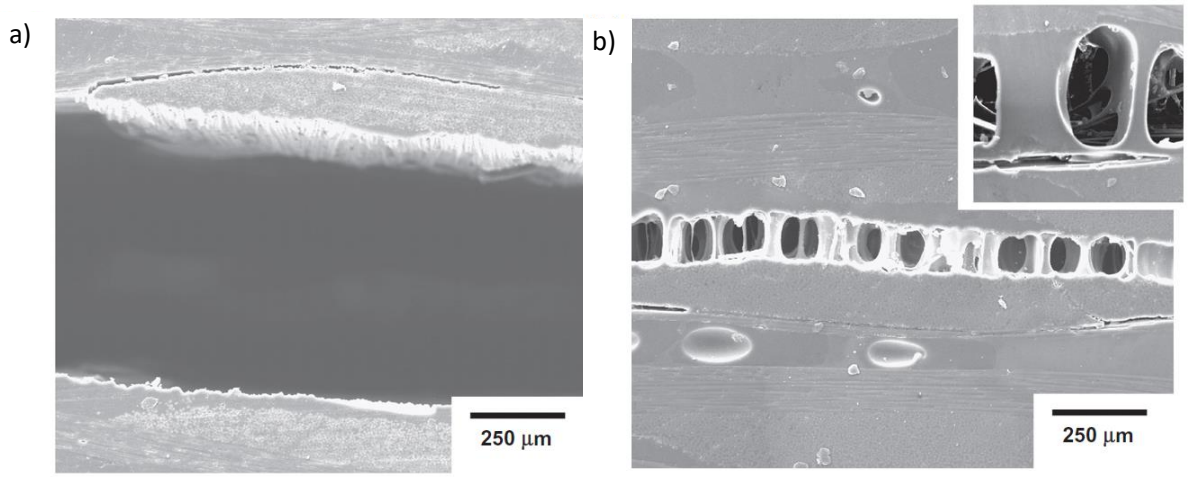

Figure 1.6: Scanning electron microscopy images of the delamination crack in a mendable laminate with interlayers of Surlyn 8940 - a) before self-healing and b) after self-healing, [Pingkarawat et al., 2012].

1.2. Literature overview

Research in the field of self-healing materials is currently predominantly focused on experimental testing and development of novel material systems and self-healing technologies. Supramolecular polymers, integrated in a FRP composite material as an interlayer, have proven their healing ability in [Kostopoulos et al., 2016b] by increasing the fracture toughness after DCB (Double Cantilever Beam) tests. The work in [Gordon et al., 2016] provides an overview of several self-healing polymer blends whose self-healing ability has been proven by healing of plates penetrated during ballistic tests. A Diels-Alder based thermoplastic copolymer is used as a healing agent in form of an interlayer in FRP composite material in [Kotrotsos et al., 2019] and it is shown that it increases the fracture toughness after the evolution of damage, i.e. delamination. In [Pingkarawat et al., 2012] mode I fracture toughness of multi-layered composite materials with interlayers of self-healable Surlyn 8940 copolymer is examined. Figure 1.6 shows the crack bridging ligaments of Surlyn 8940 which cause the increase in fracture toughness after healing and are its direct consequence. The same experiments were conducted in [Kostopoulos et al., 2016a], but here with bismaleimide (BMI) based prepregs. In both works significant increase in fracture toughness is proven after the healing process. In [Da Via et al., 2022] blending of synthetised anionomer

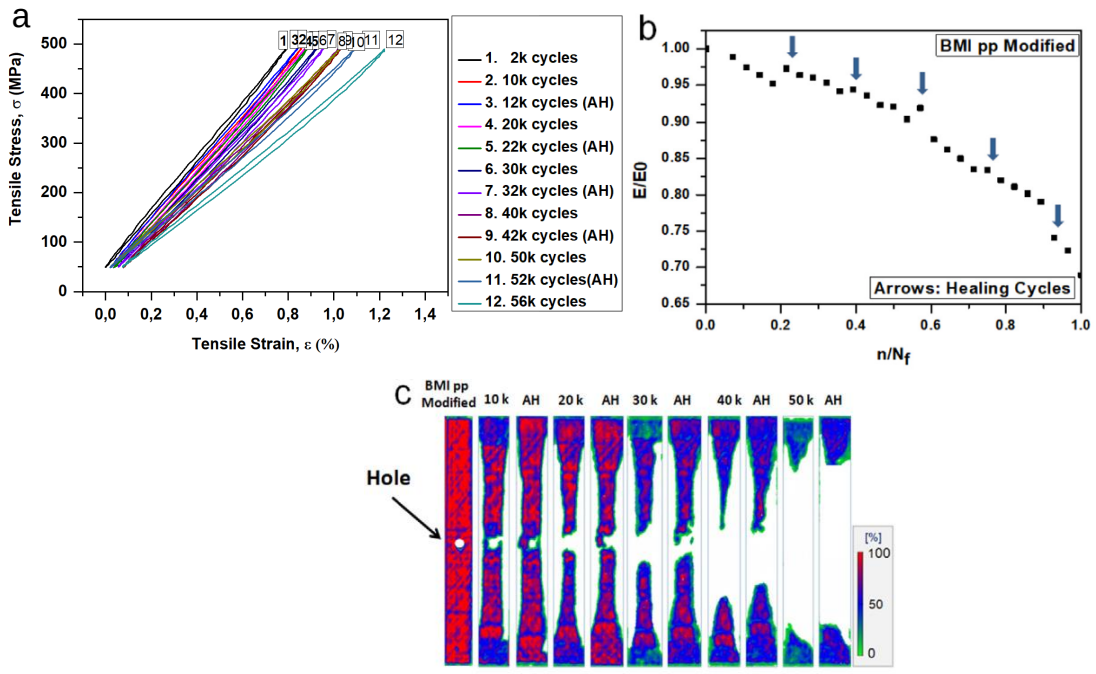

Figure 1.7: Tension-tension fatigue experiments on BMI modified CFRPs with healing periods after every 10,000 cycles; a) First and final hysteresis loops after each consecutive healing period, total of five healing periods, b) elastic modulus ratio evolution, c) C-scan inspection images after each healing period, [Kostopoulos et al., 2019].

and cationomer resulted in a polymer with elastomeric behaviour and extraordinary supramolecular cohesion. Specimens were subjected to tensile tests until rupture. After 1 h of healing at 50 °C, full recovery of tensile strength was achieved. Three Point Bending (3PB) tests are conducted in [Kostopoulos et al., 2018] and it is concluded that healing can be achieved multiple times with high efficiencies. Tensile fatigue tests were carried out in [Kostopoulos et al., 2019], and the research proved that using a self-healing material improves the fatigue life of tensile specimens. Results of that research are given in Figure 1.7 where increase of elastic modulus ratio, hysteresis loops and C-scans of specimens are depicted. Glass fibre reinforced polymer (a blend of epoxy resin and a thermally mending polymer) with self-healing ability was subjected to DCB tests in [Cohades and Michaud, 2017a]. The addition of the self-healing polymer led to significant increase in fracture toughness after the healing process. However, the addition of the self-healing material to conventional composite material can result in lower mechanical properties compared to the conventional composite laminate. That is the case with the shear strength of hybrid composites in [Pingkarawat et al., 2012,

Kostopoulos et al., 2016a, Wang et al., 2012], and with shear strength of composites with epoxy-Surlyn 8940 blend [Azevedo do Nascimento et al., 2020].

The above-mentioned references deal with applications of self-healing polymers in conventional composite structures where they are combined with epoxy matrix systems resulting in composites with self-healing interlayers or polymer blends. In [Calderón-Villajos et al., 2019] the healing efficiency of an additively manufactured FRP composite material with a copolymer matrix is examined and it is shown that the healing process remains equally efficient after the 3D-printing process. Furthermore, a procedure for manufacturing of a FRP composite with Surlyn 8940 copolymer matrix is provided in [Reynolds, 2011]. However, only a limited number of scientific papers have examined mechanical properties of FRP composite structures with matrix constituent being an intrinsically self-healing polymer material. In [Park et al., 2010], CFRP composite specimens are subjected to 3PB tests. Bismaleimide tetrafuran (2MEP4F) is used as the matrix material and UD (unidirectional) carbon fibres are used as reinforcements. The bending load was applied until damage was initiated. Afterwards, specimens were healed during different healing time periods at elevated temperatures. Every specimen was subjected to two healing cycles. Each healing cycle caused increase of the flexural stiffness, measurable in force-displacement diagrams, i.e. the regain of strain energy up to 90 % after the first, and up to 86 % after the second bending cycle. An X-ray micro-tomography model of one of the specimens is given in Figure 1.8 - model of the virgin specimen, specimen after the first bending, and after the healing process is given. Furthermore, the work in [Sordo and Michaud, 2016] deals with experimental testing of self-healing in woven glass FRP composite specimens with supramolecular hybrid network matrix material. Specimens were subjected to 3PB tests and low velocity impact tests. Healing of samples after 3PB tests resulted in recovery of flexural strength of 65 % and in the recovery of bending stiffness of 72 %, after 24 h of healing at room temperature. Mending of impact damage was examined visually, and it proved that complete restoration is reached after 28 days of healing time. Finally, in [Zhang et al., 2018] a CFRP (Carbon Fibre Reinforced Polymer) composite material with novel, intrinsically self-healing isocyanurate-oxazolidone (ISOX) thermosetting matrix material is introduced and subjected to short beam shear (SBS) tests. The polymer exhibits exceptional glass transition temperature of 285 °C which makes it highly prospective for structural applications in aerospace industry. Experiments showed that mechanical strength and

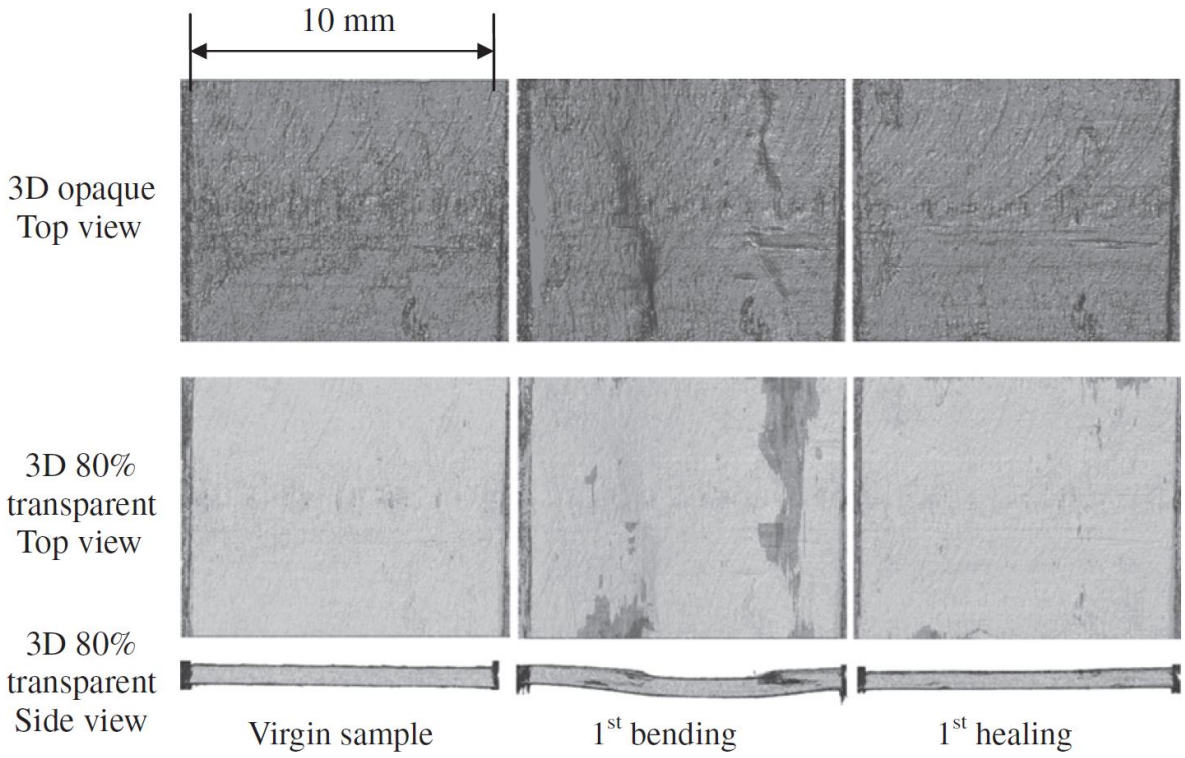

Figure 1.8: A 3D model generated by X-ray micro-tomography representing: virgin composite sample, sample after the first bending, and after the first healing, [Park et al., 2010].

stiffness of this matrix material are comparable with that of a structural grade epoxy matrix. Composite specimens are subjected to short beam shear (SBS) tests, afterwards healed at 200 °C for 12 h. In these experiments, healing efficiencies of 85 % after first healing and 70 % after second healing are achieved. The healing efficiency is measured as the recovery of peak load during the SBS test, compared to the initial peak load. The research has shown that self-healing polymer materials are no longer confined to applications as additions to conventional matrix systems. Moreover, new self-healing polymer compounds are highly prospective to be used as matrix constituents.

Several works deal with LVI (Low Velocity Impact) and post-impact healing of intrinsically self-healing FRP composites. In [Hayes et al., 2007] a novel synthetised thermosetting intrinsically self-healing matrix is combined with UD E-glass fibres to produce specimens for LVI (8 J, 16 J and 30 J impact). Specimens were healed for 2 h at elevated temperature and it resulted in average 50 % healing efficiency, where higher efficiencies are achieved after lower energy impacts, and lower healing efficiencies are achieved after higher energy impacts. The healing efficiency was determined by comparing

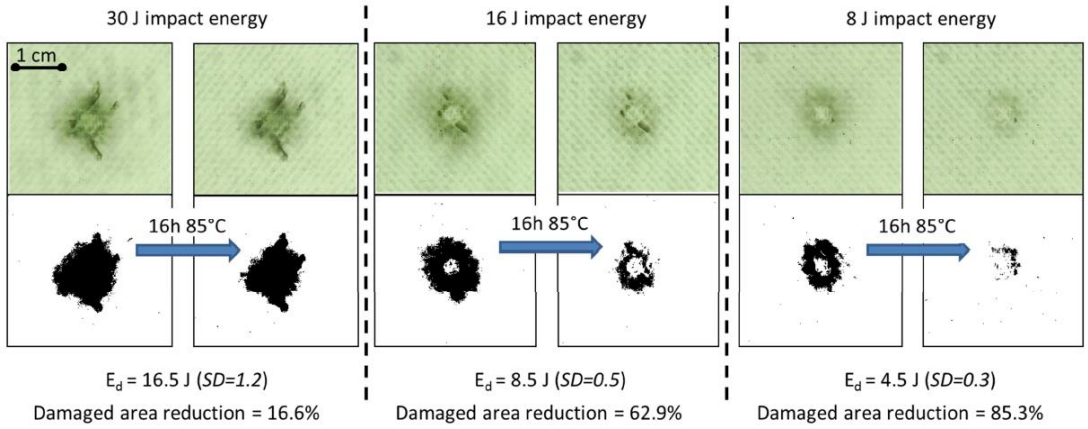

Figure 1.9: Optical analysis of the healing after low-velocity impact for 3 different impact energies. Healing is performed at 85°C and 0.2 bar for 16 hours. Top images show the real damaged composite whereas the bottom pictures show the same pictures treated with a binary filter to facilitate the characterization, [Post et al., 2017].

measured damaged areas. Similar experiments and measurements were conducted in [Post et al., 2017] with another newly developed intrinsically self-healing thermosetting matrix and woven E-glass fibres. For different impact energies (8 J, 16 J and 30 J) it is observed that at higher impact energies healing efficiency is lower since there is a lot of fibre breakage. On the other hand, at lower impact energies matrix damage is dominant, resulting in higher healing efficiencies. This can be concluded from optical inspection images shown in Figure 1.9. Furthermore, in [Cohades and Michaud, 2017b] a compound of conventional epoxy matrix material and 25 vol% poly(ε-caprolactone) is used as a self-healing matrix material with woven E-glass fibres to produce LVI specimens. Three impact energies are used, 34 J, 17 J and 8.5 J. Extent of damage is captured by means of ultrasonic inspection before and after the healing. Documented damage area recovery ranged from 40 % to 90 %. Recently, in [Feng and Li, 2021], where another thermosetting self-healing polymer network is used with woven glass fibres, 84 % healing efficiency is achieved. Specimens were impacted, healed and impacted again. Afterwards, contact forces were compared with unhealed samples to calculate the healing efficiency.

When it comes to devastating debris damage in space structures, there are several approaches to dealing with such phenomena. In [Pernigoni and Grande, 2020] a sandwich structure is proposed, where high strength layers are load bearing and energy absorbing,

while inner pure self-healing polymer layer both seals and heals the impact damage. For that purpose, a supramolecular polymer is combined with aramid fibres and complete sealing and healing is achieved. Finally, in [Kostopoulos et al., 2020] interlayers of self-healing polymer are utilised in conventional fibre reinforced polymer (FRP) composites to repair delamination damage. The aforementioned materials exhibit excellent healing properties. However, they have poor thermo-mechanical properties when compared to conventional epoxy resins. In addition, the space environment is harsh and micrometeoroids and orbital debris (MMOD) present a threat for mechanical integrity of a space structure. Moreover, demands on space structures materials are high since they have to withstand other damaging phenomena such as atomic oxygen degradation (ATOX), galactic cosmic rays (GCR) and solar electromagnetic radiation [Pernigoni et al., 2021]. In low Earth orbit, ATOX can erode the external surfaces of polymers and thus reduce the durability of the structure. However, ATOX is irrelevant in extra-terrestrial i.e., oxygen-free environments. Furthermore, GCR can initiate material degradation and cause the loss of mechanical integrity. Finally, the solar electromagnetic radiation which includes UV rays and solar particle events (SPE) can manifest as volatility, mass-energy loss, reduced mechanical performance and thermo-optical properties. Some self-healing polymers use UV rays as a trigger for the self-healing mechanism and turn a damaging environmental factor into a useful one. Moreover, in [Wang et al., 2018], an ATOX resistant, thermally-stable and self-healing polymer coating is reported which uses ATOX as a trigger for the self-healing mechanism. In dealing with previously mentioned thermo-mechanical properties of usual self-healing polymers, vitrimers represent a perspective alternative. Their mechanical properties are close to conventional epoxy resins, e.g.: $E = 3$ GPa, tensile strength = 75 MPa, as reported in [Builes Cárdenas et al., 2022]. Furthermore, in [Builes Cárdenas et al., 2022] vitrimer's glass transition temperature above 170 °C is reported. This means that it could be able to withstand spacecraft surface temperatures which range from -120 to 120 °C [Pernigoni et al., 2021]. Moreover, their recyclability and ability to autonomously heal structural damage makes them a promising polymer matrix system for production of self-repairable and thus long-lasting and low-maintenance aerospace structures. In [Wang et al., 2021] a vitrimer is combined with woven carbon fabric and the healing efficiency of 76 % is achieved for the case of interlaminar shear strength. Furthermore, in [Paolillo et al., 2021] several vitrimer thermosets suitable for mass production have been reported. Moreover, a bio-based

epoxy vitrimer with glass transition temperature of 187 °C and mechanical properties similar to conventional epoxy networks is reported in [Yang et al., 2020].

Research on numerical modelling of self-healing phenomenon is based on foundations of Continuum Damage Mechanics (CDM), laid in [Kachanov, 1958]. The first broadening of CDM to Continuum Damage Healing Mechanics (CDHM) was proposed in [Barbero et al., 2005]. Inhere, a thermodynamic-based continuum damage-healing constitutive model for modelling of composite materials at the macro-scale with extrinsic self-healing ability (by means of microcapsules) was proposed. The model proposed in [Barbero and Ford, 2007] is an extension of the model proposed in [Barbero et al., 2005], where damage and healing phenomena are experimentally quantified within the context of CDHM at a micro-scale. Motivated by those two models, a number of continuum damage-healing constitutive models have been developed up to now, most of them for pure self-healing materials.

The majority of the CDHM models are developed either for asphaltic and cementitious materials [Darabi et al., 2012a, Davies and Jefferson, 2017, Sanz-Herrera et al., 2019] or for pure self-healing polymer materials [Voyiadjis et al., 2011], [Voyiadjis et al., 2012b] [Alsheghri and Abu Al-Rub, 2015]. In [Voyiadjis et al., 2011] an isotropic micro-damage healing model for shape memory materials in the elastic and plastic regions is developed, and it was later extended in [Voyiadjis et al., 2012b] by adding dependency of damage and healing variables on time and strain rate. Anisotropic properties of damage and healing variables were introduced in [Voyiadjis et al., 2012a]. Moreover, in [Oucif et al., 2019] a super healing theory is presented where the healing phenomenon acts as a strengthening material. In [Alsheghri and Abu Al-Rub, 2015] a cohesive zone healing model for poly(methyl methacrylate) (PMMA) dependent on temperature, resting time and crack closure effect is developed. In [Subramanian and Mulay, 2020] a constitutive model for modelling damage and healing phenomena in self-healing materials in general is proposed. A kinetic coupling is defined between the damage and healing variables using damage strain energy release rate. Model capabilities are presented on one-dimensional cyclic loading cases.

Extensive research has been done concerning numerical models for healing mechanism in asphaltic materials. For instance, a linear elastic micro-damage healing model, incorporating damage variable evolution equation from [Darabi et al., 2011] and the healing variable evolution equation presented in [Abu Al-Rub et al., 2010], was pro-

posed in [Darabi et al., 2012a]. That model was later extended with local viscoelasticity and viscoplasticity in [Abu Al-Rub and Darabi, 2012], with detailed theoretical aspects provided. The numerical implementation of that extended model was described in detail in [Darabi et al., 2012b]. The previously mentioned references described the material at a macrolevel whereas [Davies and Jefferson, 2017] developed a micromechanical model for two-phase asphaltic materials which predicts permanent strains due to the filling of micro-cracks by the newly formed (healing) material. On the other hand, [Sanz-Herrera et al., 2019] introduced a coupled-mechano-chemical-diffusive model where healing is a result of two chemical reactions. In the aforementioned references, the damage and healing variables are usually physically represented as cross-section ratios and their evolution affects the material's elasticity modulus. However, in [Voyiadjis et al., 2020], based on the elastic strain energy equivalence hypothesis, it is shown that the healing variable calculated based on the change in elasticity modulus is greater than the one determined based on the cross-section ratios.

Since the development of the model in [Barbero et al., 2005], only a couple of models which predict damage and healing in polymer composite materials have been developed. First such model is given in [Shabani et al., 2020] which is used for modelling of crack formation and healing in composite materials with intrinsically self-healing matrix material, based on furan and maleimide components. It is an analytical model based on the shear-lag method and the classical lamination theory. This analytical model predicts the residual flexural stiffness of cracked cross-ply laminates as a function of crack density, and the recovered flexural stiffness after thermal treatment, i.e. after the healing process. The proposed analytical model is validated using three-point bending (3PB) tests. In [Udhayaraman et al., 2020], a multi-scale constitutive model that predicts fracture and healing of plain woven textile composites is developed. This model approximates warp and weft yarns as UD plies, where each ply contains half of the original matrix constituent. Applying classical lamination theory on an equivalent cross-ply laminate model, meso-scale failure modes are predicted. Finally, the work in [Subramanian and Mulay, 2020] proposed a constitutive model for modelling damage and healing phenomena in self-healing materials in general. A kinetic coupling is defined between the damage and healing variables using damage strain energy release rate. Model capabilities are presented on one-dimensional cyclic loading cases.

According to the research available in the literature, an appropriate constitutive

model for fibre reinforced composite materials with intrinsic self-healing ability does not exist, thus there is a gap for the research on this topic.

1.3. Objectives and Thesis Hypothesis

The objective of the Thesis is development and validation of a constitutive model for modelling of damage evolution and the process of intrinsic self-healing in fibre reinforced polymer composite structures.

Thesis hypothesis:
Initiation and evolution of damage in a fibre reinforced composite matrix material, as well as the intrinsic self-healing phenomenon i.e., the repair of mechanical properties impaired during the damage process, can be accurately predicted using the developed constitutive model, which takes into account strain rate, strain level, accumulated damage, time during which healing takes place and enables damaging of previously healed material.

1.4. Thesis Outline

In the first, introductory chapter, motivation for this research is given. Furthermore, a thorough literature overview is provided as well as research goals and hypothesis. Motivation and research goals are additionally substantiated by the literature review.

The second chapter is an overview of self-healing materials and their aerospace applications. Thereby, physical processes which cause self-healing in: (1) polymers and FRP composites, (2) polymer coatings, (3) metals and alloys, and (4) ceramic matrix composites, are described.

The third chapter provides basic concepts of Continuum Damage Mechanics (CDM) and its expansion to Continuum Damage Healing Mechanics (CDHM). Furthermore, starting from fundamental relations of CDHM, derivation of constitutive equations for micro-damage and healing used in this Thesis is given.

In the fourth chapter, a constitutive model for pure intrinsically self-healing polymer is described. Theoretical aspects concerning the model are followed by description of numerical implementation of the aforementioned model. Finally, the model is validated with previously obtained experimental results.

The fifth chapter deals with modelling of FRP composites with intrinsically self-

healing matrix material. Detailed description of the matrix constitutive model is here omitted, since it is provided in Chapter four. Furthermore, the applied micromechanical model the Rule Of Mixtures (ROM) and localisation and homogenisation techniques are described. Methodology description is followed by validation of the developed constitutive model, both for static and dynamic loading conditions. Three-point bending test experimental results, available in the literature, are used for validation in static loading cases. In the case of validation for dynamic loading, experimental results of Low Velocity Impact (LVI) test, available in the literature, are used. Finally, after successful validation for both static and dynamic loading cases, the model is applied to simulation of a bird strike and post-impact healing of a self-healing FRP composite aircraft wing structure.

The final chapter provides a conclusion and further research recommendations in the field of numerical modelling of intrinsically self-healing FRP composites.

2 Self-healing materials in aerospace applications

This chapter gives a brief overview and applications of engineering self-healing materials in general, including self-healing polymers, metals and alloys, ceramic matrix composites, FRP composites and coatings. The emphasis in this chapter is on current and future applications of such materials in aerospace structures, especially on self-healing polymers and FRP composites, since they are the topic of this dissertation.

Materials intended for aerospace applications have to meet high requirements due to specific environmental conditions. Apart from space debris impacts, aerospace structures' mechanical integrity is imperilled with both extremely high and extremely low temperatures, atomic oxygen degradation (ATOX), galactic cosmic rays (GCR) and solar electromagnetic radiation [Pernigoni et al., 2021]. Influence of these space environmental factors has been previously described in the introductory part of this Thesis. With respect to service temperature, engineering materials for aerospace applications can be divided into three groups: (1) low temperature, (2) middle range temperature and (3) high temperature applications. Respectively, fibre reinforced polymer composites, metal matrix composites and ceramic matrix composites are used. Potential for application of self-healing materials lies in load bearing structures, engine parts, space debris and impact protection, landing gear etc. which encompass all three temperature categories.

For each material category, firstly principles of self-healing are analysed and afterwards, current and future aerospace applications are discussed.

2.1. Self-healing polymers and FRP composites

As it is already mentioned in the introduction, self-healing polymers, and thus FRP composites, can be classified in two groups: (1) extrinsically and (2) intrinsically self-healing polymers. Extrinsically self-healing polymers and FRP composites are also referred to as autonomously self-healing polymers and composites, since the healing process is initiated by the damage event. On the other hand, intrinsically self-healing polymers and composites need an external stimulus, such as pressure, heat, UV radiation etc., to initiate the healing process. Due to their ability to autonomously repair structural damage, they present a prospective alternative to conventional epoxy-based FRP composites.

FRP composites are nowadays used in structural load bearing applications such as fuselage, wing skin, spar, ribs, flaps etc. For instance, Boeing 787 and Airbus A350 contain up to 50 % of FRP composites by weight, [Rana and Fangueiro, 2016]. Both extrinsically and intrinsically self-healing FRP composites proved their healing efficiency and applicability in structural components. In [Guadagno et al., 2010] microencapsulated epoxy based composite proved its healing efficiency after mechanical load. Hollow glass fibres proved strength recovery after 3PB test in [Teoh et al., 2010]. Furthermore, in [Raimondo et al., 2016], a CFRP with a microcapsule based epoxy resin for low temperature healing applications (-50 °C) is reported. Hail impact tests were carried out with different impact energies: 141 J (41.6 m/s), 118 J (38 m/s) and 70 J (36 m/s). Non-destructive inspection observed no cracks immediately after the impact, which proved a high rate of the healing process. In [Coope et al., 2016] an epoxy resin containing Diels-Alder furan and maleimide moieties applied in FRP composites is reported. The resin heals at elevated temperatures, ca. 150 °C. Due to its good processing properties which enable fibre volume fraction up to 63 %, it is deemed appropriate for use in load bearing aerospace structures where damage during exploitation occurs. Furthermore, in [Park et al., 2010] a bismaleimide tetrafuran based CFRP UD composite showed strain energy recovery of up to 90 % after a 3PB test. Moreover, in [Sordo and Michaud, 2016] visual inspection showed complete recovery of impact damage after 28 days of healing at room temperature.

Example of potential future applications is high velocity impact protection. One such design is proposed in [K. Gordon, R. Penner, P. Bogert, W.T. Yost and E. Siochi, 2011].

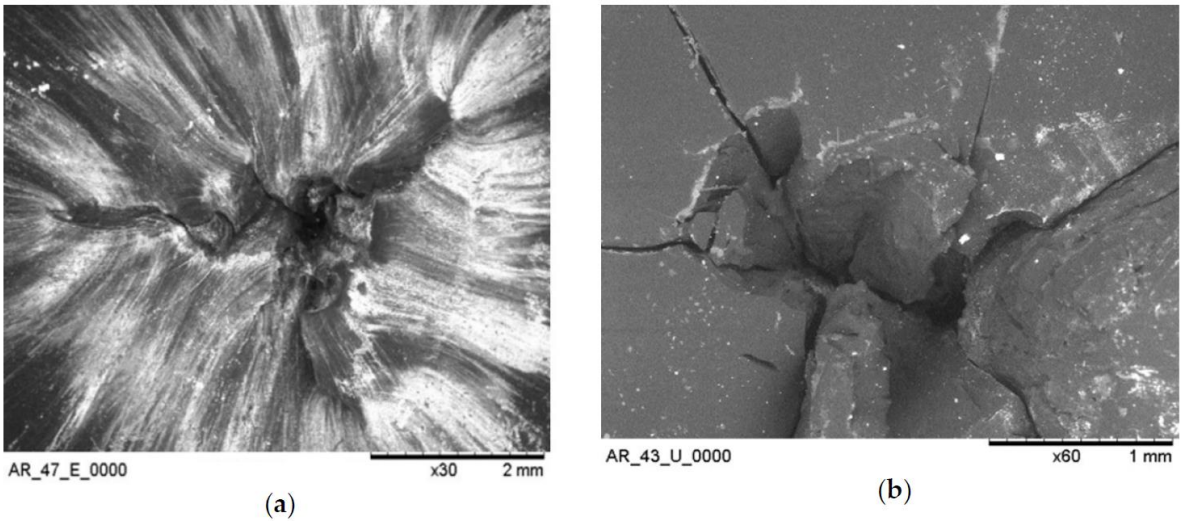

Figure 2.1: Microscopic images of projectile entrance and exit side after two consecutive shots; a) entrance side, b) exit side, [Janszen et al., 2019].

Self-healing and puncture closure is reported after bullet penetration for pure polymer plates made of poly(ethylene-co-methacrylic acid) (EMAA). In the vicinity of the hole, EMAA had been heated up to 98 °C, 3 °C above the melting temperature, which enabled sealing and healing of the hole. Due to poor mechanical properties, EMAA is not considered appropriate engineering material. However, it can be used as an interlayer in multilayered impact protection designs for pressurized vessels, since it is able to seal and heal punctures.

In [Janszen et al., 2019] another high velocity impact protection based on EMAA is proposed. Here potential applications of such material in prevention of fire or explosion due to impact or bullet damage in aerospace fuel tanks is studied. Phenomena during impact and penetration of EMAA plates are investigated in detail. High velocity impact tests were conducted in the temperature range from -40 °C to 70 °C. It is shown that the material is able to properly heal two consecutive shots with 30 s between each penetration. However, microscopic observations have shown that the closure of the hole was a bit worse than in the case of a single shot. Nevertheless, the sample passed the leakage test after the second shot. In Figure 2.1 microscopic images of the projectile entrance and exit side after two shots are given. The second healing was not as good as the first since the thickness of the plate in the impact area was reduced due to the

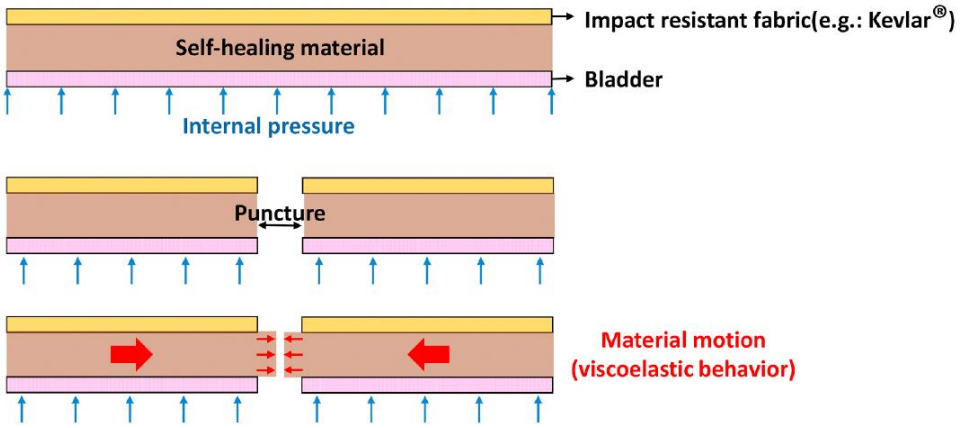

Figure 2.2: Multilayered high velocity impact protection design, a schematic representation, [Pernigoni and Grande, 2020].

previous impact. Thus, a critical ratio of plate thickness over projectile diameter (t/D) is determined and is equal to 0.2. This means that for cases $t/D > 0.2$, healing occurs, and for cases $t/D < 0.2$, healing does not occur. In addition, the samples successfully healed locally, in the vicinity of the impact, even at low temperatures (-40 °C), however, damage and cracks remained permanent in regions further away from the impact zone. Finally, specimens were tested in a pressurized container filled with liquid and the presence of liquid improved the healing efficiency, since it supported deformation recovery during the healing process. Furthermore, coupling of EMAA with solutions for inhibition of tank explosions such as foam or metallic fillers, often used in military aircrafts, is suggested. At high velocity impacts, consequences of damage are divided in two categories: (1) primary damage which is defined by the damage on the target, e.g. hole size, and (2) secondary damage which is defined by damage on neighbouring structures caused by ejected debris. According to [Francesconi et al., 2013], primary damage on ionomeric polymers is found to be significantly lower than on metal alloys, but exhibited poorer performance than metal alloys concerning secondary damage at lower impact velocities. With increase of impact velocity, less debris is produced.

In [Haddad et al., 2019] EMAA is coupled with aramid fibres and a multilayered HVI impact protection design is proposed and validated. Samples were hermetic after the impact. Moreover, in [Post et al., 2017] it is shown that for an epoxy based self-healing GFRP composite, the calculated dissipated energy is more than half of the induced

energy for all impact conditions. These excellent damping properties make this material a perfect candidate for impact protection. With all the aforementioned research on healing of impact damage, it can be concluded that multilayered designs could be used in space suits, habitats and inflatable structures in general. A schematic representation of such a structure is given in Figure 2.2.

To sum up, application of self-healing polymers in multilayered structures with high-strength composite layers with low debris fragmentation is considered highly prospective in aerospace industry.

2.2. Self-healing coatings

Self-healing anti-corrosion coatings are closely related to self-healing polymers, since most of anti-corrosion coatings are based on an organic polymers. Corrosion processes exhibit electrochemical nature, since transfer of charge is the main chemical reaction. That is why polymer coatings are especially interesting for these applications. The anti-corrosive coating system usually comprises several functional layers [Bierwagen and Tallman, 2001]: (1) a pretreatment which ensures good adhesion between the base material and an organic polymer layer; (2) a primer which is a self-healing polymer, intrinsic or extrinsic; and (3) a topcoat responsible for required appearance performance and protection against active corrosive agents. A microscopic image of cross-section of an anti-corrosive polymer coating is depicted in Figure 2.3 where the aforementioned functional layers are visible.

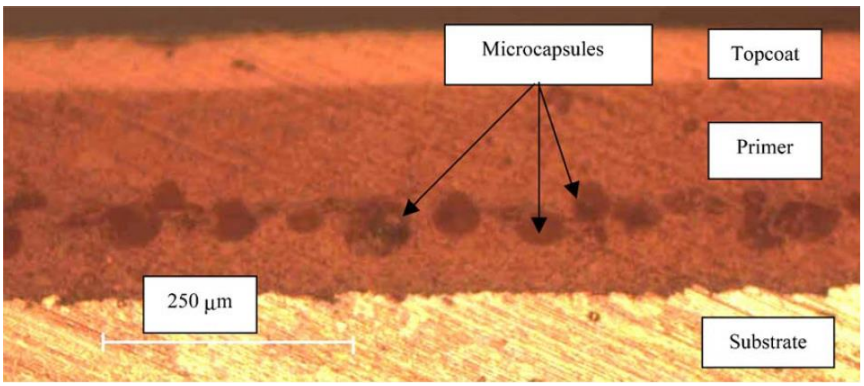

Figure 2.3: Cross-section optical microscopy image of an anti-corrosive polymer coating, [Kumar et al., 2006]

Self-healing polymer coatings find their applications in surface protection of aluminium, magnesium and titanium components which are prone to oxidation when unprotected. Furthermore, they offer protection against minor impacts causing cracks and indentations in coating. In [Zhu et al., 2019] a microcapsule-based self-healing polymer intended for crack repairing of spacecraft coatings is reported. The healing process commences under the stimuli of external force and UV radiation. Furthermore, a special microcapsule-based self-healing polymer coating is reported in [Guo et al., 2016]. The novelty is that both the healing agent and the catalyst are contained in a single microcapsule. Advantages of such approach are that both agents are released into the damaged area simultaneously and that the polymerization for crack-healing can be triggered by an environmental stimulus such as moisture, oxygen, UV radiation etc. This is considered ideal for space environment with intense UV radiation and for low Earth orbit with ATOX. Another application niche for self-healing coatings is electric wiring insulation. For instance, in Space Shuttle Orbiter there is 290 km of wiring installed in the structure of the vessel, which makes it difficult to inspect, [Williams, 2017]. Furthermore, the repair process is intrusive and causes additional damage. In [Williams, 2017], a microcapsule based self-healing epoxy coating for electric wiring insulations is proposed which offers autonomous approach in healing of insulation damage and thus, prevention of short-circuits.

To sum up, there is a wide variety of potential applications of self-healing materials in aerospace industry, ranging from structural load bearing components such as wing shell, flaps, ribs and spars to landing gear, jet engine components, protective coatings and high velocity impact protection. For each of these applications, there is an adequate self-healing material at disposal. Even though they are not commercially present yet, owing it to rapid development by the scientific community, their time is yet to come to revolutionize the aerospace industry.

2.3. Self-healing ceramic matrix composites

Engineering ceramics and ceramic matrix composites are especially interesting for high-temperature applications. However, they tend to have brittle fracture which usually occurs rapidly and leads to catastrophic failure. With ability to heal surface cracks, their lifespan increases. Self-healing mechanism in ceramic matrix composites is enabled by

embedding SiC particles which fill the surface cracks during an oxidation process at high temperatures. The process is characterized by the increase in volume of SiC (approx. 80 %) and generation of enormous exothermic heat which ensures good bonding of the formed oxide and the base material. However, there are certain conditions that have to be fulfilled to enable the healing process. These conditions are: (1) atmosphere, (2) temperature and (3) stress. Concerning the atmosphere, since the healing process is an oxidation process, oxygen is necessary for successful healing. Thus, the healing process is constrained to surface cracks. The second condition is the temperature. According to [Swapan Kumar Ghosh, 2009], to completely heal a semi-elliptical crack of 0.1 mm in surface length within 1 h, a temperature of 1300 °C is necessary. Healing at lower temperatures such as 1200 °C or 1100 °C is possible, but at slower rates - 10 to 300 h. The last condition is the material stress. It is important to be familiarized with the threshold stress above which the crack propagates and leads to failure. Above this threshold stress, healing cannot take place. In [Swapan Kumar Ghosh, 2009] it is shown that specimens healed under applied tensile stress and the ones healed under no stress, at the same temperature, had the same strength.

Nowadays, ceramic matrix composites are preferable material for high temperature applications, such as in advanced aeronautical jet engines. Moreover, they are used as an alternative to expensive nickel-based alloys [Inamuddin et al., 2021]. However, they are still limited to components which are not subject to impacts, i.e. in stationary engine parts, due to their poor crack propagation resistance, [Rana and Fangueiro, 2016]. Nevertheless, utilisation of self-healing ceramic matrix composites could enable applications even in impact exposed conditions and in rotary parts, e.g. turbine blades, due to their improved fatigue and brittle failure resistance. Another condition supporting jet engine applications is that ceramic healing occurs at temperatures characteristic for jet engine combustion chambers, [Paladugu et al., 2022]. Additional high-temperature applications of ceramic matrix composites such as in rocket nozzles, heat engines and braking systems can be improved by extending the service lifetime with utilisation of their self-healing versions. For instance in [Wu et al., 2022], a self-healing carbon fibre reinforced SiBCN(O) ceramic for potential high-temperature applications in aerospace jet engines is reported. Nearly complete crack healing is observed at 1000 °C.

2.4. Self-healing metal matrix composites

With respect to microstructural characteristics of the healing process, healing in metals can be divided in two categories, according to [Swapan Kumar Ghosh, 2009]: (1) liquid-assisted healing, (2) solid-state healing (aluminium alloys and steels). These categories describe the mechanism of transport of the self-healing metal to the damaged zone. Furthermore, self-healing systems can be divided according to their autonomy into: (1) non-autonomous systems, which require heat or electricity and (2) autonomous systems which do not need an external stimulus. However, autonomous systems are still mostly theoretical materials due to the lack of significant experimental results. Thus, the emphasis here is on non-autonomous self-healing systems.

Liquid assisted healing is mainly focused on metal matrix composites reinforced with shape memory alloy (SMA) fibres where the matrix partially liquefies at elevated temperatures. The microstructure of the metal is designed such that it contains a certain fraction of a phase with lower melting temperature. Since partial melting of the matrix material is a repeatable process, theoretically infinite number of healing cycles is available. The process is depicted schematically in Figure 2.4. However, the concept has one limitation and that is the maximum size of the crack that can be healed. This is related to the capillary forces which are crucial for transport of the liquefied phase. Thus, large scale damage, where capillary forces are not strong enough, cannot be healed. One possible solution is to increase the volume fraction of the healing agent, but this would lead to degradation of mechanical properties of the material. In [Michele Viola Manuel, 2007], a Sn-21Bi (wt%) matrix alloy with 1 % of equiatomic

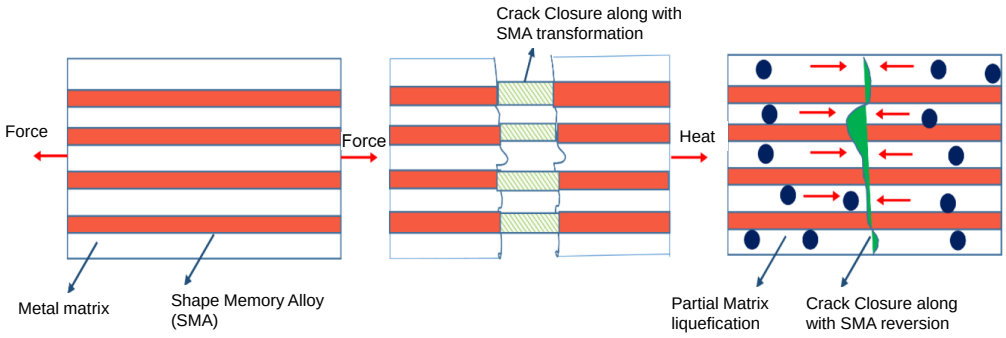

Figure 2.4: Liquid assisted healing in metal matrix composites reinforced with SMA fibres, a schematic representation, [Paladugu et al., 2022].

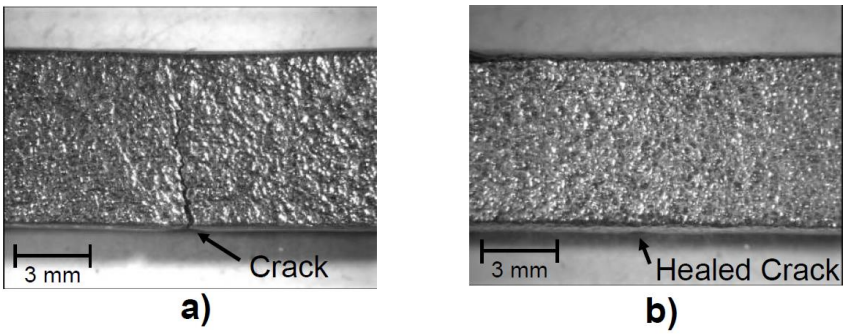

Figure 2.5: Optical microscopy image - healing of a macroscopic crack in Sn-21Bi composite reinforced with NiTi SMA fibres, [Michele Viola Manuel, 2007].

NiTi SMA fibres is presented. The embedding of SMA fibres resulted in 73 % increase in ductility when compared to the unreinforced Sn-21Bi matrix. Furthermore, the reinforced matrix showed 95 % strength recovery after complete matrix failure during a tensile test. Strength was recovered during the healing process at 169 °C for 24 h. In Figure 2.5, optical microscopy image of the Sn-21Bi specimen before and after the healing process is given.

The second approach is the solid-state healing mechanism which is based on the strong driving force for solute diffusion to high-energy areas, such as cracks and voids. This approach is mainly used for aluminium alloys and steels. Diffusion is a chemical process which occurs due to the tendency of minimization of the system energy. The diffusion of atoms through a solid is, however, much slower than through a liquid. Nevertheless, it can occur relatively quickly along high-energy paths such as grain boundaries and dislocations. This healing mechanism has been reported in aluminium alloys by dynamic solute precipitation during creep and fatigue loading in [Lumley et al., 2002].

Metal matrix composites find their applications in compressor blades or landing gear, whose service lifetime can be extended by utilisation of self-healing metal matrix composites. For instance, in [Nakao, 2013] a hybrid metal-ceramic composite for turbine blade applications is reported. The hybrid composite is an aluminium matrix reinforced with aluminium fibres and with interlayers of SiC ceramic as the healing agent. It showed complete strength and stiffness recovery after 1 h of healing at 1,200 °C, which is in the interval of service temperatures for turbine blades.

3 Continuum Damage Healing Mechanics

All engineering materials, including FRP composites, are subjected to unfavourable mechanical and environmental conditions during exploitation. These conditions lead to decrease of mechanical properties such as elasticity modulus, strength, toughness etc., due to the accumulation of microstructural changes. These microstructural changes are referred to as damage. To properly estimate the value of damage, it is necessary to formulate it in terms of mechanics. First such formulation was introduced in [Kachanov, 1958], where creep failure of metal alloys was modelled, which is nowadays considered as the foundation of the Continuum Damage Mechanics (CDM). Continuum Damage Healing Mechanics (CDHM) developed from the CDM, and it was introduced for the first time in [Barbero et al., 2005]. In the following sections, an overview of CDM foundations is provided and it is followed by introduction to CDHM and its general concepts. Afterwards, a detailed description of the micro-damage healing model opted for application to intrinsically self-healing composites in this Thesis is provided.

3.1. Foundations of CDM

In the simplest case the damage variable, ϕ, is a scalar function. In a more complex case, it is a vector function. For introduction to CDM basic formulations, the isotropic scalar damage variable is used. Thus, a certain section of the body is considered where A_0 is the initial area of the undamaged section, and it represents the nominal configuration of the material. As a result of the damaging process, a part of the section is fractured and this fractured area is denoted with A. The value A_0–A is understood as the actual area of the section, and it represents the effective configuration of the material. In case of

isotropic scalar damage variable, cracks and voids are equally distributed in all directions throughout the material. The damage variable is defined as

$$\phi = \frac{A}{A_0} \; ; \; 0 \leq \phi \leq 1, \tag{3.1}$$

and in case of a material with no self-healing ability it is a positive monotonically increasing function, $\dot{\phi} > 0$. It is convenient to introduce the continuity function, ω

$$\omega = 1 - \phi = \frac{A_0 - A}{A_0}, \tag{3.2}$$

which is a positive monotonically decreasing function, $\dot{\omega} < 0 \; ; \; 1 \geq \omega \geq 0$. For an undamaged material, $\phi = 0$, $\omega = 1$, and at fracture $\phi = 1$, $\omega = 0$. For the case of uniaxial tension, the actual stress σ_a can be introduced as

$$\sigma_a = \frac{F}{A_0 - A} = \frac{F}{A_0(1-\phi)} = \frac{F}{A_0\omega} = \frac{\sigma}{\omega}, \tag{3.3}$$

where σ is the nominal stress and σ_a is the actual stress related to the undamaged area of the section, i.e. to the effective configuration, thus

$$\omega = \frac{\sigma}{\sigma_a}. \tag{3.4}$$

It is assumed that the strain of the body is modified by damage through the actual stress solely, and that the evolution of damage is primarily determined by the actual stress. Hence, the stress-strain behaviour of the damaged material can be represented by the constitutive equation of the virgin material (without damage) with stress replaced with the actual stress. The aforementioned demonstrates the significance of the concept of actual stress and nominal and effective configurations. According to this concept the elastic strain of damaged material is defined as

$$\varepsilon = \frac{\sigma_a}{E} = \frac{1}{E}\frac{\sigma}{\omega} = \frac{\sigma}{E'}, \text{ or } \omega = \frac{1}{E}\frac{\sigma}{\varepsilon}. \tag{3.5}$$

Eq. 3.5 is the Hooke's law where $E' = E\omega$ is the damaged elasticity modulus. In the case of an elastic-plastic deformation, when damage is a result of a large strain, it is assumed that damage does not depend on elastic strain, thus

$$\frac{d\omega}{d\varepsilon} = 0, \tag{3.6}$$

which leads to relation $\sigma/\varepsilon = d\sigma/d\varepsilon$. Thus, the continuity function can be expressed as

$$\omega = \frac{1}{E}\frac{d\sigma}{d\varepsilon} = \frac{E'}{E}. \tag{3.7}$$

Eq. 3.7 implies that the damage variable can be estimated by measuring the elastic response where E is the loading and E' is the unloading elasticity modulus.

When considering a linear elastic isotropic body with isotropic scalar damage variable, the thermodynamic parameters of the state are the components of the strain tensor ε_{ij} and the continuity function ω. Furthermore, in isothermal case the density of the Helmholtz free energy is defined as

$$\Psi = \Psi(\varepsilon_{ij}, \omega), \tag{3.8}$$

$$d\Psi = \frac{\partial \Psi}{\partial \varepsilon_{ij}} d\varepsilon_{ij} + \frac{\partial \Psi}{\partial \omega} d\omega. \tag{3.9}$$

In Eq. 3.9, the derivatives $\partial\Psi/\partial\varepsilon_{ij}$ are equal to corresponding conjugate generalized forces, i.e. the components of the stress tensor σ_{ij}. The derivative $\partial\Psi/\partial\omega$ is denoted as $-\bar{Y}$, where $\bar{Y}$ is the conjugate generalized force associated with the damage parameter ω. Thus, Eq. 3.9 can expressed as

$$d\Psi = \sigma_{ij} d\varepsilon_{ij} - \bar{Y} d\omega. \tag{3.10}$$

In elastic material without damage $d\Psi = \sigma_{ij} d\varepsilon_{ij} = dU$, where $U(\varepsilon_{ij})$ is the density of the elastic strain energy. In the damaged state, according to the actual stress concept, the Hooke's law is expressed with damaged Young's modulus $E' = E\omega$ such that

$$\sigma_{ij} d\varepsilon_{ij} = \omega dU. \tag{3.11}$$

In this case

$$\Psi = U\omega \text{ and } \bar{Y} = -U. \tag{3.12}$$

The second term in Eq. 3.10 represents the increment of entropy due to the increment of damage. The second law of thermodynamics requires that

$$\bar{Y} d\omega > 0. \tag{3.13}$$

Since $d\omega < 0$, it implies that $\bar{Y} < 0$. This means that the thermodynamic conjugate force $\bar{Y}$ can be interpreted as the energy release rate caused by the evolution of damage.

This concludes the brief overview of general CDM thermodynamic framework. Eqs. 3.9 and 3.10, i.e. postulation of specific form of the Helmholtz free energy is the starting point of damage modelling in engineering materials. This is also a starting point for inclusion of CDHM concepts, which are described in the following section.

3.2. Foundations of CDHM

As previously mentioned, the first broadening of CDM to CDHM was given in [Barbero et al., 2005]. In this work, FRP composites with extrinsic self-healing ability, healing with microcapsules, are modelled. The proposed formulation is based on generalized thermodynamics, i.e. the constitutive equations are consistent with the Clausius-Duhem inequality

$$\boldsymbol{\sigma} : \dot{\boldsymbol{\varepsilon}} - \rho \left(\dot{\Psi} + s\dot{T} \right) - \frac{1}{T} \nabla \boldsymbol{q} T \geq 0, \tag{3.14}$$

where

$\boldsymbol{\sigma}$ is the stress tensor,

$\boldsymbol{\varepsilon}$ is the strain tensor,

ρ is the mass density,

Ψ is the specific Helmholtz free energy,

s is the specific entropy,

T is temperature and

$\boldsymbol{q}$ is the heat flux.

The term $\boldsymbol{\sigma} : \dot{\boldsymbol{\varepsilon}}$ represents power necessary for elastic deformation of a body. Furthermore, the term $\rho \left(\dot{\Psi} + s\dot{T} \right)$ represents the increase of entropy and the power dissipated on internal processes of the material, such as damaging, inelastic deformation, healing etc. Finally, the term $\frac{1}{T} \nabla \boldsymbol{q} T \geq 0$ represents the transfer of heat. A pure mechanical theory and infinitesimal strains are assumed in the proposed model and the additive strain decomposition is considered consistent with the theory of small strains, i.e. $\varepsilon = \varepsilon^e + \varepsilon^p$. Furthermore, to describe both degradation and healing phenomena, a set of internal variables is introduced.

$$\begin{aligned} \boldsymbol{\varphi}^d &= \boldsymbol{\varphi}^d(\mathbf{D}, \delta), \\ \boldsymbol{\varphi}^p &= \boldsymbol{\varphi}^p(\boldsymbol{\varepsilon}^p, p), \\ \boldsymbol{\varphi}^h &= \boldsymbol{\varphi}^h(\mathbf{H}, \mu), \end{aligned} \tag{3.15}$$

where

$(\mathbf{D}, \boldsymbol{\varepsilon}^p, \mathbf{H})$ are tensorial variables related to damage (d), plasticity (p) and healing (h), respectively,

(δ, p, μ) are scalar variables related to damage (d), plasticity (p) and healing (h), respectively.

Helmholtz free energy, which is a function of both internal and observable variables, can be used to describe the actual thermodynamic state

$$\Psi = \Psi(\boldsymbol{\varepsilon}^e, \boldsymbol{\varphi}^d, \boldsymbol{\varphi}^p, \boldsymbol{\varphi}^h), \tag{3.16}$$

where $\boldsymbol{\varepsilon}^e$ is the admissible elastic deformation set. Substituting Eq. 3.14 into 3.16 the following constitutive equations and thermodynamic forces are introduced

$$\begin{aligned} \boldsymbol{\sigma} &= -\rho \frac{\partial \Psi}{\partial \boldsymbol{\varepsilon}^e}, \\ \boldsymbol{V}^d &= -\rho \frac{\partial \Psi}{\partial \boldsymbol{\varphi}^d}, \\ \boldsymbol{V}^p &= -\rho \frac{\partial \Psi}{\partial \boldsymbol{\varphi}^p}, \\ \boldsymbol{V}^h &= -\rho \frac{\partial \Psi}{\partial \boldsymbol{\varphi}^h}, \end{aligned} \tag{3.17}$$

with

$\boldsymbol{V}^d = \boldsymbol{V}^d(\boldsymbol{Y}^D, \gamma)$,
$\boldsymbol{V}^p = \boldsymbol{V}^p(\widetilde{\boldsymbol{\sigma}}, R)$, and
$\boldsymbol{V}^h = \boldsymbol{V}^h(\boldsymbol{Y}^h, \phi)$,

where

$\widetilde{\boldsymbol{\sigma}}$ is the stress in the effective configuration,
$\boldsymbol{Y}^D$ is thermodynamic force related to damage,
$\boldsymbol{Y}^H$ is thermodynamic force related to healing,
γ is is thermodynamic force related to damage evolution,
ϕ is is thermodynamic force related to healing evolution and,
R is thermodynamic force related to hardening due to plasticity.

The dissipation potential is a positively defined function as

$$\Theta = \boldsymbol{V}^d : \dot{\boldsymbol{\varphi}}^d + \boldsymbol{V}^p : \dot{\boldsymbol{\varphi}}^p - \boldsymbol{V}^h : \dot{\boldsymbol{\varphi}}^h \geq 0, \tag{3.18}$$

where the minus sign in front of the term $\boldsymbol{V}^h$ indicates that the healing process is a undissipative process.

It is assumed that the Helmholtz energy is separable as

$$\Psi = \Psi(\boldsymbol{\varepsilon}^e, \boldsymbol{\varphi}^d, \boldsymbol{\varphi}^p, \boldsymbol{\varphi}^h) = \Phi(\boldsymbol{\varepsilon}^e, \boldsymbol{\varepsilon}^p, \boldsymbol{D}, \boldsymbol{H}) + \Pi(\delta, p, \mu) \tag{3.19}$$

where Φ is tensorial elastic deformation function which depends both on damage and healing tensor components; Π is a scalar function which defines the evolution of inelastic variables. The elastic deformation function Φ depends on value of the internal variables and, thus can be defined as

$$\Phi(\boldsymbol{\varepsilon}^e, \boldsymbol{\varepsilon}^p, \boldsymbol{D}, \boldsymbol{H}) = \frac{1}{2}(\boldsymbol{\varepsilon} - \boldsymbol{\varepsilon}^p) : \boldsymbol{E}(\boldsymbol{D}, \boldsymbol{H}) : (\boldsymbol{\varepsilon} - \boldsymbol{\varepsilon}^p), \tag{3.20}$$

where $\boldsymbol{E}$ is the fourth-order damaged-healed stiffness tensor. Damage and healing processes are supposed to be irreversible and, thus are defined with a monotonically increasing evolution function. Moreover, damage and healing processes cannot happen simultaneously - when damage evolves, the rate of healing is equal to zero and when healing evolves, the rate of damage is equal to zero. This is referred to as the uncoupled form of damage and healing and thus, they are expressed as

$$\Pi(\delta, p, \mu) = \Pi^d(\delta) + \Pi^p(p) + \Pi^h(\mu), \tag{3.21}$$

where $\Pi^d(\delta)$, $\Pi^p(p)$ and $\Pi^h(\mu)$ are defined as

$$\Pi^d(\delta) = -\int_{\delta_0}^{\delta_1} \frac{\partial \Psi}{\partial \delta}\, d\delta = [c_1^d \delta - c_1^d c_2^d e^{\delta / c_2^d}]\Big|_{\delta_0}^{\delta_1}, \tag{3.22}$$

$$\Pi^p(p) = -\int_{p_0}^{p_1} \frac{\partial \Psi}{\partial p}\, dp = c_1^p \frac{1}{2} p2\Big|_{p_0}^{p_1}, \tag{3.23}$$

$$\Pi^h(\mu) = -\int_{\mu_0}^{\mu_1} \frac{\partial \Psi}{\partial \mu}\, d\mu = [c_1^h (c_2^h \cdot e^{\mu / c_2^h} - \mu)]\Big|_{\mu_0}^{\mu_1}. \tag{3.24}$$

Material parameters c_1^d, c_2^d, c_1^p, c_1^h and c_2^h, introduced in Eqs. 3.22-3.24, are determined experimentally. Complementary laws related to the dissipation process can be expressed by homogeneous and convex potentials in terms of the associated thermodynamic forces as

$$\Lambda(\boldsymbol{V}^d, \boldsymbol{V}^p, \boldsymbol{V}^h) = \Lambda^D(\boldsymbol{V}^d) + \Lambda^P(\boldsymbol{V}^p) + \Lambda^H(\boldsymbol{V}^h). \tag{3.25}$$

The principle of maximum dissipation defines an equilibrium thermodynamic solution, which corresponds to a constrained optimization problem. Lagrangian multiplier method can be applied on functional $\bar{\Pi}$ to solve the problem

$$\bar{\Pi} = -\Theta + \dot{\lambda}^p \Lambda^P(\boldsymbol{V}^p) + \dot{\lambda}^d \Lambda^D(\boldsymbol{V}^D) + \dot{\lambda}^h \Lambda^H(\boldsymbol{V}^H), \tag{3.26}$$

where $\dot{\lambda}^p$, $\dot{\lambda}^d$ and $\dot{\lambda}^h$ are Lagrangian multipliers related to plasticity, damage and healing, respectively. To find extreme values of $\bar{\Pi}$ the following conditions have to be satisfied

$$\begin{aligned} \frac{\partial \bar{\Pi}}{\partial \boldsymbol{V}^D} &= 0, \\ \frac{\partial \bar{\Pi}}{\partial \boldsymbol{V}^P} &= 0, \\ \frac{\partial \bar{\Pi}}{\partial \boldsymbol{V}^H} &= 0. \end{aligned} \tag{3.27}$$

These conditions correspond to the plastic strain rate, damage, and healing evolution equations. Moreover, kinematic internal variables grow along the direction normal to the corresponding potential surface

$$\begin{aligned} \dot{\varphi}^p &= \dot{\lambda}^P \frac{\partial \Lambda^P}{\partial \boldsymbol{V}^P}, \\ \dot{\varphi}^d &= \dot{\lambda}^D \frac{\partial \Lambda^D}{\partial \boldsymbol{V}^D}, \\ \dot{\varphi}^h &= \dot{\lambda}^H \frac{\partial \Lambda^H}{\partial \boldsymbol{V}^H}. \end{aligned} \tag{3.28}$$

Conditions defined in Eq. 3.28 represent plastic strain rate, damage and healing evolution functions expressed as partial derivatives of functional $\bar{\Pi}$. By assuming the corresponding form of Helmholtz free energy function, these equations can be used to model self-healing composite materials in general.

3.3. Adopted micro-damage-healing model

Damage model developed in [Darabi et al., 2011] and a healing model developed in [Abu Al-Rub et al., 2010], originally intended for asphalt materials, are opted for modelling of intrinsically self-healing polymer composite matrix material. Since both asphalt and intrinsically self-healing polymers exhibit viscous properties and time- and

temperature dependent intrinsic self-healing, these models are considered applicable to modelling of damage-healing behaviour of polymers. The damage-healing model for the polymer matrix material is validated in Chapter 4. using experimental results on Surlyn® 8940 coupons. Appropriateness of selected damage and healing models is further elaborated in that Chapter. In the following sections, derivation of adopted damage and healing constitutive models, from thermodynamic laws to evolution equations, is presented.

3.3.1. Micro-damage model

Micro-damage constitutive model proposed in [Darabi et al., 2011] comprises time- and temperature dependent damage variable evolution equation. That is why it is referred to as thermo-viscodamage model. In the formulation of the model, the concept of effective and nominal configuration is used, see Figure 3.1. Effective configuration concept is taken from the CDM and it represents the undamaged (virgin) material. Nominal configuration can be imagined as a state of a damaged cross-section of a specimen, i.e. an actual state of the material. If damaged area is removed from that cross-section, a smaller one, without damaged area, is obtained. This is what is referred to as the healing configuration. To relate the stress and strain in nominal and effective configurations, a transformation hypothesis has to be used. Here, the strain equivalence hypothesis is used. It means that the strain tensors in the effective and nominal configuration are the same, Eq. 3.29

$$\varepsilon_{ij} = \bar{\varepsilon}_{ij}. \tag{3.29}$$

According to [Darabi et al., 2012c] formulation of the micro-damage model starts with the Clausius-Duhem inequality and the expression for the Helmholtz free energy, Ψ, in the effective configuration. Moreover, [Darabi et al., 2012c] deals with the coupling of the viscodamage model to viscoelasticity and viscoplasticity. Here, for the sake of simplicity, the Helmholtz free energy is given as a function of state variables damage ϕ, and temperature T:

$$\Psi = \Psi\left(\phi, T\right). \tag{3.30}$$

It means that a purely elastic material susceptible to damage is considered here. On the other hand, Clausius-Duhem inequality is given as

$$\bar{\sigma}_{ij}\dot{\bar{\varepsilon}}_{ij} - \rho\left(\dot{\Psi} + \eta\dot{T}\right) - \frac{1}{T}\nabla_i q_i T \geq 0, \tag{3.31}$$

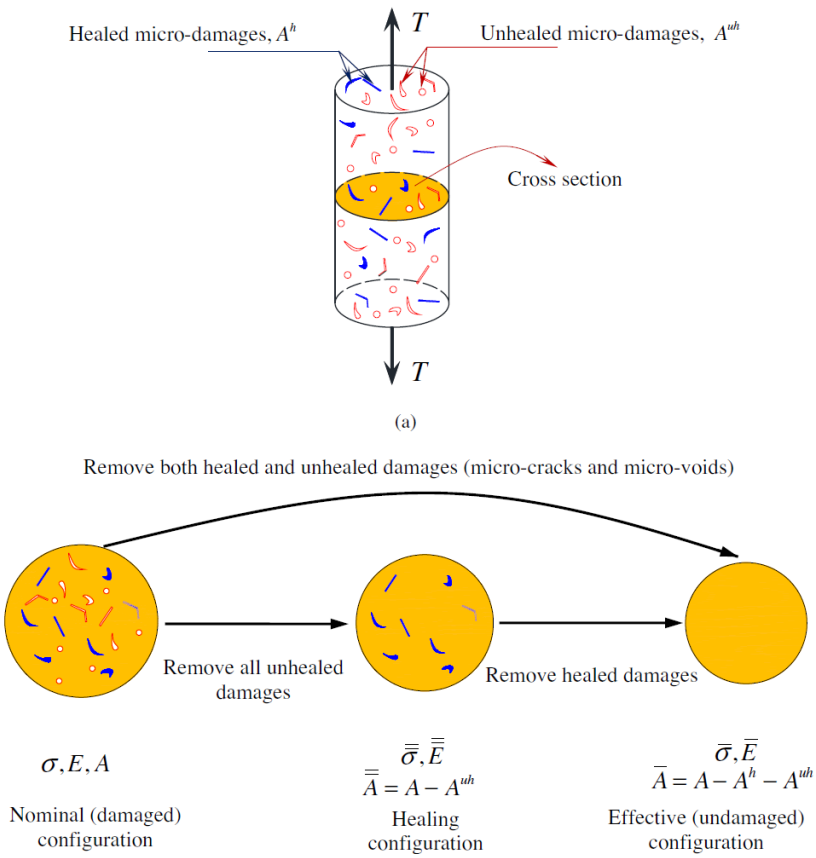

Figure 3.1: Schematic representation of nominal, healing and effective configurations on an arbitrary cross-section and relations between cross-sections, after [Darabi et al., 2012a].

where

$\bar{\sigma}_{ij}$ is the effective stress tensor,

ρ is the mass density,

η is the specific entropy,

T is the absolute temperature,

$\nabla_i q_i$ is the divergence of the heat flux vector, and

q_i is the heat flux vector.

Using the chain rule to determine the time derivative of the Helmholtz free energy with respect to its state variables gives

$$\dot{\Psi} = \frac{\partial \Psi}{\partial \phi}\dot{\phi} + \frac{\partial \Psi}{\partial\, T}\dot{T}. \tag{3.32}$$

Substituting Eq. 3.32 into Eq. 3.31 gives the following

$$-\frac{\partial \Psi}{\partial \phi}\dot{\phi} - \rho\left(\frac{\partial \Psi}{\partial\, T} + \eta\right)\dot{T} - \frac{1}{T}\nabla_i q_i T \geq 0. \tag{3.33}$$

In Eq. 3.33, the following thermodynamic conjugate forces and state laws can be distinguished

$$\bar{Y} = -\rho \frac{\partial \Psi}{\partial \phi}, \text{ and} \tag{3.34}$$

$$\eta = -\frac{\partial \Psi}{\partial\, T}, \tag{3.35}$$

where $\bar{Y}$ is the conjugate force associated with the internal state variable, ϕ, and η is the conjugate force associated with the internal state variable, T. By substituting the thermodynamic state laws, Eqs. 3.34 and 3.35 into the Eq. 3.33, the expression for the rate of the total energy dissipation, Π, is obtained

$$\Pi = \bar{Y}\dot{\phi} - \rho \left(\frac{\partial \Psi}{\partial\, T} + \eta \right) \dot{T} - \frac{1}{T} \nabla_i q_i T \geq 0. \tag{3.36}$$

From Eq. 3.36 it can be interpreted that the total rate of energy dissipation can be decomposed into viscodamage and thermal components, such as

$$\Pi = \Pi^{vd} + \Pi^{th} \geq 0, \tag{3.37}$$

where

$$\Pi^{vd} = \bar{Y}\dot{\phi} \geq 0, \tag{3.38}$$

$$\Pi^{th} = -\frac{1}{T} \nabla_i q_i T \geq 0. \tag{3.39}$$

The evolution law of the damage variable can be obtained using the calculus of several variables with Lagrange multiplier $\dot{\lambda}^{vd}$. That can be achieved by subjecting the viscoinelastic rate of energy dissipation, here $\Pi^{vi} = \Pi^{vd}$, to constraint $g = 0$

$$\Omega = \Pi^{vd} - \dot{\lambda}^{vd} g \geq 0, \tag{3.40}$$

where g is the viscodamage loading surface function and it is selected as a constraint, i.e. it is always $g = 0$. The maximum viscoinelastic dissipation principle states that the actual states of thermodynamic forces are those that maximize the inelastic dissipation function over all possible states. Using that principle, with Ω as the objective function, the following can be obtained

$$\frac{\partial \Omega}{\partial \bar{Y}} = 0. \tag{3.41}$$

By substituting Eq. 3.40 into Eq. 3.41 and using Eqs. 3.38 and 3.39, a thermodynamic law corresponding to the evolution of the damage variable, ϕ, is obtained

$$\dot{\phi} = \dot{\lambda}^{vd} \frac{\partial\, g}{\partial \bar{Y}}\,. \tag{3.42}$$

Eq. 3.42 provides the evolution function for the damage density. Lagrange multiplier $\dot{\lambda}^{vd}$ can be obtained by satisfying the consistency condition for viscodamage loading surface, i.e. $\dot{g} = 0$.

Specific form of the Helmholtz free energy function

Since healing is not considered here, the Helmholtz free energy function is a function of the damage variable, ϕ, and absolute temperature, T,

$$\Psi\left(\phi, T\right) = \Psi^{tvd}\left(\phi, T\right). \tag{3.43}$$

This means that the Helmholtz free energy function has only one component, Ψ^{tvd}, thermo-viscodamage component. In [Darabi et al., 2012c] the following form of the thermo-viscodamage component is proposed

$$\rho\Psi^{tvd} = \frac{1}{b_1}[(1-\phi)^{b_1}\langle\bar{\tau}^{vd} - \alpha\bar{I}_1\rangle \cdot e^{b_2\bar{\varepsilon}_{eff}}]\vartheta^{vd}(T), \tag{3.44}$$

where b_1, b_2 and α are material model parameters and $\vartheta^{vd}\left(T\right)$ is the viscodamage temperature coupling term such that

$$\vartheta^{vd}\left(T\right) = e^{-\gamma\left(1-\frac{T}{T_0}\right)}, \tag{3.45}$$

where γ is a material parameter and T_0 is the reference temperature. The brackets $\langle\,\rangle$ are Macaulay brackets defined by $\langle a\rangle = (a+|a|)/2$ to ensure that the non-positive values of $\bar{\tau}^{vd} - \alpha\bar{I}_1$ lead to $\rho\Psi^{tvd} = 0$. The expression $\langle\bar{\tau}^{vd} - \alpha\bar{I}_1\rangle$ in Eq. 3.44 is the component of the damage force in the effective configuration and it is assumed to have the form of the modified Drucker-Prager yielding criterion to include the pressure effects on damage. Damage starts to evolve when the condition $\bar{\tau}^{vd} - \alpha\bar{I}_1 > 0$ is satisfied, where $\bar{\tau}^{vd}$ is the deviatoric stress and has the following form

$$\bar{\tau}^{vd} = \frac{\sqrt{3\bar{J}_2}}{2}\left[1 + \frac{1}{d^{vd}} + \left(1 - \frac{1}{d^{vd}}\right)\frac{3\bar{J}_3}{\sqrt{\bar{J}_2^3}}\right], \tag{3.46}$$

where $\bar{J}_2 = \frac{1}{2}\bar{S}_{ij}\bar{S}_{ij}$ and $\bar{J}_3 = \frac{1}{2}\bar{S}_{ij}\bar{S}_{jk}\bar{S}_{ki}$ are the second and third deviatoric stress invariants of the effective stress tensor, $\bar{\boldsymbol{\sigma}}$, d^{vd} is the ratio of the damage force in the uniaxial tension to the damage force in the uniaxial compression.

Viscodamage variable evolution equation

A starting point for derivation of the viscodamage variable evolution equation is the damage force. It can be derived from the Helmholtz free energy function by substituting Eq. 3.44 into Eq. 3.34 as following

$$\bar{Y} = -\rho\frac{\partial\Psi}{\partial\phi} = -\rho\frac{\partial\Psi^{vd}}{\partial\phi} = [(1-\phi)^{b_1-1}\langle\bar{\tau}^{vd} - \alpha\bar{I}_1\rangle \cdot e^{b_2\bar{\varepsilon}_{eff}}]\vartheta^{vd}(T). \tag{3.47}$$

Here, associative flow (viscodamage) is assumed, i.e. the damage growth surface g is supposed to be the same as the damage potential function, G. A simple static damage loading surface can be defined

$$g = \bar{Y} - Y_0 \leq 0, \tag{3.48}$$

where Y_0 is the threshold damage force, which is determined experimentally. In order to include the rate-dependent damage (viscodamage), dynamic damage loading surface, χ^{vd}, can be defined, such as

$$\chi^{vd} = g - \bar{\sigma}_v^{vd} = 0, \tag{3.49}$$

where $\bar{\sigma}_v^{vd}$ is the damage overstress defined as

$$\bar{\sigma}_v^{vd} = \langle\bar{Y} - Y_0\rangle. \tag{3.50}$$

For the damage Lagrange multiplier an increasing function of the damage overstress is postulated

$$\dot{\lambda}^{vd} = \Gamma^{vd}\langle\frac{\bar{\sigma}_v^{vd} + Y_0}{Y_0}\rangle = 0, \tag{3.51}$$

where Γ^{vd} is the damage viscosity parameter and q is a material constant. Rearranging Eq. 3.51, the damage overstress can be obtained

$$\bar{\sigma}_v^{vd} = Y_0\left[\left(\frac{\dot{\lambda}^{vd}}{\Gamma^{vd}}\right)^{\frac{1}{q}} - 1\right]. \tag{3.52}$$

Substituting Eq. 3.48 into Eq. 3.42 implies that the damage multiplier $\dot{\lambda}^{vd}$ is the same as the damage rate, i.e. $\dot{\lambda}^{vd} = \dot{\phi}$. Substituting Eqs. 3.47 and 3.48 into Eq. 3.49 yields the dynamic viscodamage loading surface

$$\chi^{vd} = \bar{Y} - Y_0\left(\frac{\dot{\phi}}{\Gamma^{vd}}\right)^{\frac{1}{q}} = 0, \tag{3.53}$$

and substituting Eq. 3.47 into Eq. 3.53 yields its final form

$$\chi^{vd} = \left[(1-\phi)^{b_1-1} \left\langle \bar{\tau}^{vd} - \alpha \bar{I}_1 \right\rangle \cdot e^{b_2 \bar{\varepsilon}_{eff}}\right] \vartheta^{vd} - Y_0 \left(\frac{\dot{\phi}}{\Gamma^{vd}}\right)^{\frac{1}{q}} = 0. \tag{3.54}$$

The generalized Kuhn-Tucker conditions for loading/unloading can be applied to the dynamic viscodamage surface to define the damage nucleation criterion

$$\chi^{vd} \leq 0, \quad \dot{\lambda}^{vd} \geq 0, \quad \dot{\lambda}^{vd}\chi^{vd} = 0, \quad \dot{\lambda}^{vd}\dot{\chi}^{vd} = 0. \tag{3.55}$$

The thermo-viscodamage model can be obtained by rearranging Eq. 3.52

$$\dot{\phi} = \Gamma^{vd} \left[\frac{(1-\phi)^{b_1-1} \left\langle \bar{\tau}^{vd} - \alpha \bar{I}_1 \right\rangle}{Y_0}\right]^q \cdot e^{b_2 q \bar{\varepsilon}_{eff}} \cdot (\vartheta^{vd})^q, \tag{3.56}$$

where

$$\vartheta^{vd}(T) = e^{-\gamma\left(1-\frac{T}{T_0}\right)}. \tag{3.57}$$

In the constitutive model of a self-healing composite matrix material presented in this Thesis, the following form of the damage variable evolution equation is used

$$\dot{\phi} = \Gamma^{vd} \left[\frac{\bar{Y}}{Y_0}\right]^q (1-\phi)^2 \cdot e^{k \cdot \bar{\varepsilon}_{eff}} \cdot \left(\vartheta^{vd}\right)^q, \tag{3.58}$$

where

$\bar{Y}$ is the damage driving force and is calculated as $\bar{Y} = \sqrt{3\bar{J}_2}$,
Γ_{vd} is the damage viscosity parameter,
Y_0 is the threshold damage force,
q and k are material parameters which have to be determined experimentally,
$\bar{\varepsilon}_{eff}$ is the effective (equivalent) strain in the effective configuration, and
$\left(\vartheta^{vd}\right)^q$ is dependency of damage on temperature defined in Eq. 3.57.

3.3.2. Healing model

The thermodynamic framework for theoretical derivation of the healing variable evolution law is taken from [Darabi et al., 2012a]. The concept of nominal and effective configurations, presented in previous section, is extended with the healing configuration. The healing configuration is firstly introduced in [Abu Al-Rub et al., 2010] and it can be imagined as a state of the material where damaged area is removed from the cross-section and only virgin and healed material is left, Figure 3.1.

For derivation of healing variable evolution equation, the power equivalence hypothesis is used for relating the healing and nominal configurations. However, the formulation is started with the principle of virtual power according to which the external expenditure of the power due to a virtual motion should be balanced by the internal expenditure of power due to the same virtual motion and it is denoted as

$$P_{int} = P_{ext}, \tag{3.59}$$

The internal expenditure of the power is given as

$$P_{int} = \int_V (\boldsymbol{\sigma} : \dot{\boldsymbol{\varepsilon}}^e + Y\dot{\phi} - H\dot{h} + \xi\dot{T} + \gamma\nabla\dot{T})\, dV, \tag{3.60}$$

where $\boldsymbol{\sigma}$ is the Cauchy stress tensor, $\dot{\boldsymbol{\varepsilon}}^e$ is the rate of the elastic strain tensor. The damage force, Y, and the healing force, H, are the generalized thermodynamic forces conjugate to the damage density and the healing variable, respectively. Two additional thermodynamic forces, ξ and γ, conjugate to temperature and its gradient, respectively, are defined. Equation 3.60 implies that the damage process increases the internal expenditure of the power, whereas, the micro-damage healing process decreases the internal expenditure of the power. On the other hand, the external expenditure of the power is given as

$$P_{ext} = \int_V b_i\dot{u}_i dV + \int_S t_i\dot{u}_i dS + \int_V \rho\ddot{u}_i\dot{u}_i dV + \int_S \chi\dot{T} dS, \tag{3.61}$$

where $\boldsymbol{u}$ is the displacement vector, $\boldsymbol{b}$ is the macroscopic body force, $\boldsymbol{t}$ is the macroscopic surface traction, ρ is the mass density and χ is the generalized temperature traction, conjugate to the temperature. Using Eq. 3.59 and after some mathematical manipulations the following relations are obtained

$$\sigma_{ij,j} + b_i = \rho\ddot{u}_i \text{ in } V, \tag{3.62}$$

$$t_i = \sigma_{ij}n_j \text{ on } S, \tag{3.63}$$

$$\chi = \gamma_i n_i \text{ on } S, \tag{3.64}$$

$$Y = 0 \text{ in } V, \tag{3.65}$$

$$-H\dot{h} + (\xi - \gamma_{i,i})\,\dot{T} = 0 \text{ in } V, \tag{3.66}$$

where $\boldsymbol{n}$ is the outward unit normal on the boundary S. Eq. 3.62 is the local static/dynamic macroforce balance whereas the Eq. 3.63 represents the boundary traction as density

of the surface forces. Eq. 3.64 defines the boundary traction for the thermodynamic forces conjugate to $\dot{T}$. Eq. 3.65 defines the damage microforce balance which can be used to derive the damage evolution equation. Since the damage evolution equation is derived in the previous section, it will not be discussed here. Eq. 3.66 is referred to as the micro-damage healing microforce balance and is used to derive the healing evolution equation. If the gradient of the rate of the temperature is neglected, i.e. when $\nabla\dot{T} \sim 0$, the equation has the following form

$$-H\dot{h} + \xi\dot{T} = 0. \tag{3.67}$$

Eq. 3.67 shows that the healing process is dependant on the rate of the temperature, i.e. external heat is required for the healing process to occur. The relationship between the rate of the temperature change and the healing rate is assumed linear, i.e. $\xi\dot{T} = K\dot{h}$. Thus, the microdamage healing microforce balance is simplified to the following form, with $K = \frac{\xi\dot{T}}{\dot{h}}$

$$H - K = 0. \tag{3.68}$$

Since the unhealed damage does not contribute to the internal expenditure of power in the healing configuration, the internal expenditure of power can be written in the healing configuration as

$$\bar{\bar{P}}_{int} = \int_V \bar{\bar{\boldsymbol{\sigma}}} : \dot{\bar{\bar{\boldsymbol{\varepsilon}}}}^e \, dV. \tag{3.69}$$

Using the power equivalence hypothesis and Eqs. 3.67 and 3.65 it can be shown that Eqs. 3.60 and 3.67 are the same

$$\bar{\bar{P}}_{int} = P_{int}. \tag{3.70}$$

Here, the Helmholtz free energy is assumed as a function of the damage variable, ϕ, and the healing variable, h, as

$$\Psi = \Psi\left(\phi, h\right). \tag{3.71}$$

Therefore, the Clausius-Duhem inequality can be written as

$$\int_V \rho\dot{\Psi} \leq \; P_{int}. \tag{3.72}$$

Taking the time derivative of Eq. 3.71 and substituting it into Eq. 3.72 yields the following equation

$$\left(Y - \rho\frac{\partial\Psi}{\partial\phi}\right)\dot{\phi} - \left(H + \rho\frac{\partial\Psi}{\partial\, h}\right)\dot{h} + K\dot{h} \geq 0. \tag{3.73}$$

From Eq. 3.72, the rate of the energy dissipation can be written as

$$\Pi = \left(Y - \rho\frac{\partial\Psi}{\partial\phi}\right)\dot{\phi} - \left(H + \rho\frac{\partial\Psi}{\partial\ h}\right)\dot{h} + K\dot{h} \geq 0. \tag{3.74}$$

where the rate of the energy dissipation during the damage process can be designated as

$$\Pi^{vd} = \left(Y - \rho\frac{\partial\Psi}{\partial\phi}\right)\dot{\phi}, \tag{3.75}$$

whereas the energy dissipation during the healing process can be written as

$$\Pi^{h} = -\left(H + \rho\frac{\partial\Psi}{\partial\ h}\right)\dot{h} + K\dot{h}. \tag{3.76}$$

Therefore, the total rate of the energy dissipation can be formulated as

$$\Pi = \Pi^{vd} + \Pi^{h} \geq 0. \tag{3.77}$$

Damage and healing processes do not occur at the same time. That is why the rate of the energy dissipation during the damage process is caused by the damage nucleation and growth only

$$\Pi = \Pi^{vd} = \left(Y - \rho\frac{\partial\Psi}{\partial\phi}\right)\dot{\phi} \geq 0,$$
$$\dot{h} = 0. \tag{3.78}$$

Similar is during the healing process. In that case, Π represents the rate of the energy dissipation due to the micro-damage healing process

$$\Pi = \Pi^{h} = -\left(H + \rho\frac{\partial\Psi}{\partial\ h}\right)\dot{h} + K\dot{h} \geq 0,$$
$$\dot{\phi} = 0. \tag{3.79}$$

Eq. 3.79 shows that the micro-damage healing process causes the stored energy to decrease. Eqs. 3.78 and 3.79 are only a function of the Helmholtz free energy which means that the energy terms can be defined as

$$Y^{ene} \equiv \rho\frac{\partial\Psi}{\partial\phi},$$
$$H^{ene} \equiv -\rho\frac{\partial\Psi}{\partial\ h}, \tag{3.80}$$

where Y^{ene} is the energy component of the thermodynamic force conjugate to the damage variable and H^{ene} is the energy component of the thermodynamic force conjugate to the healing variable. Substituting Eq. 3.80 into Eqs. 3.78 and 3.79 gives

$$\Pi = (Y - Y^{ene})\,\dot{\phi} - (H - H^{ene})\,\dot{h} + K\dot{h} \geq 0,$$

$$\Pi = Y^{dis}\dot{\phi} - \left(H^{dis} - K\right)\dot{h} \geq 0, \tag{3.81}$$

where $Y^{dis} = Y - Y^{ene}$ is the dissipative component of the thermodynamic force conjugate to the damage variable, whereas $H^{dis} = H - H^{ene}$ is the dissipative component of the thermodynamic force conjugate to the healing variable. The dissipative components can be identified using the maximum rate of energy dissipation principle

$$Y^{dis} = \lambda^{vd}\frac{\partial \Pi}{\partial \dot{\phi}}, \tag{3.82}$$

$$H^{dis} - K = -\lambda^{h}\frac{\partial \Pi}{\partial \dot{h}}, \tag{3.83}$$

where λ^{vd} and λ^{h} are viscodamage and micro-damage healing Lagrange multipliers, respectively, which can be determined using the calculus of multiple variables

$$\lambda^{vd} = \frac{\Pi}{\left(\frac{\partial \Pi}{\partial \dot{\phi}}\dot{\phi}\right)}, \tag{3.84}$$

$$\lambda^{h} = \frac{\Pi}{\left(\frac{\partial \Pi}{\partial \dot{h}}\dot{h}\right)}. \tag{3.85}$$

Specific form of the Helmholtz free energy function

The next step is to assume mathematical function for the Helmholtz free energy and the rate of the energy dissipation function. Here, the following expression is supposed for the Helmholtz free energy function

$$\rho\Psi = \frac{1}{2}\bar{\bar{\boldsymbol{\varepsilon}}}^{e} : \bar{\bar{\boldsymbol{E}}} : \bar{\bar{\boldsymbol{\varepsilon}}}^{e} + \Gamma_1(1-\phi)(1-h), \tag{3.86}$$

and the following equation for the rate of the energy dissipation

$$\Pi = \Gamma_2\,(1-\phi)^{c_1}\,(1-h)\left(\frac{\bar{\bar{Y}}}{Y_{th}}\right)^{c_2} e^{c_3\bar{\bar{\varepsilon}}_{eff}}\dot{\phi}^2 + \Gamma_3\,(1-\phi)^{c_4}\,(1-h)^{c_5}\,\dot{h}^2. \tag{3.87}$$

The damage and micro-damage healing microforce balances, given with Eq. 3.65 and Eq. 3.68 can be rewritten as

$$\begin{aligned} Y &= 0, \\ Y^{ene} + Y^{dis} &= 0, \\ Y^{ene} &= -Y^{dis}, \end{aligned} \tag{3.88}$$

and

$$\begin{aligned} H - K &= 0, \\ H^{ene} + H^{dis} - K &= 0, \\ H^{ene} &= -(H^{dis} - K). \end{aligned} \tag{3.89}$$

Energy and dissipative components of the thermodynamic conjugate forces can be identified by substituting Eq. 3.87 into Eqs. 3.80, 3.82 and 3.83

$$Y^{ene} = -\Gamma_1 \left(1 - h\right), \tag{3.90}$$

$$Y^{dis} = \Gamma_2 \left(1 - \phi\right)^{c_1} \left(1 - h\right) \left(\frac{\bar{\bar{Y}}}{Y_{th}}\right)^{c_2} e^{c_3 \bar{\bar{\varepsilon}}_{eff}} \dot{\phi}, \tag{3.91}$$

$$H^{ene} = \Gamma_1 \left(1 - \phi\right), \tag{3.92}$$

$$H^{dis} - K = -\Gamma_3 \left(1 - \phi\right)^{c_4} \left(1 - h\right)^{c_5} \dot{h}. \tag{3.93}$$

The viscodamage evolution equation, given with Eq. 3.58, can be obtained using this set of equations. The difference is that here the dependence on temperature was not introduced in the assumption of the Helmholtz free energy function. Furthermore, here, the power equivalence hypothesis was used, and its application yielded the same equation. The differences arise when the model is numerically implemented.

Healing variable evolution equation

The healing variable evolution equation can be determined by substituting Eqs. 3.92 and 3.93 into Eq. 3.94

$$\dot{h} = \Gamma^h \left(1 - \phi\right)^{m_1} \left(1 - h\right)^{m_2}, \tag{3.94}$$

where $\Gamma^h = \frac{\Gamma_1}{\Gamma_3}$, $m_1 = 1 - c_4$ and $m_2 = -c_5$. Parameters Γ^h, m_1 and m_2 have to be determined experimentally.

Equations 3.58 and 3.94 represent the micro-damage and healing variable evolution equations, respectively. These equations are implemented into the elastic-plastic-damage-healing constitutive model for intrinsically self-healing polymers, utilised as matrix constituents in self-healing FRP composites. In Chapter 4. the aforementioned constitutive model is validated using experimental results on Surlyn® 8940 coupons, conducted at the Faculty of Mechanical Engineering and Naval Architecture.

4 Modelling of a self-healing polymer

A constitutive model for an intrinsically self-healing polymer matrix material is developed and implemented into the Abaqus/Standard user material subroutine UMAT. It comprises plasticity, micro-damage and healing models, which are described in detail in Chapter 3. The model is validated using static tensile tests and loading/unloading cases. Afterwards it is used in development of a constitutive model for the intrinsically self-healing UD FRP composite material.

4.1. Micro-damage-healing plasticity model

The constitutive model of a self-healing polymer matrix material, developed for applications in micromechanical modelling of FRP composites, comprises damage model from [Darabi et al., 2011] and healing model from [Abu Al-Rub et al., 2010] originally developed for asphalt. These models are considered applicable to the material investigated in this research, which is a partially neutralised poly(ethylene-co-methacrylic acid) (EMAA) ionomer copolymer, Surlyn® 8940 by DuPont. Applicability of the model is justified by the fact that Surlyn® 8940 and asphalt exhibit phenomenologically similar material properties, such as viscous properties, and time- and temperature dependant intrinsic healing. The experimental validation of applied constitutive models within this Thesis approved this assumption. Viscous properties, i.e. rate-dependent behaviour of Surlyn® 8940 has been reported in [Varley and van der Zwaag, 2008]. Time- and temperature dependency of the healing phenomenon was proven in [Kalista and Ward, 2007, Varley and van der Zwaag, 2008] and [Reynolds, 2011]. Furthermore, the elastic response, which enables closure of microcracks, is crucial for the healing process. The

healing process initiates as soon as microcrack surfaces get in contact [Reynolds, 2011]. In [Reynolds, 2011] it is even shown that certain degree of healing can be achieved at room temperatures. Moreover, according to research in [Varley and van der Zwaag, 2008] and [Haramina et al., 2021], thermal history greatly influences mechanical properties of Surlyn® 8940. Plasticity model employed is the von Mises linear isotropic hardening plasticity. A brief mathematical description is given in the following paragraphs.

4.1.1. Micro-damage-healing model

Micro damage-healing model proposed here incorporates mathematical functions, describing evolution of the damage variable from [Darabi et al., 2011] and evolution of the healing variable based on the model in [Abu Al-Rub et al., 2010]. The concept of nominal and effective configurations, which are commonly used in CDM for development of a new constitutive model, is extended by introducing the healing configuration. The healing configuration is a feature introduced in [Abu Al-Rub et al., 2010] for the first time. Additionally, the concept of nominal, healing and effective configurations streamlines the numerical implementation of the model.

The nominal configuration represents the true state of the material, both with healed, A_h, and unhealed micro-damage, A_{uh}. On the other hand, the healing configuration can be imagined as a state of the material in which only healed damage exists. Consequently, the unhealed damage is removed, and the total cross-section area is smaller than the one in nominal configuration. Damage, healing and plasticity models are coupled in the healing configuration. Finally, the concept of effective configuration is taken from the theory of CDM and it represents a virgin, i.e. undamaged material. All three configurations are schematically represented in Figure 4.1. Three cross-section areas are designated: A, representing cross-section area in the nominal configuration, $\bar{\bar{A}}$, the cross-section area in the healing configuration and $\bar{A}$, being the cross-section area in effective configuration. Stress and strain tensors in nominal and healing configurations are related by means of strain equivalence hypothesis, which is a well-known transformation hypothesis in CDM. The strain equivalence hypothesis streamlines the numerical implementation of the proposed constitutive model, since the strain increment and total strain in nominal and healing configurations are considered equal.

Damage and healing variables are physically represented as cross-section area ratios. Damage variable, ϕ, ranges from 0 to 1, where $\phi = 0$ represents undamaged material and

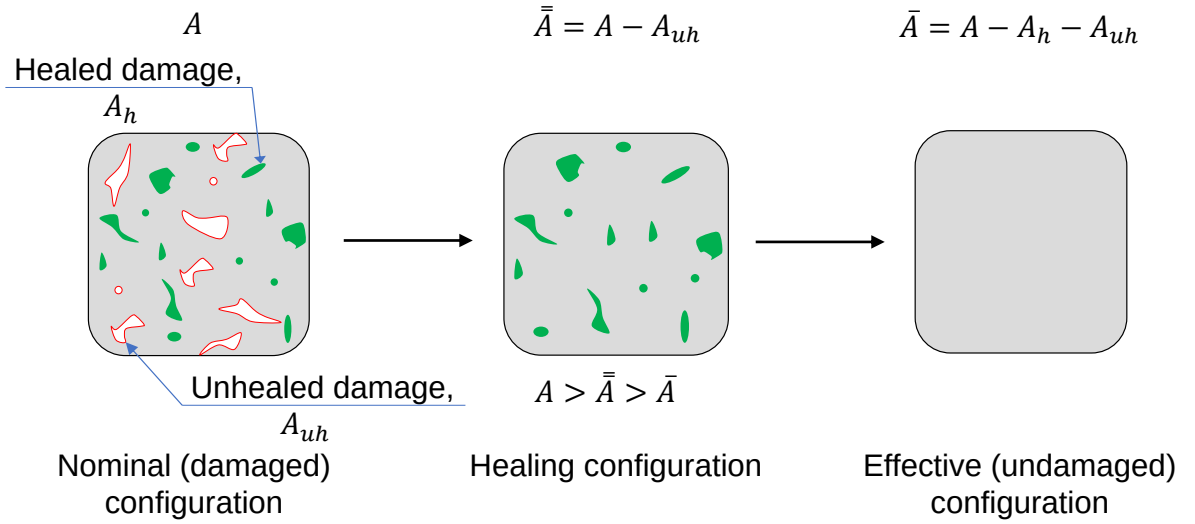

Figure 4.1: Schematic representation of nominal, healing and effective configurations on an arbitrary cross-section and relations between cross-sections, after [Darabi et al., 2012a].

$\phi = 1$ represents complete damage (fracture). Healing variable, h, as well as the damage variable, ranges from 0 to 1, where $h = 0$ means that no damage is healed and $h = 1$ means that all induced micro-damage is mended. Damage variable, ϕ, is defined as a ratio of A_d to total area A, where A_d is a summation of both healed, A_h, and unhealed damage, A_{uh}, i.e.: $A_d = A_{uh} + A_h$. On the other hand, the healing variable, h, is a ratio of healed damage, A_h, to A_d, i.e.

$$\phi = \frac{A_d}{A} = \frac{A_{uh} + A_h}{A}, \tag{4.1}$$

$$h = \frac{A_h}{A_d} = \frac{A_h}{A_{uh} + A_h}. \tag{4.2}$$

Both damage and healing variables are scalars and defined with ordinary differential equations, Eq. (4.3) and Eq. (4.4), which are functions of one independent variable, time. Damage evolution equation, after [Darabi et al., 2011], is given in its rate form as

$$\dot{\phi} = \Gamma^{vd} \left(\frac{\bar{\bar{Y}}}{Y_{th}} \right)^q (1 - \phi)^2 \cdot \exp\left(k \cdot \bar{\bar{\varepsilon}}_{eff}\right), \tag{4.3}$$

where

Γ_{vd} is the damage viscosity parameter which determines how fast the damage

variable evolves;
$\bar{\bar{Y}} = \sqrt{(3/2)\bar{\bar{\boldsymbol{\sigma}}}'_{ij}\bar{\bar{\boldsymbol{\sigma}}}'_{ij}}$ is the damage driving force in the healing configuration, where $\bar{\bar{\boldsymbol{\sigma}}}'_{ij}$ is the healing deviatoric stress tensor;
Y_{th} is the threshold damage force;
q and k are material parameters and
$\bar{\bar{\varepsilon}}_{eff} = \bar{\bar{\boldsymbol{\varepsilon}}}_{ij} \cdot \bar{\bar{\boldsymbol{\varepsilon}}}_{ij}$ is the effective (equivalent) strain in the healing configuration.

Mathematical formulation of Eq. (4.3) results in several features: (i) it can simulate the non-linear response of the material both during loading and unloading, (ii) it is rate-dependent, (iii) it accounts for the deformation history by including the level of equivalent strain. Rate dependency of the damage variable is significant, since this constitutive model is to be used for impact analyses in the later phases of the research. Furthermore, healing evolution equation is given in its rate form as

$$\dot{h} = \Gamma^h (1-h)^{m_1} (1-\phi)^{m_2}, \tag{4.4}$$

where Γ^h is the healing viscosity parameter which determines how fast the healing variable evolves and m_1 and m_2 are material parameters which are determined experimentally. Eq. (4.4) defines behaviour of the healing variable so that it asymptotically tends to 1. In theory, provided that the healing period lasts infinitely long, damaged material could be fully healed which means that the elasticity modulus would be fully recovered. In actual applications complete recovery of mechanical properties can never be achieved so this represents only a theoretical consideration. Additionally, the effective damage variable is introduced to capture the interaction between damage and healing variables. It ranges from 0 to 1, $0 < \phi_{eff} < 1$ where $\phi_{eff} = 0$ means that the material is undamaged, or all induced micro-damage is healed and $\phi_{eff} = 1$ indicates fracture. It is defined as

$$\phi_{eff} = \phi(1-h). \tag{4.5}$$

4.1.2. Von Mises linear isotropic hardening plasticity model

Plasticity model employed here is the von Mises linear isotropic hardening plasticity. The constitutive model developed in this work is intended to be used in the micromechanical modelling of fibre reinforced composites, where the use of von Mises linear isotropic

hardening plasticity model is a common practice [Doghri et al., 2011, Batra et al., 2012]. In [Voyiadjis et al., 2011] a thermodynamically consistent framework for modelling of von Mises isotropic hardening plasticity in polymers is developed. The physical justification of the isotropic hardening lies in the fact that the plastic deformation in polymers is based on the change in entropy of the bound in polymers. Moreover, according to [Deschanel et al., 2009], Surlyn has 40 % effective crystallinity content and the glass transition temperature in the range of -20 to 70 °C. Thus, at room temperatures and higher, crystal slip in the crystalline regions is the dominant yielding mechanism. Hence, the von Mises linear isotropic hardening plasticity model is considered appropriate for describing yielding mechanism of the investigated material.

The von Mises linear isotropic hardening plasticity model is defined with

σ_{y0}, the initial yield stress,

r, isotropic hardening variable,

H, linear isotropic hardening parameter (material constant), and

p, the effective plastic strain.

Thereby, the yield stress, σ_y, increases linearly with each subsequent loading above the current yield stress as

$$\sigma_y = \sigma_{y0} + r(p), \tag{4.6}$$

$$r(p) = \int H\, dp\ , \tag{4.7}$$

where dp is the effective plastic strain increment. Von Mises equivalent stress is calculated as

$$\sigma_e = \sqrt{\frac{3}{2}\boldsymbol{\sigma}'_{ij}\boldsymbol{\sigma}'_{ij}}, \tag{4.8}$$

where $\boldsymbol{\sigma}'_{ij}$ is the deviatoric stress tensor. Finally, the form of the yield surface is given as

$$f = \sigma_e - (\sigma_{y0} + \int H\, dp\ ), \tag{4.9}$$

where σ_{y0} is the yield stress. If $f > 0$, the material has entered the plasticity region.

4.2. Numerical implementation

The proposed constitutive model is numerically implemented into Abaqus/Standard user material subroutine UMAT using the incremental approach. The subroutine is

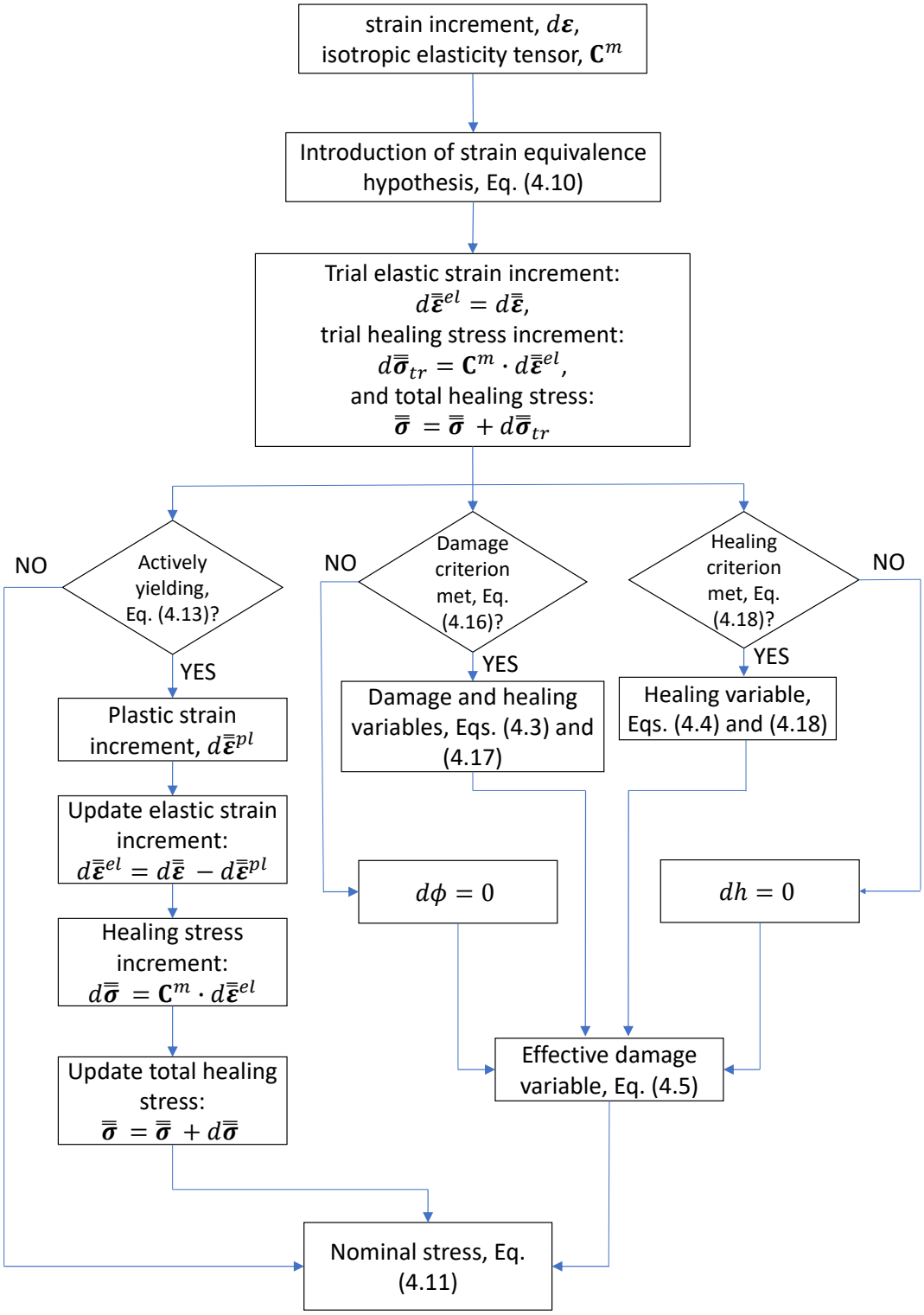

Figure 4.2: A UMAT flowchart showing the numerical implementation procedure of the developed constitutive model.

written in FORTRAN77 and the numerical implementation flowchart is given in Figure 4.2.

As depicted in Figure 4.2, firstly, the strain increment vector, provided by the Abaqus finite element solver is introduced. Then, the material's isotropic elasticity tensor is defined based on the mechanical properties of the material: elasiticy modulus, E, and Poisson coefficient ν. In addition, damage-healing model and plasticity model parameters are defined. Subsequently, the strain equivalence hypothesis is introduced, Eq. 4.10, which states that strains are equal in nominal and healing configurations. Thus, in the following text *in the healing configuration* concerning the strains will be omitted. Then, a trial elastic strain is defined and using it, trial healing stress increment and total healing stress are calculated. Now, the program checks whether the healing, damaging or plasticity initiation criteria are satisfied. If the plasticity initiation criterion is met, the plastic strain increment, $d\bar{\boldsymbol{\varepsilon}}^{pl}$, using the return-mapping algorithm is calculated. Using the calculated plastic strain increment, with application of the additive decomposition of strain, the elastic strain increment is determined. With the elastic strain increment known, the healing stress increment and thus, total healing stress can be calculated. When the damage initiation criterion is satisfied, the damage variable is calculated using the Eq. 4.3. Moreover, if the material has been previously healed, i.e. the healing variable is $h > 0$, the healing variable is reduced during the damaging process, since the healed material can be damaged again. The reduction of the healing variable during the damaging process is governed by Eq. 4.17. On the other hand, if the healing initiation criterion is met, the healing variable evolves according to the Eq. 4.18. Whether the damage and healing criteria are met or not, the effective damage variable, ϕ_{eff} is calculated using the Eq. 4.5. Using the effective damage variable, nominal stress is calculated. If damage and healing variables are $\phi = h = 0$, the effective damage variable is $\phi_{eff} = 0$ and Eq. 4.11 becomes trivial, $\boldsymbol{\sigma} = \bar{\bar{\boldsymbol{\sigma}}}$. The nominal stress represents the required output of the UMAT/VUMAT subroutine.

As already mentioned, damage, healing and plasticity models are coupled in the healing configuration, and the introduction of the strain equivalence hypothesis streamlines the numerical implementation. According to the strain equivalence hypothesis, strain increment, $d\boldsymbol{\varepsilon}$, is equal both in the nominal and the healing configuration. Thus, one can write the following equation

$$d\bar{\bar{\boldsymbol{\varepsilon}}} = d\boldsymbol{\varepsilon}, \tag{4.10}$$

where $d\bar{\bar{\boldsymbol{\varepsilon}}}$ is the healing strain increment. The introduction of the strain equivalence hypothesis is followed by the numerical implementation of damage, healing and plasticity models. That means that all the calculus is performed in the healing configuration and that all variables of the plasticity, damage and healing models are used as healing variables. Firstly, the plasticity model is implemented, and then it is followed by the implementation of damage and healing models. In the end, nominal stress is calculated as

$$\boldsymbol{\sigma} = (1 - \phi_{eff}) \cdot \bar{\bar{\boldsymbol{\sigma}}}, \tag{4.11}$$

where $\bar{\bar{\boldsymbol{\sigma}}}$ is the healing stress tensor.

4.2.1. Von Mises linear isotropic hardening plasticity model

The initial yielding stress, σ_{y0}, is a material property, and it is given in the nominal configuration. Since the calculus is carried out in the healing configuration, the yielding stress has to be transformed into the healing configuration, i.e. the initial healing yielding stress, $\bar{\bar{\sigma}}_{y0}$, has to be determined. It is done using the following relation

$$\bar{\bar{\sigma}}_{y0} = \sigma_{y0} \cdot (1 - \phi_{eff}). \tag{4.12}$$

Now, the yielding surface has the form

$$\bar{\bar{f}} = \bar{\bar{\sigma}}_e - (\bar{\bar{\sigma}}_{y0} + \int H \cdot \, dp \,), \tag{4.13}$$

where the equivalent stress is calculated using the healing deviatoric stress, $\bar{\bar{\sigma}}'_{ij}$. The principle of additive decomposition of strain is used to divide total strain into elastic and plastic strain, i.e.

$$d\bar{\bar{\boldsymbol{\varepsilon}}} = d\bar{\bar{\boldsymbol{\varepsilon}}}^{el} + d\bar{\bar{\boldsymbol{\varepsilon}}}^{pl} \tag{4.14}$$

An implicit integration scheme – a return-mapping algorithm, is employed to solve the model equations, i.e. to determine the healing plastic strain increment $d\boldsymbol{\varepsilon}^{pl}$.

4.2.2. Damage model

The behaviour of the damage model is governed by the healing damage driving force, $\bar{\bar{Y}}$, and the threshold damage force, Y_{th}, which is a material parameter determined experimentally. The healing damage driving force, essentially, has the form of the von

Mises equivalent stress in the healing configuration, and is calculated using the healing deviatoric stress tensor as

$$\bar{\bar{Y}} = \sqrt{\frac{3}{2}\bar{\bar{\boldsymbol{\sigma}}}'_{ij}\bar{\bar{\boldsymbol{\sigma}}}'_{ij}}. \tag{4.15}$$

When the healing damage driving force becomes greater than the threshold damage force, i.e.: when $\bar{\bar{Y}} \geq Y_{th}$, damage evolution initiates. Thus, the damage initiation criterion can be simply stated as

$$\sqrt{\frac{3}{2}\bar{\bar{\boldsymbol{\sigma}}}'_{ij}\bar{\bar{\boldsymbol{\sigma}}}'_{ij}} - Y_{th} \geq 0. \tag{4.16}$$

The method used to solve the damage variable evolution equation, Eq. (4.3), is the fourth order explicit Runge-Kutta method.

4.2.3. Healing model

Healing process is defined to initiate when the material is not being loaded, i.e. when the strain rate is equal to 0 and when damage exists, since the undamaged material cannot be healed. Fourth order explicit Runge-Kutta method is employed again to solve the differential equation defining evolution of healing variable, Eq. (4.4). Physical definition of the healing variable is expressed with cross-section surfaces, $h = A_h/A_d$, where A_d consists both of healed, A_h, and unhealed damage, A_{uh}. Since A_{uh} increases during the damaging process, the healing variable can decrease as well, according to [Darabi et al., 2012a]. The decrease is a result of further damaging of the virgin material and repeated damaging of previously healed portions of the material. Thus, the healing variable evolution condition can be stated as

$$h^{t+\Delta t} = \frac{\phi^t}{\phi^{t+\Delta t}} \cdot h^t \text{ when } \dot{\phi}^{t+\Delta t} \geq 0, \text{ and } h > 0, \tag{4.17}$$

$$h^{t+\Delta t} = h^t + \dot{h}^{t+\Delta t} \cdot \Delta t \text{ when } \phi^{t+\Delta t} \geq 0 \text{ and } \dot{\varepsilon} = 0, \tag{4.18}$$

where the equation for the healing variable evolution given with Eq. (4.18) is solved using the fourth order explicit Runge-Kutta method, and $\dot{h}$ is given in Eq. (4.4).

4.3. Validation - static tensile and cyclic tensile loading

The proposed constitutive model is validated using two sets of experiments, both of which had been conducted at the Faculty of Mechanical Engineering and Naval Architecture, University of Zagreb. The first set of experiments included static tensile tests on Surlyn® 8940 specimens, whereas the second included two-cycle tests on Surlyn® 8940 coupons. Validation results have been previously published in [Smojver et al., 2022c]. All tests were performed specifically for validation purposes, following the guidelines from ISO 527-2. Experimental results of static tensile tests have been previously published in [Haramina et al., 2021]. These tests were performed at the loading speed of 50 mm/min. On the other hand, two-cycle tensile tests were performed at the loading speed of 20 mm/min, and displacements were measured using a double gauge. Double gauge enables measurements of displacements on both sides of the specimen and finally, the averaged value is calculated. The experimental setup is depicted with a sketch in Figure 4.3. Experiments were conducted at room temperatures, since healing is achieved even at such temperatures, as reported in [Reynolds, 2011]. Specimens were left to heal for 5 seconds between the two cycles.

Table 4.1: Parameters of experimental procedures for validation of the constitutive model for intrinsically self-healing polymer matrix material.

	STATIC TENSILE TEST	TWO-CYCLE TENSILE TEST
subject of validation	damage model	damage, healing and plasticity models
applied standard	ISO 527-2	ISO 527-2
loading rate	50 mm/min	20 mm/min
coupon material	Surlyn® 8940	Surlyn® 8940
healing time	-	5 s
temperature	21 °C	21 °C
displacement measurement	loading spindle displacement	double gauge

Described experiments represent the set of experimental procedures for validation of the developed constitutive model for intrinsically self-healing polymer matrix material. Static tensile tests are utilised to prove the validity of the damage model, whereas the

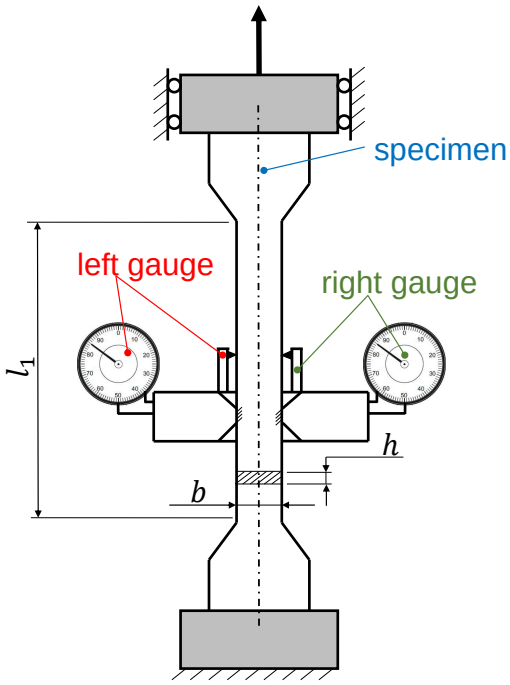

Figure 4.3: Schematic representation of experimental setup for two-cycle tensile tests with designated specimen, double displacement-measuring gauge, and specimen dimensions: l_1, total length of narrow parallel-sided portion; b, width; h, thickness.

two-cycle tensile tests are used to validate the healing and plasticity models. Experiments' parameters are summarised in Table 4.1.

In Abaqus/Standard, for simulation of the aforementioned experiments, a simple rectangular specimen is used. In agreement with ISO 527-2, the specimen has a total length of l_1, which is the length of the narrow parallel-sided portion of the specimen, and the gauge length, L_0, which is a segment of the specimen upon which measurements are performed. Specimen dimensions are given in Figure 4.4.

In order to accurately simulate the experiment conditions, the force is measured in the reference point, point C in Figure 4.4, which is rigidly connected to the specimen on one end. At the other end, boundary conditions restricting displacements in all directions are defined. Displacement, i.e. elongation of the gauge length, ΔL, is calculated from displacement measurements as follows: $\Delta L = u_B - u_A$, where u_B is the displacement of point B and u_A is the displacement of point A, see Figure 4.4. Afterwards, stress and strain are calculated directly from the force and displacement measurements. Stress is simply calculated as a ratio of the applied force over the cross-section area ($b \times h$), while

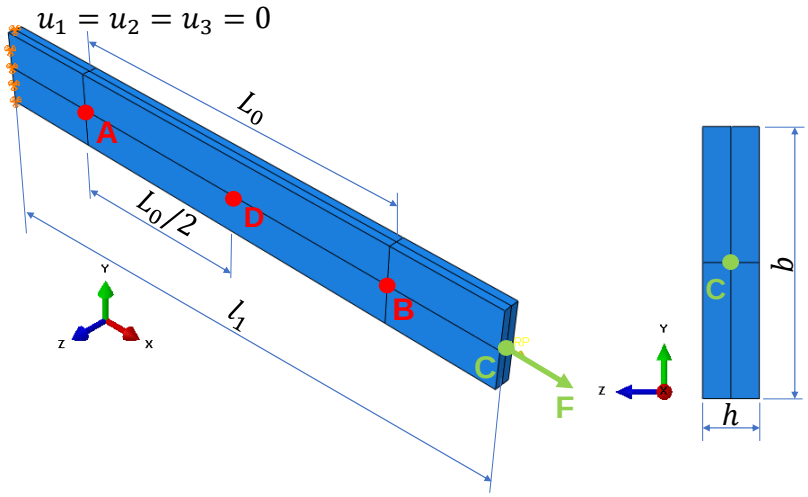

	Static tensile test	Two-cycle tensile test
b	15.8 mm	10.38 mm
h	2.2 mm	2.16 mm
L_0	50 mm	50 mm
l_1	80 mm	80 mm

Figure 4.4: Abaqus CAE specimen model with boundary conditions and characteristic points and dimensions.

strain is calculated using

$$\varepsilon = \frac{\Delta L}{L_0} = \frac{u_B - u_A}{L_0}. \tag{4.19}$$

The damage variable, healing variable, effective damage variable and effective plastic strain are measured in the middle of the specimen (point D in Figure 4.4) to minimize the effects of boundary conditions and the applied load on the results.

The CAE specimen model is discretized with linear continuum solid elements (C3D8R), with four integration points per element. Discretized models for both sets of experiments are shown in Figure 4.5. The specimen for the static tensile test is discretized with 384 C3D8 elements (693 nodes), whereas the one for the two-cycle tensile test is discretized using 256 elements (495 nodes). The convergence analysis was conducted on two-cycle tensile test specimen with four different mesh sizes resulting in 128, 256, 1600 and 3200 C3D8 elements with results showing mesh-independence. The obtained force-displacement results are almost identical and their representation in a single diagram results in coincident curves.

4.3.1. Static tensile tests on Surlyn® 8940

Numerical analysis results are compared to experimental results obtained for three specimens. Constitutive model parameters used for simulating static tensile tests are

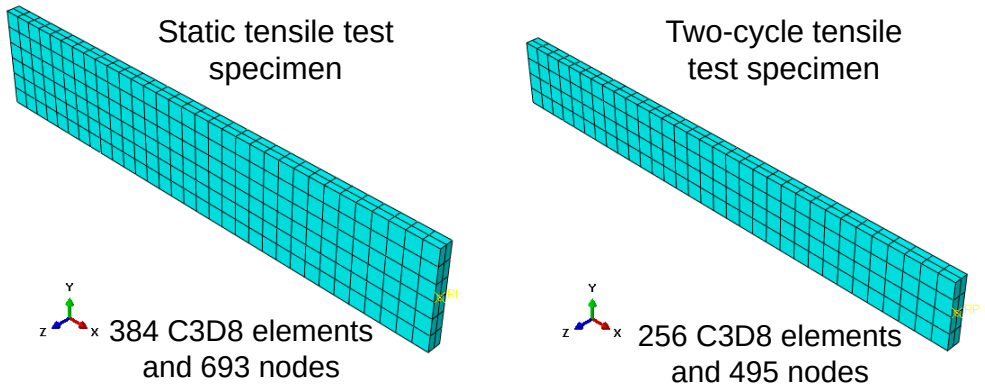

Figure 4.5: Discretized specimens for the static tensile test and the two-cycle tensile test.

given in Table 4.2. Only damage and plasticity model parameters are given, since healing does not take place during this experiment. Values of the parameters have been selected to best fit the experimental results.

The analysis results are compared with the experiments in a stress-strain diagram, Figure 4.6, whereas the damage variable and the effective plastic strain are plotted only as analysis results. The diagram in Figure 4.6 shows relatively good agreement of analysis results with experimental ones. Figure 4.7 depicts the constitutive model prediction of the evolution of the damage variable and the effective plastic strain with dependence on total strain during the static tensile test. The influence of the damage viscosity parameter on the damage variable is confirmed here, since it determines the rate of the damage variable evolution.

Table 4.2: Constitutive model parameters used for the simulation of static tensile test on Surlyn® 8940.

Parameter	**Value**
E	500 MPa
ν	0.3
Damage model	
Γ^{vd}	$1.5 \cdot 10^{-2}\mathrm{s}^{-1}$
Y_{th}	3.1 MPa
k	1
q	1
Plasticity model	
σ_{y0}	3 MPa
H	1,800 MPa

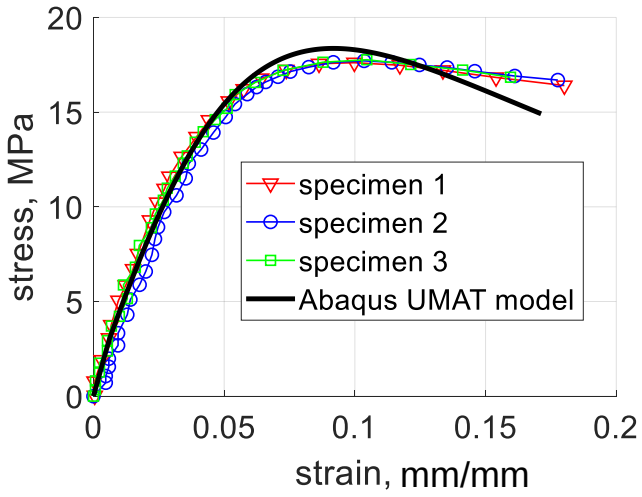

Figure 4.6: Nominal stress-strain diagram – comparison of experimental results and numerical analysis results (Abaqus UMAT model).

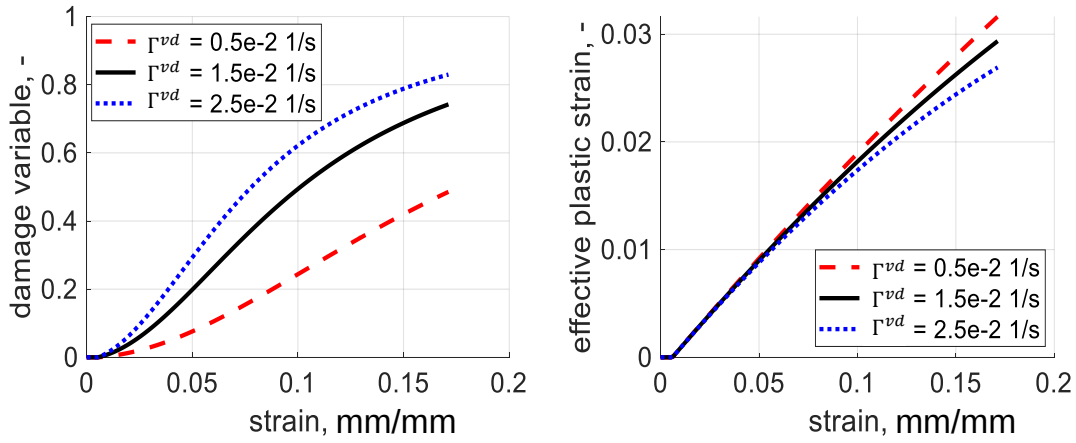

Figure 4.7: Dependence of damage variable and effective plastic strain on total strain for different values of damage viscosity parameter, Γ^{vd}, during the static tensile test.

Concerning the effective plastic strain, a linear behaviour for a von Mises linear isotropic hardening plasticity model would be expected. However, the behaviour is non-linear due to the presence of damage and it is a proof of a good coupling between the damage and plasticity models. Furthermore, Figure 4.7 shows that the greater values of the damage viscosity parameter, unlike for the damage variable, cause a slower rate of effective plastic strain. Therefore, the greater rate of effective plastic strain causes smaller rate of the damage variable and vice versa, the greater rate of the damage variable causes the

smaller rate of the effective plastic strain. That proves, once again, that the damage and plasticity models are well coupled.

4.3.2. Two-cycle tensile tests on Surlyn® 8940

Two-cycle tensile tests are performed in order to validate the healing and the plasticity part of the constitutive model. The specimen is subjected to the loading regime represented in Figure 4.8a). The specimen is loaded up to 220 N in the first cycle, healed for 5 s and loaded again, up to 260 N, in the second cycle. Here, as well as for the static tensile tests, numerical analysis results are compared to experimental results of three specimens. Constitutive model parameters are given in Table 4.3. Two parameters, Γ^{vd} and k, in Table 4.3, differ from the ones determined for the static tensile test, given in Table 4.2. The reason for this is dependence of mechanical properties of Surlyn® 8940 on thermal history. Namely, samples for static tensile tests and for two-cycle tensile tests are produced by hot compression moulding in a vacuum bag. The heat treatment of samples for static tensile tests and for two-cycle tensile tests was not identical, resulting in different thermal histories of the samples.

Table 4.3: Constitutive model parameters used for the simulation of two-cycle tensile test on Surlyn® 8940.

Parameter	**Value**
E	500 MPa
ν	0.3
Damage model	
Γ^{vd}	$6.51 \cdot 10^{-2}\,\mathrm{s}^{-1}$
Y_{th}	3.1 MPa
k	10
q	1
Healing model	
Γ^{h}	$0.7\,\mathrm{s}^{-1}$
m	2
Plasticity model	
σ_{y0}	3 MPa
H	1,800 MPa

As reported in [Varley and van der Zwaag, 2008], the influence of thermal history on mechanical properties of Surlyn® 8940 was confirmed in [Haramina et al., 2021], by

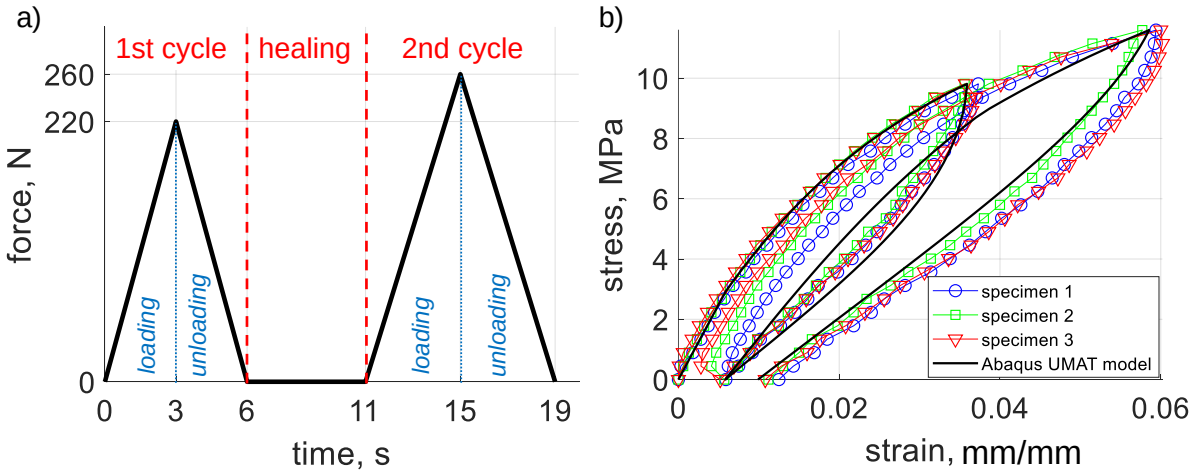

Figure 4.8: a) A schematic representation of the two-cycle loading experiment with designated cycles and loading/unloading intervals; b) A nominal stress-strain diagram – comparison of numerical analysis results (Abaqus UMAT model) and experimental results.

conducting Dynamic Mechanical Analysis (DMA) on the same batch of specimens as the ones used for static tensile tests.

Figure 4.8b) shows a comparison of analysis results with experimental results in a stress-strain diagram, and it proves good agreement of constitutive model prediction with experimental results. Some differences in the loading-unloading curves of the second cycle are present. They are caused by the fact that the displacement-measuring gauge has to be reset manually, i.e. dismounted from the specimen, reset, and mounted back to the specimen, to enable displacement measurements in the second cycle. Moreover, in Figure 4.8b) it can be seen that, at the loading-unloading point of the second loading cycle, strain is approx. 6 %. The developed constitutive model is to be implemented in a micromechanical framework for modelling of unidirectional composite materials. As these fail at relatively low strain values, experiments that would result in higher values of strain have not been considered in this Thesis. Therefore, two loading-unloading cycles are considered sufficient to draw a conclusion on the appropriateness of the constitutive model for this purpose. Figure 4.9a) shows the evolution of the damage variable, Figure 4.9b) the effective damage variable and Figure 4.10a) the evolution of the healing variable during the two-cycle tensile test. Damage, and all other variables are plotted with respect to time, because plotting with respect to strain is inconvenient in this case, since strain

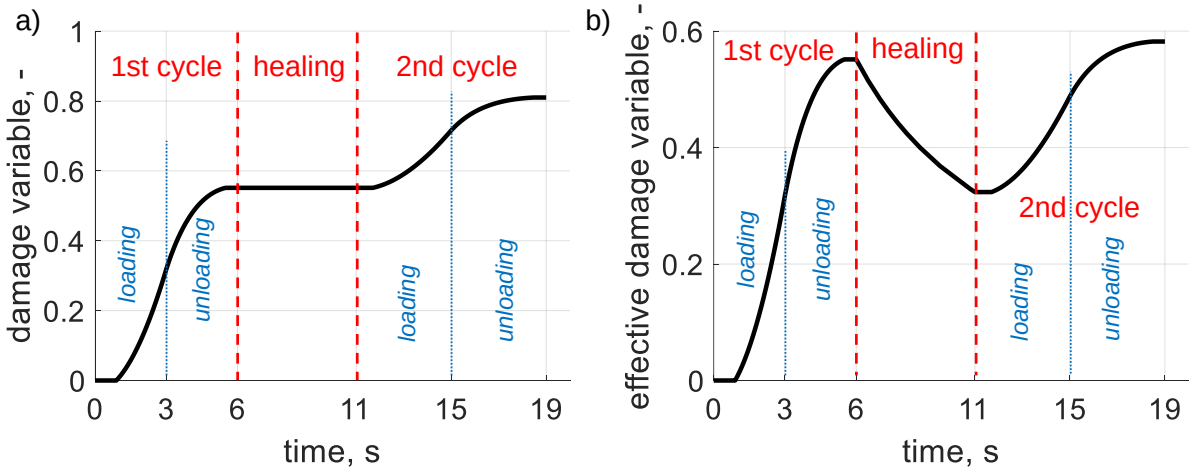

Figure 4.9: a) Evolution of the damage variable, ϕ, during the two-cycle tensile test; a constitutive model prediction with designated cycles and loading/unloading intervals; b) Evolution of the effective damage variable, ϕ_{eff}, during the two-cycle tensile test; a constitutive model prediction with designated cycles and loading/unloading intervals.

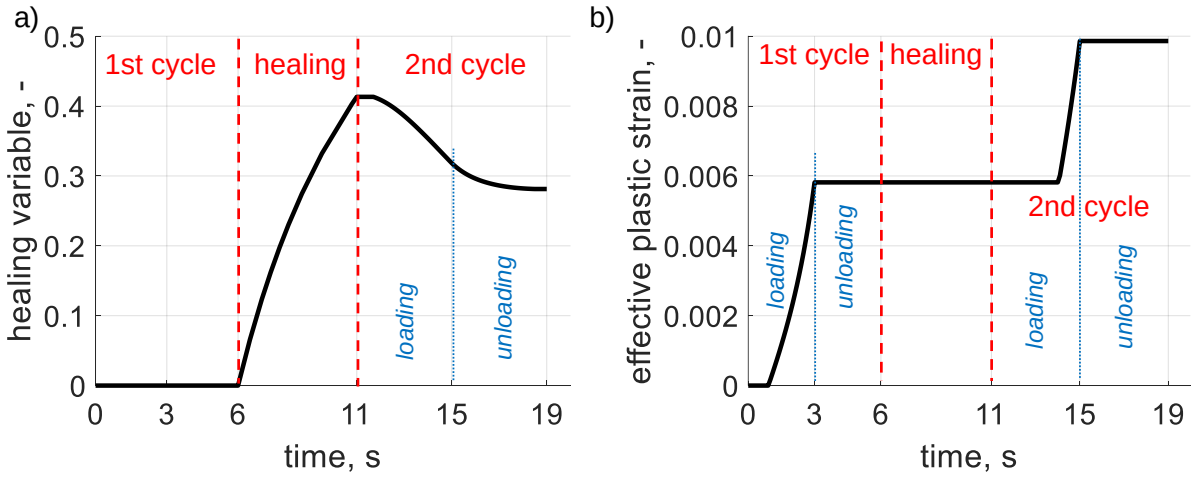

Figure 4.10: a) Evolution of the healing variable, h, during the two-cycle tensile test; a constitutive model prediction with designated cycles and loading/unloading intervals; b) Evolution of the effective plastic strain; a constitutive model prediction with designated cycles and loading/unloading intervals.

oscillates from zero to maximum value. The damage process is defined to commence after the initiation of yielding. Therefore, the damage variable increases both during the loading and unloading in both cycles, but at a slower rate during the unloading process, as long as the damage initiation criterion, Eq. 4.16, is met. Healing does not affect the damage variable, ϕ. However, the effective damage variable, $\phi_{eff} = \phi(1 - h)$, is affected

by the healing process, i.e. the healing variable, and it decreases during the healing process. The evolution of the effective plastic strain is depicted in Figure 4.10b). Even though it shows only results of the numerical analysis, plastic behaviour of the model can be validated by diagram in Figure 4.8b), where it is obvious that plastic strain predicted by the constitutive model is in good agreement with experimental results. In addition, it is to be mentioned that plastic strain increases only during the loading process, when the effective stress is higher than the current yield stress, σ_y. The yield stress increases linearly with each loading above the current yield stress, as given in Eq. 4.6. This is the reason why in the second cycle, Figure 4.10b), effective plastic strain remains constant longer than in the first one, i.e. as long as the current yield stress is not reached.

5 Multiscale modelling of intrinsically self-healing FRP composites

This chapter deals with modelling of intrinsically self-healing fibre reinforced polymer composites at the micro- and macroscale. Furthermore, the chapter includes validation of the developed constitutive model for two loading-healing cases: (i) healing after 3PB test as validation of the model for static loading cases and (ii) healing after LVI as validation of the model for dynamic loading cases.

5.1. Constitutive model description

The developed constitutive model is a multiscale model which employs the rule of mixture (ROM) equations as a means for homogenisation, and Voigt iso-strain and Reuss iso-stress approximations as a means for localisation, [Goldberg, 1999]. At the microscale, each constituent, reinforcing fibres and the matrix material, is modelled separately. The reinforcing fibres are modelled as transversely isotropic linear elastic material with maximum stress failure criterion and a progressive damage model taken from [Lapczyk and Hurtado, 2007]. The matrix material is modelled using the previously developed and validated constitutive model for the intrinsically self-healing polymer material. In the following text, modelling of the reinforcing fibres at the microscale is described. It is followed by a thorough report on applied homogenisation and localisation techniques. Detailed description of the model for the matrix constituent is given in Chapter 4. and, thus is here omitted.

5.1.1. Reinforcing fibres at the microscale

The reinforcing fibres are modelled as transversely isotropic linear elastic material with maximum stress failure criterion and progressive damage model. The adopted damage model is the one from [Lapczyk and Hurtado, 2007]. Damage initiation is governed by the maximum stress failure criterion which is used in the following form

$$F_f^t = \frac{\sigma_{11}^f}{X_f^T} \text{ and } F_f^c = \frac{\sigma_{11}^f}{X_f^C}, \tag{5.1}$$

for fibre tension and fibre compression, respectively. In Eq. (5.1), σ_{11}^f is the longitudinal fibre stress, X^T is the fibre tensile strength, and X^C is the fibre compressive strength. After the initiation of fibre damage, ϕ_f, its evolution in the case of both tension and compression is after [Lapczyk and Hurtado, 2007] defined as

$$\phi_f = \frac{\delta_{eq}^f(\delta_{eq} - \delta_{eq}^0)}{\delta_{eq}(\delta_{eq}^f - \delta_{eq}^0)}, \tag{5.2}$$

where

δ_{eq}^0 is the fibre initial equivalent displacement at which the initiation criterion for specific failure mode was met;

δ_{eq}^f is the equivalent displacement at which the material has ruptured in specific failure mode;

δ_{eq} is the current fibre equivalent displacement for specific failure mode.

Each of these parameters has different values for tensile and compressive failure. Value of δ_{eq}^0 is determined during the analysis, and it gets the value of δ_{eq}^f when the tensile or compressive failure criterion is met. Value of δ_{eq}^f for compressive and tensile failure mode is determined experimentally. Finally, the current fibre equivalent displacement, δ_{eq}, in the case of tension is calculated as

$$\delta_{eq}^T = L^C \sqrt{(\varepsilon_{11}^f)^2 + (\varepsilon_{12}^f)^2}, \tag{5.3}$$

where ε_{11}^f and ε_{12}^f are components of the fibre strain tensor and L^C is the characteristic finite element length. For the case of compressive failure, it is calculated as

$$\delta_{eq}^C = L^C |\varepsilon_{11}^f|. \tag{5.4}$$

5.1.2. Homogenisation

Orthotropic elasticity tensor is used for modelling of the homogenised composite material. For this, the Rule of Mixtures equations for calculation of mechanical properties of the homogenised composite are used in this work. Thus, longitudinal elasticity modulus, E_{11}, transverse elasticity modulus, E_{22}, Poisson's ratio, ν_{12}, and in-plane shear modulus, G_{12}, of the homogenised composite material are calculated as

$$E_{11} = E_{11}^f V^f + E^m(1 - V^f), \tag{5.5}$$

$$\frac{1}{E_{22}} = \frac{V^f}{E_{22}^f} + \frac{1 - V^f}{E^m}, \tag{5.6}$$

$$\nu_{12} = \nu_{12}^f V^f + \nu^m(1 - V^f), \tag{5.7}$$

$$\frac{1}{G_{12}} = \frac{V^f}{G_{12}^f} + \frac{1 - V^f}{G^m}. \tag{5.8}$$

In Eqs. (5.5)-(5.8),

E_{11}^f is the longitudinal elasticity modulus of reinforcing fibres;
E_{22}^f is the transverse elasticity modulus of reinforcing fibres;
ν_{12}^f is the Poisson's ratio of the reinforcing fibres;
G_{12}^f is the in-plane shear modulus of the reinforcing fibres;
E^m is the elasticity modulus of the matrix material;
ν^m is the Poisson's ratio of the matrix material and
G^m is the shear modulus of the matrix material.

To fully define the orthotropic elasticity tensor for three-dimensional analyses, E_{33}, ν_{13}, ν_{23}, G_{23} and G_{13} are missing, but can be defined as

$$E_{33} = E_{22}, \tag{5.9}$$

$$\nu_{13} = \nu_{12}, \tag{5.10}$$

$$G_{13} = G_{12}, \tag{5.11}$$

and values of G_{23} and ν_{23} are determined experimentally or taken from the literature. In this Thesis, the latter is opted.

Input for the user material subroutine VUMAT is the total strain increment tensor $d\boldsymbol{\varepsilon}$. It represents the strain increment of the homogenised composite material at the

macroscale. Total strain increment of the homogenised composite $d\boldsymbol{\varepsilon}$ is decomposed into elastic and plastic components as

$$d\boldsymbol{\varepsilon} = d\boldsymbol{\varepsilon^{el}} + d\boldsymbol{\varepsilon^{pl}}. \tag{5.12}$$

In Eq. (5.12) elastic strain increment $d\boldsymbol{\varepsilon^{el}}$ and plastic strain increment $d\boldsymbol{\varepsilon^{pl}}$ are unknown. Components of the plastic strain increment tensor $d\boldsymbol{\varepsilon^{pl}}$ are calculated using the values of plastic strain tensor of the matrix material as

$$d\varepsilon_{11}^{pl} = d\varepsilon_{11}^{m,pl}, \tag{5.13}$$

$$d\varepsilon_{ii}^{pl} = d\varepsilon_{ii}^{m,pl} \cdot (V^f \cdot \frac{E^m}{E_{ii}^f} + (1 - V^f)), \text{ where } i = 2, 3; \tag{5.14}$$

$$d\gamma_{ij}^{pl} = d\gamma_{ij}^{m,pl} \cdot (V^f \cdot \frac{G^m}{G_{ij}^f} + (1 - V^f)), \text{ where } i, j = 1, 2, 3. \tag{5.15}$$

Equations (5.13) - (5.15) are derived using the Voigt iso-strain and Reuss iso-stress assumptions, analogously to derivation of equations (5.17) and (5.19) in Section 5.1.3.. With known values of the plastic strain increment tensor, elastic strain increment tensor can easily be obtained from Eq. (5.12).

5.1.3. Localisation

Successful modelling of the matrix constituent and the reinforcing fibres at the microscale requires decomposition of the total strain increment, $d\boldsymbol{\varepsilon}$, into fibre strain increment tensor, $d\boldsymbol{\varepsilon^f}$, and the matrix material strain increment tensor, $d\boldsymbol{\varepsilon^m}$. This decomposition is based on the Voigt iso-strain and the Reuss iso-stress approximations.

The Voigt iso-strain approximation is used for 1-direction i.e., direction of the reinforcing fibres. This means that the fibres and the matrix material deform equally in 1-direction. Thus, the total, fibre and matrix strain increment tensor components are defined using the iso-strain assumption as

$$d\varepsilon_{11}^m = d\varepsilon_{11}^f = d\varepsilon_{11}. \tag{5.16}$$

For the case of normal stress components σ_{22}, σ_{33} and shear stress components τ_{ij}, the Reuss iso-stress assumption is utilised. This implies that the matrix, fibre and

homogenised stress components are correlated as

$$d\sigma_{ii}^{m} = d\sigma_{ii}^{f} = d\sigma_{ii}, \text{ where } i = 2, 3; \tag{5.17}$$

$$d\varepsilon_{ii}^{f} = \frac{E^{m}}{E_{ii}^{f}} \cdot d\varepsilon_{ii}^{m}, \text{ where } i = 2, 3; \tag{5.18}$$

$$d\tau_{ij}^{m} = d\tau_{ij}^{f} = d\tau_{ij}, \text{ where } i, j = 1, 2, 3; \tag{5.19}$$

$$d\tau_{ij}^{f} = \frac{G^{m}}{G_{ij}^{f}} \cdot d\tau_{ij}^{m} \text{ where } i, j = 1, 2, 3. \tag{5.20}$$

Equations (5.17) and (5.19) imply the following form of the strain increment tensor

$$(1 - V^{f}) \cdot d\varepsilon_{ii}^{m} + V^{f} \cdot d\varepsilon_{ii}^{f} = d\varepsilon_{ii}, \text{ where } i = 2, 3; \tag{5.21}$$

$$(1 - V^{f}) \cdot d\gamma_{ij}^{m} + V^{f} \cdot d\gamma_{ij}^{f} = d\gamma_{ij}, \text{ where } i, j = 1, 2, 3. \tag{5.22}$$

Solving equations (5.21) and (5.22) for $d\varepsilon_{ii}^{m}$ and $d\gamma_{ij}^{m}$ by applying the Reuss iso-stress assumption, equations (5.18) and (5.20), yields

$$d\varepsilon_{ii}^{m} = \frac{d\varepsilon_{ii}}{V^{f} \cdot \frac{E^{m}}{E_{ii}^{f}} + (1 - V^{f})}, \text{ where } i = 2, 3; \tag{5.23}$$

and

$$d\gamma_{ij}^{m} = \frac{d\gamma_{ij}}{V^{f} \cdot \frac{G^{m}}{G_{ij}^{f}} + (1 - V^{f})}, \text{ where } i, j = 1, 2, 3. \tag{5.24}$$

Components of the matrix strain increment tensor $d\boldsymbol{\varepsilon}^{m}$ are defined with equations (5.16), (5.23) and (5.24). Since the matrix constituent can be deformed plastically, total matrix strain increment $d\boldsymbol{\varepsilon}^{m}$ is decomposed into matrix plastic strain $d\boldsymbol{\varepsilon}^{m,pl}$ and matrix elastic strain $d\boldsymbol{\varepsilon}^{m,el}$ as

$$d\boldsymbol{\varepsilon}^{m} = d\boldsymbol{\varepsilon}^{m,el} + d\boldsymbol{\varepsilon}^{m,pl}. \tag{5.25}$$

In Eq. (5.25) the matrix plastic strain increment tensor $d\boldsymbol{\varepsilon}^{m,pl}$ is defined by the von Mises linear isotropic hardening plasticity model and the matrix elastic strain increment tensor can be easily obtained. Since the reinforcing fibres are linear elastic, fibre strain increment tensor is obtained combining equations (5.18) and (5.23) which yields

$$d\varepsilon_{ii}^{f} = \frac{E^{m}}{E_{ii}^{f}} \cdot \frac{d\varepsilon_{ii}}{V^{f} \cdot \frac{E^{m}}{E_{ii}^{f}} + (1 - V^{f})}, \text{ where } i = 2, 3. \tag{5.26}$$

Furthermore, in Eq. (5.26) the total homogenised composite strain increment $d\varepsilon_{ii}$ is replaced with elastic homogenised composite strain increment $d\varepsilon_{ii}^{el}$, which is defined with Eq. (5.12), the additive decomposition of total strain increment $d\boldsymbol{\varepsilon}$. This replacement is necessary, since the reinforcing fibres are modelled as linear elastic, which means that no inelastic strains are allowed. The same is applied to the fibre shear strain increment components by combining equations (5.20) and (5.24), and to the fibre strain increment in 1-direction, keeping the Voigt iso-strain approximation. Finally, expressions defining components of the fibre strain increment tensor are given as

$$d\varepsilon_{11}^{f} = d\varepsilon_{11}^{el}, \tag{5.27}$$

$$d\varepsilon_{ii}^{f} = \frac{E^{m}}{E_{ii}^{f}} \cdot \frac{d\varepsilon_{ii}^{el}}{V^{f} \cdot \frac{E^{m}}{E_{ii}^{f}} + (1 - V^{f})}, \text{ where } i = 2, 3; \tag{5.28}$$

$$d\gamma_{ij}^{f} = \frac{G^{m}}{G_{ij}^{f}} \cdot \frac{d\gamma_{ij}^{el}}{V^{f} \cdot \frac{G^{m}}{G_{ij}^{f}} + (1 - V^{f})}, \text{ where } i, j = 1, 2, 3. \tag{5.29}$$

5.2. Static loading validation - healing after three point bending test

For the purpose of static loading validation, experimental results of short span three-point bending tests, available in [Park et al., 2010], are used. These results have been previously published in [Smojver et al., 2022b]. Tested specimens consist of thermally mendable bis-maleimide tetrafuran (2MEP4F) as the matrix constituent, and GA045 unidirectional carbon fibres as reinforcements. The layup sequence of composite specimens is [0/90/0] and the fibre volume fraction is $V^{f} = 0.46$.

In [Park et al., 2010], three specimens are subjected to three-point bending experiments. During experiments on specimens 2 and 3, a thin aluminium plate, placed between the loading nose and the specimen, was used to prevent fibre breakage. On the other hand, specimen 1 was tested without the aluminium plate and thus, it suffered fibre breakage. In this case, fibre failure and damage are not considered, which is why specimen 1 experimental results are not utilised. On the other hand, as reported in [Park et al., 2010], the quality of sample 2 was not appropriate, meaning that it exhibited too low flexural stiffness when compared to specimens 1 and 3. Hence, experimental results of specimen 3 are used for validation purposes in this work.

Table 5.1: Matrix material and reinforcing fibres mechanical properties used in Abaqus analyses of healing after 3PB test.

2MEP4F		GA045		Aluminium	
E	4.14 GPa	E_{11}	228 GPa	E	70 GPa
ν	0.36	E_{22}	15 GPa	ν	0.33
σ_{y0}	118 MPa	ν_{12}	0.2	ρ_{Al}	2700 kg/m^3
ρ_{2MEP4F}	1,310 kg/m^3	ν_{23}	0.4		
		G_{12}	15 GPa		
		G_{23}	7 GPa		
$\rho_{CFRP} = 1276$kg/m^3					

Matrix constituent mechanical properties – elasticity modulus, Poisson's ratio, yield stress and density are taken from [Chen et al., 2003]. After thorough literature research, fibres' longitudinal elasticity modulus $E_{11} = 228$ GPa, and fabric areal weight $\rho_{GA045} = 104.3$ g/m^2, are taken from the manufacturer's website [Hexcel, 2021]. The rest of the mechanical properties of GA045 fibres are taken as for T300 UD carbon fibres since they exhibit similar elasticity modulus E_{11}. T300 mechanical properties are taken from [Zhao et al., 2019]. Constituents' mechanical properties and the averaged CFRP composite density, ρ_{CFRP}, as well as aluminium mechanical properties are given in Table 5.1. Using the matrix material density ρ_{2MEP4F}, carbon fibres' areal weight ρ_{GA045}, specimen dimensions given in Figure 5.1, and fibre volume fraction V_f, density of the composite ρ_{CFRP} is calculated. The experimental setup for a three-point bending test requires two supports and a loading nose. Additionally, in experiments conducted in [Park et al., 2010], an aluminium plate is placed between the loading nose and the specimen to prevent fibre breakage. The Abaqus model, along with specimen, aluminium plate, loading nose and supports' dimensions, and boundary conditions are given in Figure 5.1. The aluminium plate is 10.5 mm in length, 5 mm in width and 0.5 mm in thickness. The specimen is partitioned through thickness in three parts to enable modelling of its layup sequence. In order to prevent displacements of a rigid body, symmetry boundary conditions are defined on the specimen and the aluminium plate, in the plane of symmetry which splits the length l of the specimen and width of the aluminium plate in half, Figure 5.1. Additionally, gravity load with gravitational acceleration defined in negative z direction, - 9.807 m/s^2, is applied on the specimen and the aluminium plate to ensure numerical stability of the analysis during the healing steps.

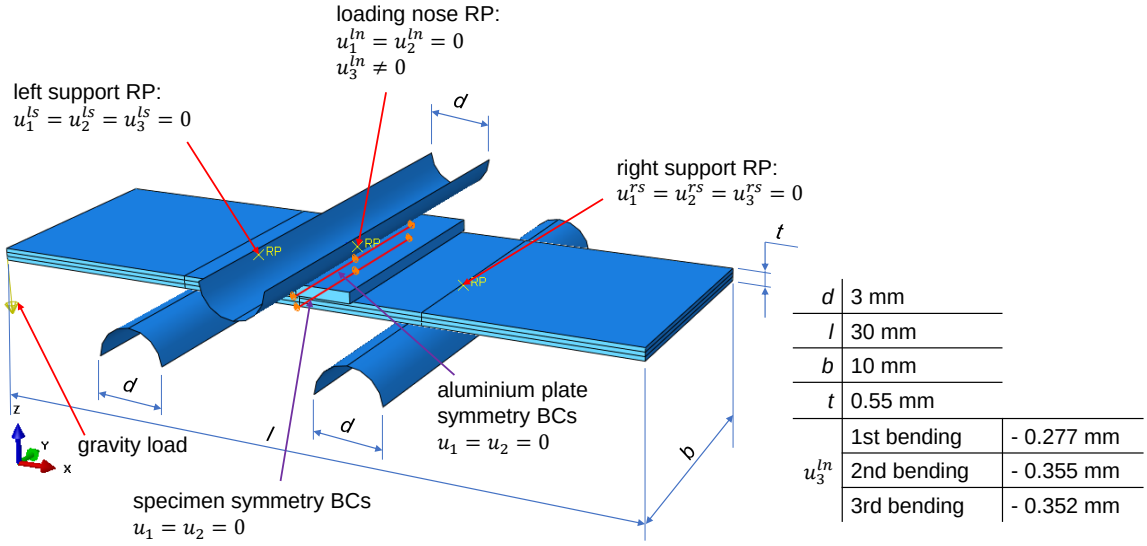

d	3 mm	
l	30 mm	
b	10 mm	
t	0.55 mm	
u_3^{ln}	1st bending	- 0.277 mm
	2nd bending	- 0.355 mm
	3rd bending	- 0.352 mm

Figure 5.1: Abaqus model of the experimental setup with designated specimen, supports and loading nose dimensions as well as boundary conditions; the aluminium plate is used due to the reference used as a data source, [Park et al., 2010].

Table 5.2: Outline of the 3PB test experiment and its equivalent numerical analysis.

	Abaqus analysis		**experiment**
	loading nose displacement, mm	*time*, s	*time*, s
1st bending	-0.277	16.62	16.62
1st healing period	0	1	3,600
2nd bending	-0.355	21.3	21.3
2nd healing period	0	2	7,200
3rd bending	-0.352	21.12	21.12

In the experiment, specimen 3 is loaded with constant loading speed of 1 mm/min, according to ASTM D7264, up to total loading nose displacement of 0.277 mm in the first bending. Then, the specimen is left to heal for 1 h. Afterwards it is loaded at the same loading speed up to the total loading nose displacement of 0.355 mm. Then it is healed again for 2 h. Finally, it is loaded for the third time at the same loading speed up to the total loading nose displacement of 0.352 mm. The outline of the experiment is given in Table 5.2. In Figure 5.1 displacements of the loading nose are given according to the provided coordinate system. That is why displacement values are negative.

In Abaqus analyses, the experiment is divided into seven steps:

1. first bending,

2. unloading,
3. first healing,
4. second bending,
5. unloading,
6. second healing, and
7. third bending.

Furthermore, duration of experimental healing periods is scaled to save the computational time. Thus, healing periods in the analysis last 1 s and 2 s instead of 1 h and 2 h, see Table 5.2. Accordingly, the healing model parameters are scaled and used only during the healing periods – steps (3) and (6). Scaled healing parameters are determined so that the healing process after 1 s and 2 s results in the same regain of flexural stiffness as when using the non-scaled parameters after 1 h and 2 h of healing, using experimental results from [Park et al., 2010] as a reference. Non-scaled healing parameters are used during the bending periods – steps (1), (2), (4), (5) and (7). As previously mentioned, the healing process initiates when strain rate is equal to zero. Since some integration points can have the strain rate equal to zero even during the bending periods, healing can be initiated, and non-scaled healing parameters have to be used. Damage, healing and plasticity model parameters of the matrix constituent used for the validation are given in Table 5.3. Loading nose and supports are modelled using the *analytical rigid*

Table 5.3: Damage, healing and plasticity model parameters of the matrix constituent used in Abaqus analyses of healing after 3PB test.

Damage model	
Γ^{vd}	$6.11 \cdot 10^{-2}\,\mathrm{s}^{-1}$
Y_{th}	3.1 MPa
k	-4
q	1
Healing model	
Γ^{h}	$0.153\,\mathrm{s}^{-1}$
m	2
Scaled healing parameters	
Γ^{h}	$221.2\,\mathrm{s}^{-1}$
m	2
Plasticity model	
σ_{y0}	118 MPa
H	1,800 MPa

surface option in Abaqus and they are linked to their reference points (RP), Figure 5.1 using the *rigid body* constraint. Surface-to-surface contact is defined on the following contact surfaces:

- loading nose-aluminium plate,
- aluminium plate-specimen,
- left support-specimen, and
- right support-specimen,

whereby the specimen surfaces are defined as *slave* surfaces. Contact interaction property is defined as *normal behaviour* with *hard contact*, without friction.

The specimen is discretized with 7440 linear continuum solid (C3D8R) elements (10332 nodes) with reduced integration. Each composite ply is discretized with one finite element through thickness, resulting in three finite elements through thickness of the specimen. On the other hand, the aluminium plate is discretized with 2520 continuum shell (SC8R) elements (3612 nodes). Discretized specimen and the aluminium plate with analytical rigid surfaces are shown in Figure 5.2. Regions of the specimen that do not lay between the supports are discretized with a coarser mesh since they do not influence the results.

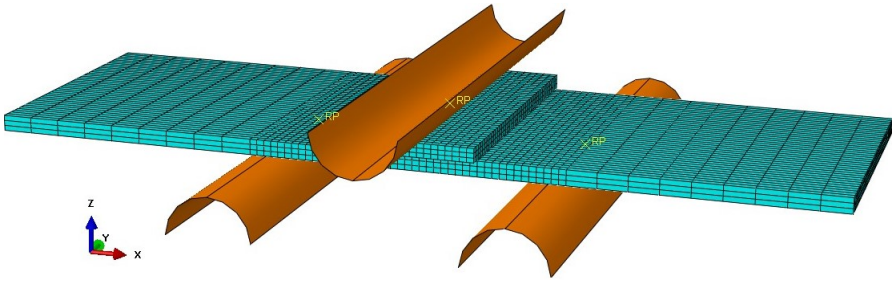

Figure 5.2: 3PB test specimen discretized with 7440 linear continuum solid elements (10332 nodes) and the aluminium plate discretized with 2520 continuum shell elements (3612 nodes).

5.2.1. Validation results and discussion

In Figure 5.3 numerical model predictions for specimen 3 are compared with experimental results in a force-displacement diagram. Measured displacement is displacement of the loading nose, and the measured force is contact force between the loading nose and the aluminium plate. Very good agreement of analysis with experimental results is achieved. The developed constitutive model can accurately describe the micro-damaging

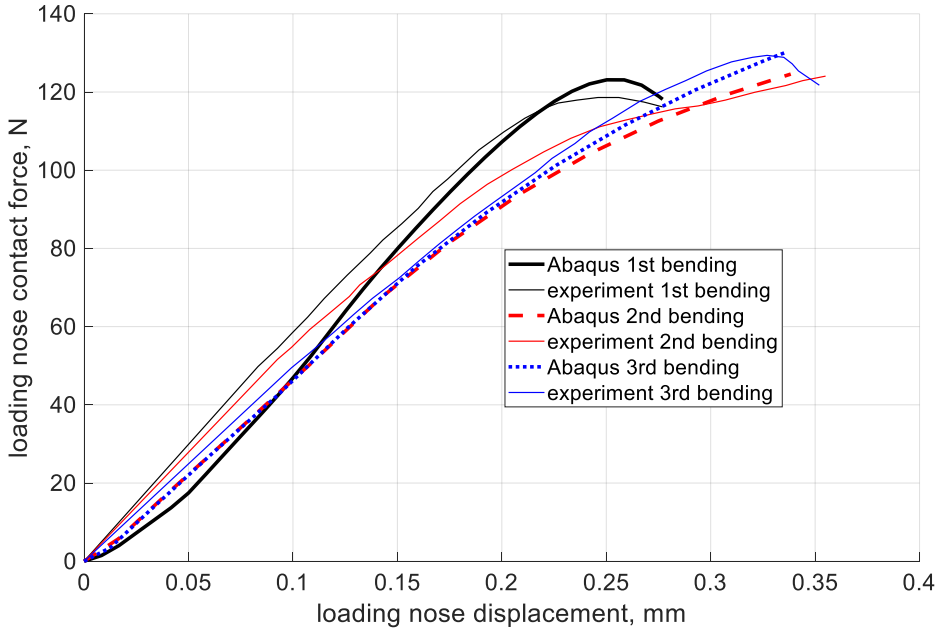

Figure 5.3: Specimen 3 three-point bending test force-displacement diagrams, model validation results - comparison of analysis and experimental results.

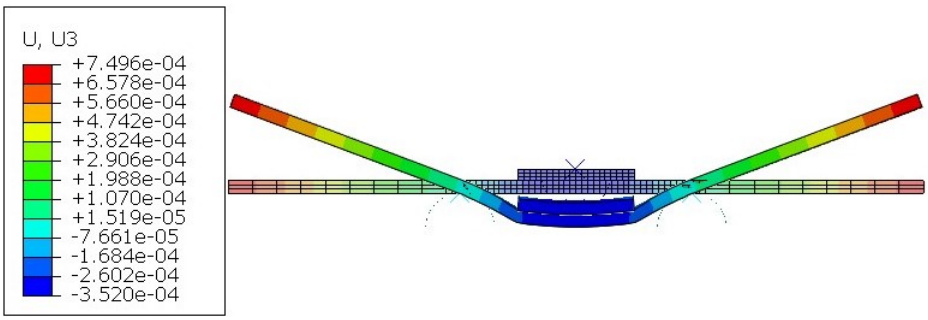

Figure 5.4: Specimen and aluminium plate displacements [m] in z-direction (U3) plotted on their deformed and undeformed shapes, deformation scale factor = 5.

and the healing mechanisms in intrinsically self-healing fibre reinforced composite structures, i.e. in UD CFRP composite with bis-maleimide tetrafuran (2MEP4F) as a matrix material. Furthermore, deformed and undeformed shapes of the specimen and the aluminium plate are given in Figure 5.4 along with distribution of displacements in z-direction (U3) at the end of the third bending. Distribution of the effective damage variable in the 90-degree (middle) ply and in 0-degree plies (top and bottom) is given at the beginning and at the end of the first healing cycle in Figure 5.5. Distribution of the

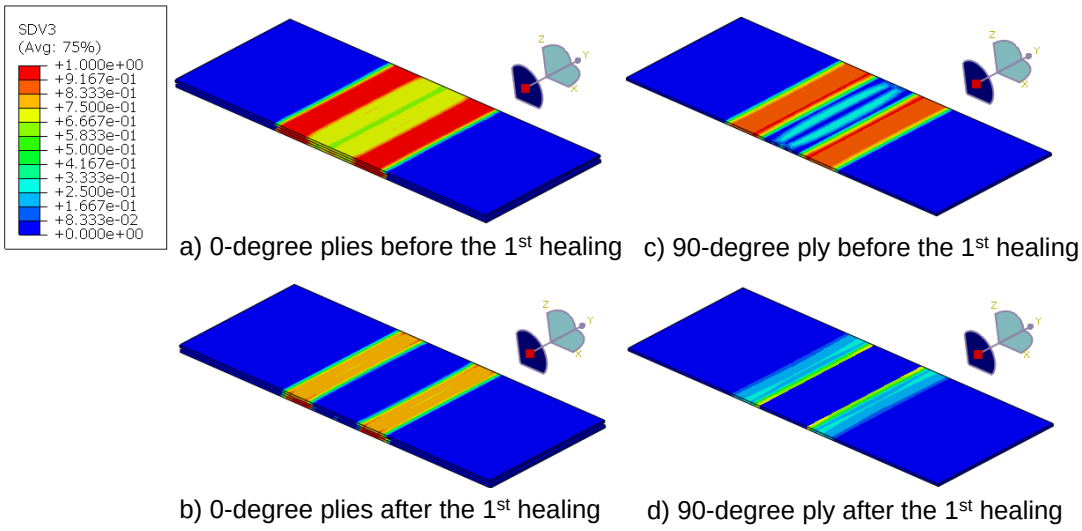

Figure 5.5: Distribution of the effective damage variable, ϕ_{eff} [-], in 0-degree plies (top and bottom) and 90-degree (middle) ply; a) 0-degree plies at the beginning and b) at the end of the first healing; c) 90-degree ply at the beginning and d) at the end of the first healing. Deformation scale factor = 1.

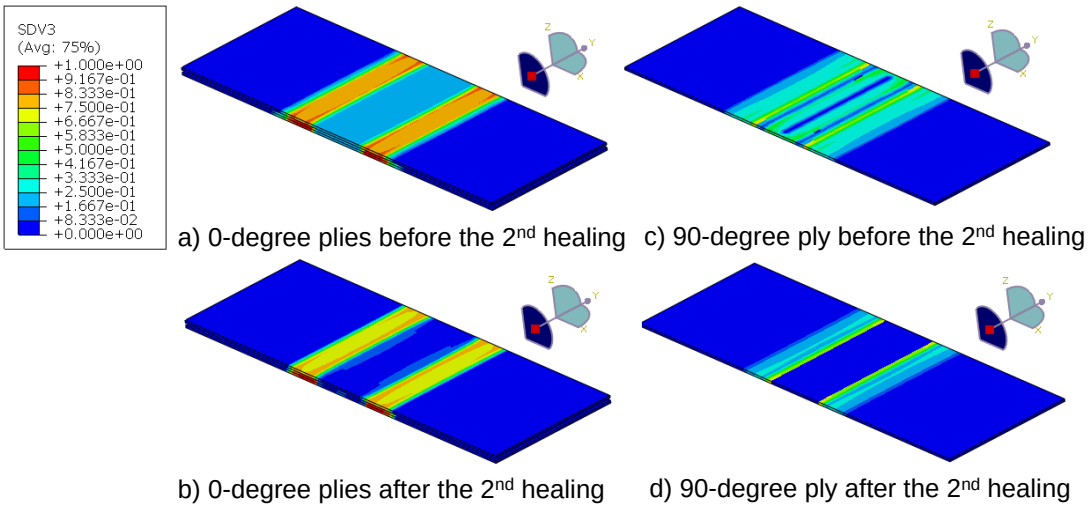

Figure 5.6: Distribution of the effective damage variable, ϕ_{eff} [-], in 0-degree plies (top and bottom) and 90-degree (middle) ply; a) 0-degree plies at the beginning and b) at the end of the second healing; c) 90-degree ply at the beginning and d) at the end of the second healing. Deformation scale factor = 1.

effective damage variable in the 90-degree (middle) ply and in 0-degree plies (top and bottom) before and after the second healing is given in Figure 5.6.

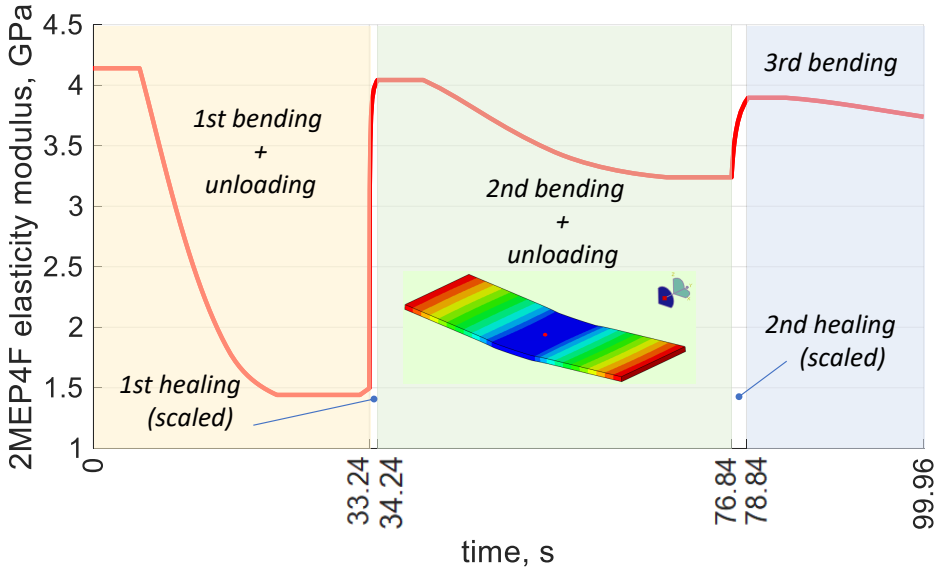

Figure 5.7: Evolution of the matrix material (2MEP4F) elasticity modulus during the analysis in an element in the middle of the specimen, upper 0-degree ply.

The healing phenomenon reduces micro-damage in critical sections of the specimen resulting in the regain of specimen's flexural stiffness. This regain of specimen's flexural stiffness is a direct consequence of the recovery of matrix material elasticity modulus. Diagram showing reduction of the matrix material elasticity modulus during the damaging processes and it's increase during the healing processes is given in Figure 5.7. It can also be seen that the healing is not complete even after 3 h of healing in total, i.e. there are still some damaged regions of the specimen.

5.2.2. Parametric analysis

Parametric analysis is conducted to demonstrate the influence of damage and healing model parameters on the numerical analysis predictions. Furthermore, it is used to present the capabilities of the constitutive model and to provide a physical representation of each model parameter. The analysis is carried out on the specimen defined in Figure 5.1.

Micro-damage model parametric analysis is performed on the first bending. Force-displacement diagrams obtained by varying parameters Γ^{vd} and k are given in Figure 5.8. During the analyses, remaining parameters are kept constant at values defined in Table

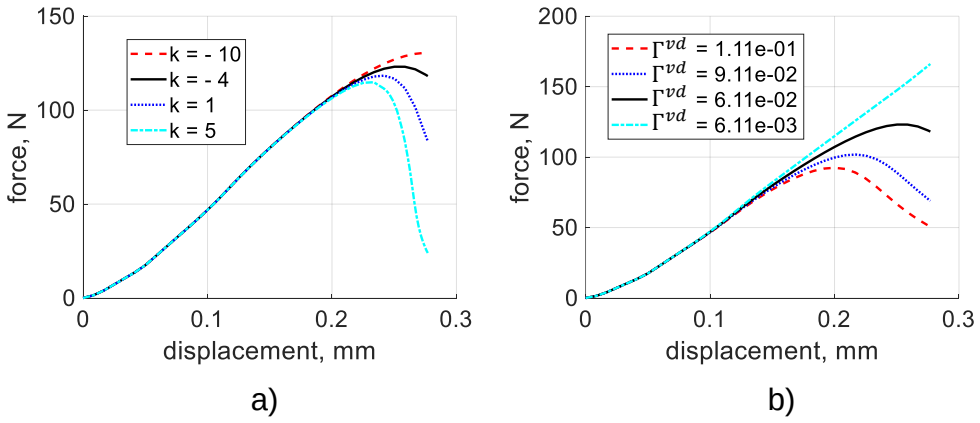

Figure 5.8: Force-displacement diagrams obtained by varying damage model parameters Γ^{vd} and k; a) variation of parameter k; b) variation of parameter Γ^{vd}.

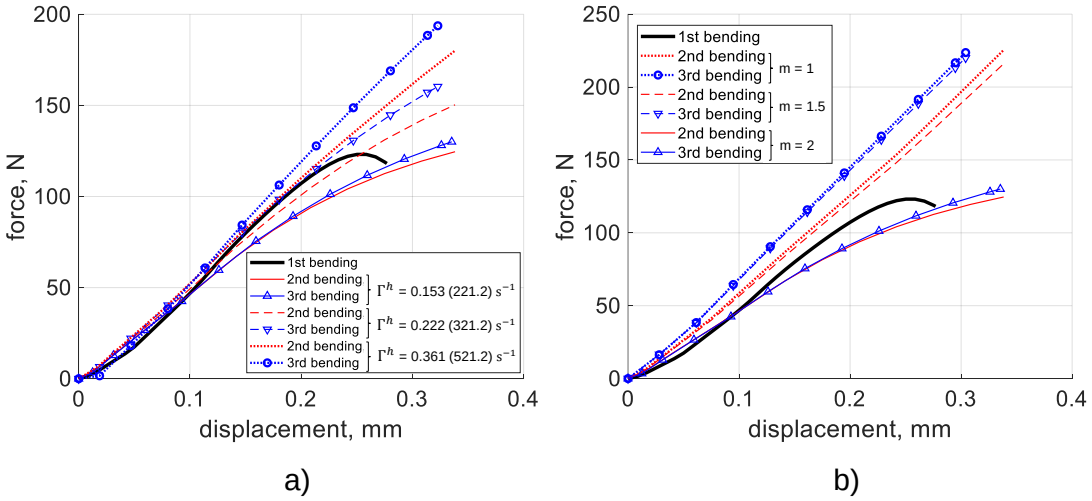

Figure 5.9: Force-displacement diagrams obtained by varying healing model parameters Γ^h and m; a) variation of parameter Γ^h; b) variation of parameter m.

5.3. Validation results obtained using set of parameters defined in Table 5.3 are plotted as a black solid line. As previously mentioned, the onset of damage is controlled by the threshold damage force Y_{th}. However, post damage-initiation behaviour is controlled by parameters Γ^{vd} and k. Their influence on material behaviour is depicted in Figure 5.8.

Variation of healing parameters, Γ^h and m, and their influence on results in force-displacement diagram is given in Figure 5.9, whereas other parameters are kept constant as defined in Table 5.3. First bending is the same for all three cases of healing parameters variation and it is plotted as a black solid line. Validation results obtained using set of

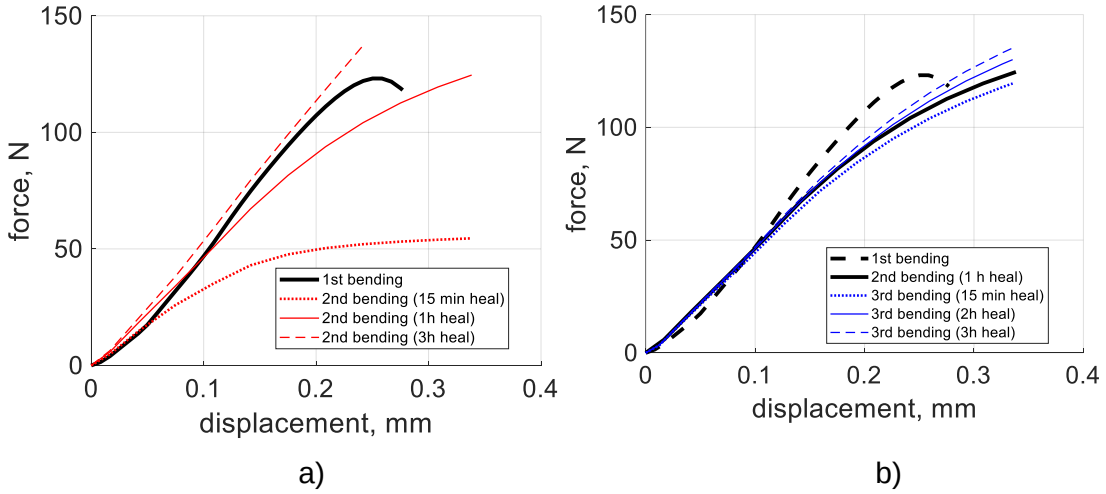

Figure 5.10: Force-displacement diagrams obtained by varying duration of the healing periods; a) variation of duration of the first healing period (15 min, 1 h and 3 h); b) variation of duration of the second healing period (15 min, 2 h and 3 h).

parameters defined in Table 5.3 are plotted as red solid lines (2^{nd} bending) and blue solid lines with triangles (3^{rd} bending). In Figure 5.9 it can be seen that parameter m is used for rough calibration on the healing model, whereas the parameter Γ^h is utilised for fine tuning.

Additionally, duration of healing periods is varied, and the results are given in Figure 5.10. The applied model parameters are the ones defined in Table 5.3. In Figure 5.10a a force-displacement diagram obtained by variation of duration of the first healing period is given. Results of the first bending are plotted as a black solid line. In Figure 5.10b duration of the second healing period is varied. Here the results of the first bending are plotted with a black dashed line, and the results of the second bending are plotted as a black solid line. It can be seen in Figure 5.10 that the effect of the duration of healing is prominent in the first healing period when there is no previously healed damage in the specimen. On the other hand, effect of the duration of healing on the second healing period is not as prominent as on the first one since the healing variable reached a saturated value. Finally, as it is the case with experimental results in [Park et al., 2010], the longer healing period results in higher regain of stiffness.

Based on the provided parametric analysis, it is concluded that there is a high degree of control over the constitutive model. Thus, it can be used to describe material behaviour of various UD FRP composites with self-healable matrix constituent.

5.3. Dynamic loading validation - healing after low velocity impact

The described constitutive model is validated using the LVI experimental results available in [Cohades and Michaud, 2017b]. Validation results have been previously published in [Smojver et al., 2022a]. Composite specimens subjected to impact tests consisted of woven twill 2x2 E-glass fabric and a blend of Epon^{TM}828EL epoxy resin and 25vol% of poly(ε-caprolactone) (PCL) as the matrix constituent. Specimens' layup consisted of 16 woven plies i.e., $[\pm 45/(0/90)_2/\pm 45]_4$ where (0/90) and ± 45 each represent a single woven ply. Fibre volume fraction of produced composite plates is $V^f = 0.48$ and they are cut to 350x250 mm impact specimens.

Impact tests are conducted according to ASTM 7136 standard for LVI tests. The standard requires the specimen to be simply supported at a base with a cut-out. The impactor has a mass of 5.5 kg and its spherical tip is 16 mm in diameter. Abaqus model of the experimental setup is given in Figure 5.11 along with boundary conditions, dimensions and discretization details. In the analysis, the impactor is modelled as a rigid sphere shell with mass and diameter as defined in ASTM 7136. The base is modelled as a rigid shell, 500x500 mm, with a cut-out of 125x75 mm.

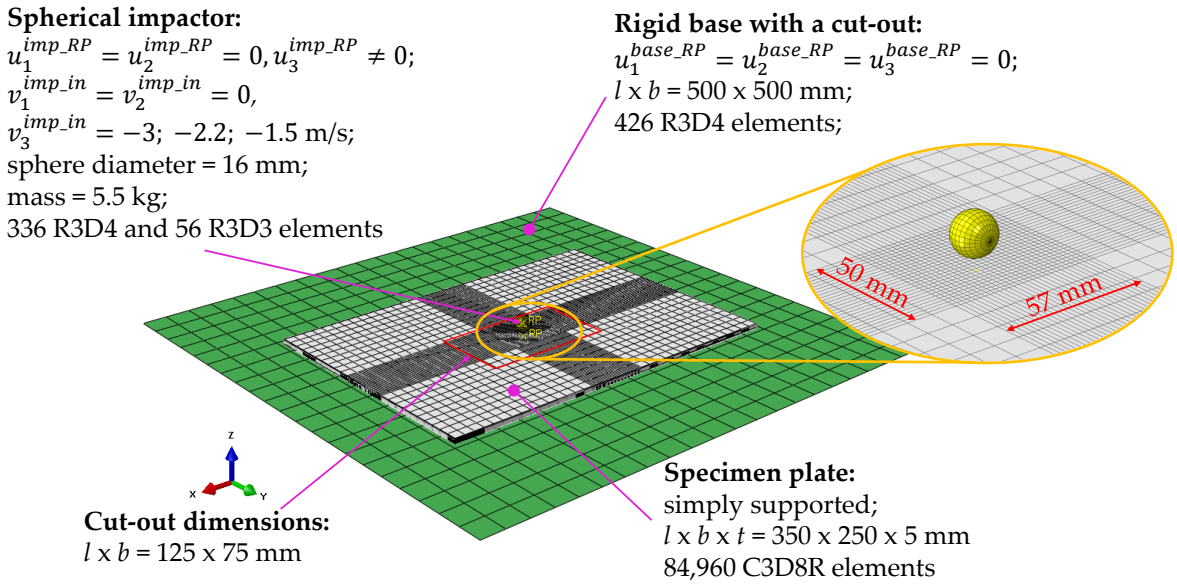

Figure 5.11: Discretized Abaqus model of the LVI experimental setup with main dimensions, boundary conditions and discretization details.

Table 5.4: GFRP constituents' mechanical properties used in Abaqus analyses of healing after LVI.

828EL + 25 vol% PCL		**UD E-glass fibre**	
E	1.58 GPa	E_{11}	72 GPa
ν	0.4	E_{22}	12.1 GPa
σ_{y0}	10 MPa	ν_{12}	0.09
ρ_{828EL}	1,340 kg/m^3	ν_{23}	0.22
ρ_{PCL}	1,145 kg/m^3	G_{12}	33 GPa
		G_{23}	5 GPa
		$\rho_{E-glass}$	2,550 kg/m^3
		X_f^T	2,000 MPa
		X_f^C	3,103 MPa

$\rho_{GFRP} = 1,895$ kg/m^3

Rigid base is discretized with 426 R3D4 elements, spherical impactor with 336 R3D4 and 56 R3D3 elements, whereas the specimen plate is discretized with 84,960 C3D8R elements. A single woven ply of the specimen is approximated with two UD plies which results in total 32 UD plies representing 16 woven plies. Each UD ply is discretized with one finite element through thickness, resulting in 32 finite elements through thickness of the specimen. Furthermore, the impact area in the middle of the specimen is discretized with a finer mesh. Dimensions of this area are 50 x 57 mm, as shown in Figure 5.11. In [Cohades and Michaud, 2017b], coupons are subjected to three different impact energies: 8.5, 17 and 34 J impacts, which correspond to 1.5, 2.2 and 3 m/s impact velocities, respectively, as indicated in Figure 5.11. Thus, in Abaqus, these velocities are defined as a *Predefined Field* on the spherical impactor's reference point (RP) for each impact case. *General Contact* is defined in the model with *Normal Behaviour* and no friction. A total time of 6 ms was simulated in Abaqus/Explicit, i.e. as long as the impactor is in contact with the specimen, as indicated in force-displacements diagram in [Cohades and Michaud, 2017b]. Furthermore, experimental healing processes lasted 30 min at 150 °C. In Abaqus/Explicit analyses, total time of 0.1 ms was simulated to save the computational time. Thus, using an iterative procedure the healing model parameters are adjusted for the analysis to result in the same healing effect as experimental healing process. Moreover, these parameters are to be used only for analyses where duration of the healing period is scaled down from 30 min to 0.1 ms.

Constituents' mechanical properties and densities are given in Table 5.4. Matrix mate-

Table 5.5: Constitutive model parameters used in Abaqus analyses of healing after LVI.

MATRIX MATERIAL	
Damage model	
Γ^{vd}	$12.05\,\mathrm{s}^{-1}$
Y_{th}	11 MPa
k	1
q	1
Healing model	
Γ^{h}	$52,000\,\mathrm{s}^{-1}$
m_1	1
m_2	1
Plasticity model	
σ_{y0}	10 MPa
H	1,800 MPa

REINFORCING FIBRES	
Damage model	
$\delta_{eq}^{f,T}$	0.8
$\delta_{eq}^{f,C}$	0.8

rial's properties are taken from [Cohades and Michaud, 2017b]. General mechanical properties of E-glass UD fibres are taken from [László P. Kollár, George S. Springer, 2003]. Constitutive model parameters used in numerical analyses are given in Table 5.5.

5.3.1. Validation results and discussion

The developed constitutive model is validated by comparing the analysis results with: (i) experimentally obtained force-displacement diagram, (ii) C-scans of specimens and (iii) distribution of fibre damage in specimens.

Firstly, numerical and experimental contact forces are compared, Figure 5.12a. It is noticeable that for each impact scenario, 8.5, 17 and 34 J impact energy, an excellent agreement of experimental and analysis results is achieved. This implies that the damage model accurately predicts the damaging processes in the material. Furthermore, in Figure 5.12b, resulting contact forces obtained using the VUMAT self-healing composite material model are compared with resulting contact forces obtained using a linear elastic composite material model available in Abaqus. It can be observed that the linear elastic composite behaves significantly stiffer than the self-healing composite, since phenomena such as damaging and plasticity are not considered.

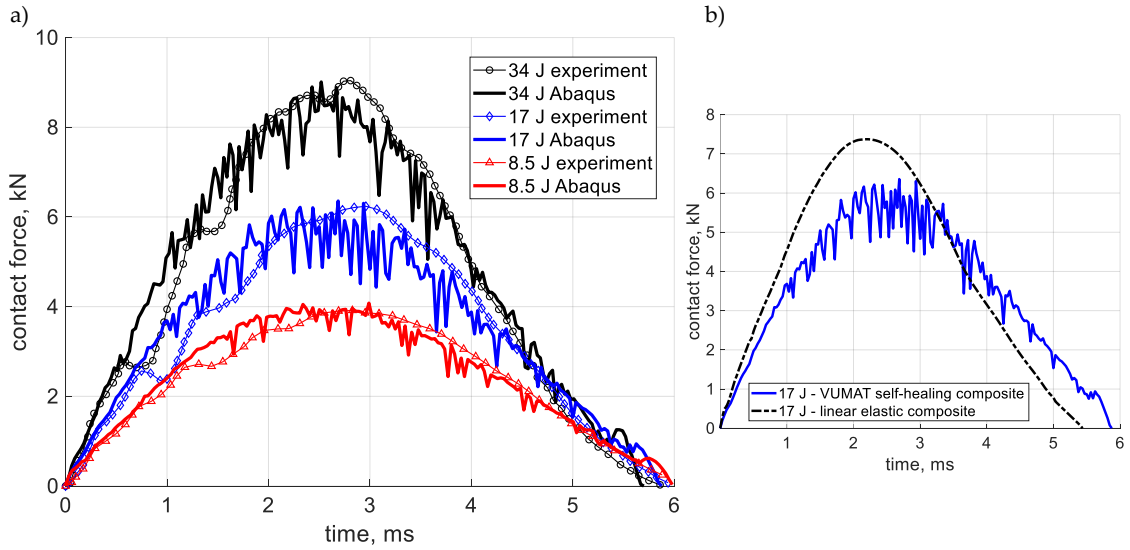

Figure 5.12: Contact forces during the LVI test; a) comparison of experimental and numerical contact forces for each low velocity impact case – 8.5, 17 and 34 J; b) comparison of contact forces obtained using VUMAT self-healing composite and a linear elastic composite for the 17 J impact case.

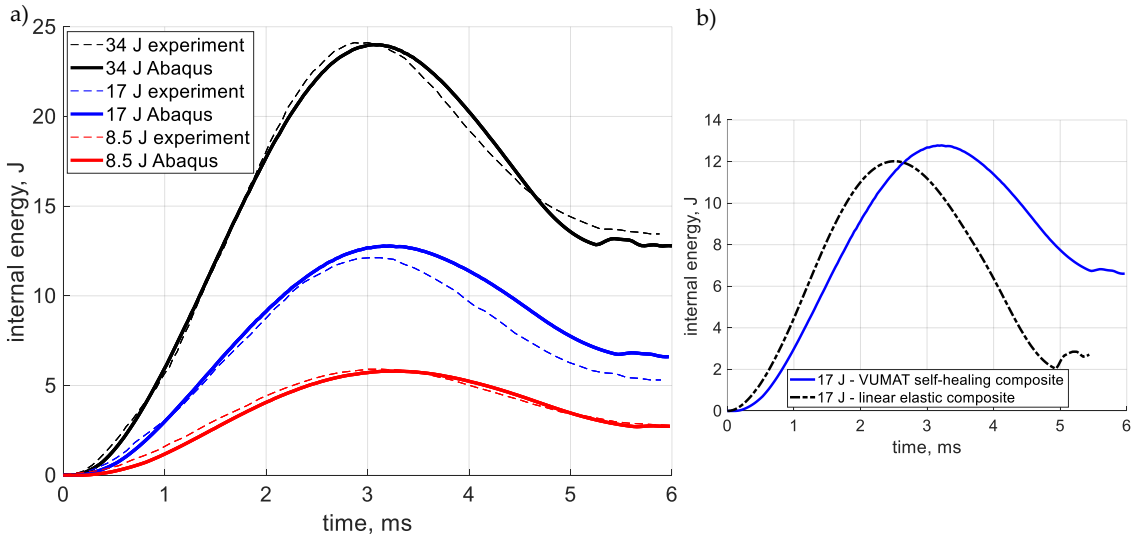

Figure 5.13: Internal energy during the LVI test; a) experimentally and numerically obtained internal energy accumulated in specimens for each low velocity impact case – 8.5, 17 and 34 J; b) internal energy obtained using VUMAT self-healing composite and using a linear elastic composite for the 17 J impact case.

Furthermore, numerically and experimentally obtained energies accumulated in specimens are compared. Results are given in Figure 5.13a. In Figure 5.13b, internal energy

obtained using the VUMAT self-healing composite material model is compared with internal energy obtained using the linear elastic composite material model, available in Abaqus. It can be observed that at the end of the experiment internal energy accumulated in linear elastic composite is significantly lower than the one in self-healing composite. The difference is caused by damage and plasticity models which are implemented in the VUMAT self-healing composite material model.

Ultrasonic C-scan is an image showing the distribution of damage through the thickness of the specimen. A drawback is that in these scans the distribution of damage in each ply is unknown. In [Cohades and Michaud, 2017b] such images are provided. Thus, in Figures 5.14 and 5.15 where analysis results i.e., effective damage distribution is compared with C-scans, only plies with maximum damaged area are shown. Analysis results show distribution of the effective damage variable in area of the specimen with finer mesh (50x57 mm), as indicated in Figure 5.11. Furthermore, in Figures 5.14 and 5.15 analysis results and experimental C-scans are given in the same scale – scale of the C-scan for 34 J impact. That is why original C-scans, taken from [Cohades and Michaud, 2017b], for the cases of 17 J and 8.5 J impact have white dashed frames to indicate the originally depicted healing region. The area outside the frame is added to the original C-scan to obtain an image comparable with analysis results. Furthermore, effective damage variable is shown in the interval [0.1,1]. Moreover, two plies are compared with a single C-scan since one woven ply is approximated with two UD plies.

Figure 5.14 shows comparison of numerical analysis results with C-scans before the healing process occurs, immediately after the impact, whereas Figure 5.15 is the same comparison after the healing process. In [Cohades and Michaud, 2017b] healing efficiency in terms of damage area recovery of 40 %, 55 % and 95 % is reported for impact cases 34, 17 and 8.5 J, respectively. Lower healing efficiency at higher energy impacts is attributed to fibre deformation and damage, as well as formation of large cracks. The developed constitutive model predicts constant healing efficiency of 25 % for each impact energy case with model parameters given in Table 5.5. In Figure 5.16 , distribution of the effective damage variable through the thickness of the specimen before and after the healing process is given. A 3/4 section view of the area with finer mesh (50 x 57 mm) is provided. Detailed views of the specimen are presented in the same scale. In this constitutive model, the matrix material healing model is independent on the fibre damage and the healing temperature, and the micro-damage model does not predict formation of large

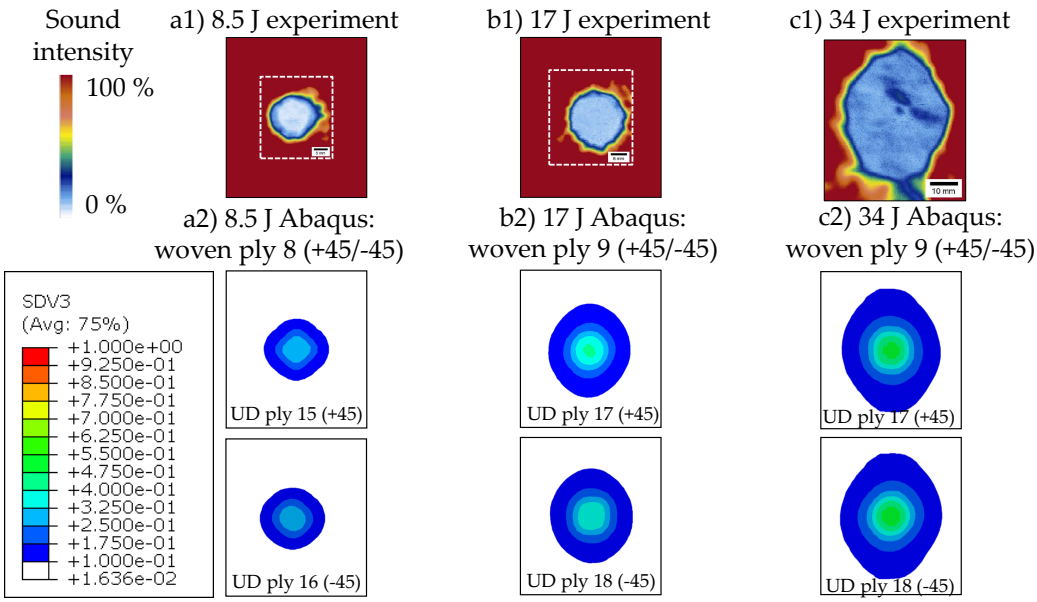

Figure 5.14: Comparison of effective damage variable ϕ_{eff} distribution with experimental C-scans before the healing process. One woven ply is represented with two UD plies. C-scans reprinted from [Cohades and Michaud, 2017b], with permission from Elsevier.

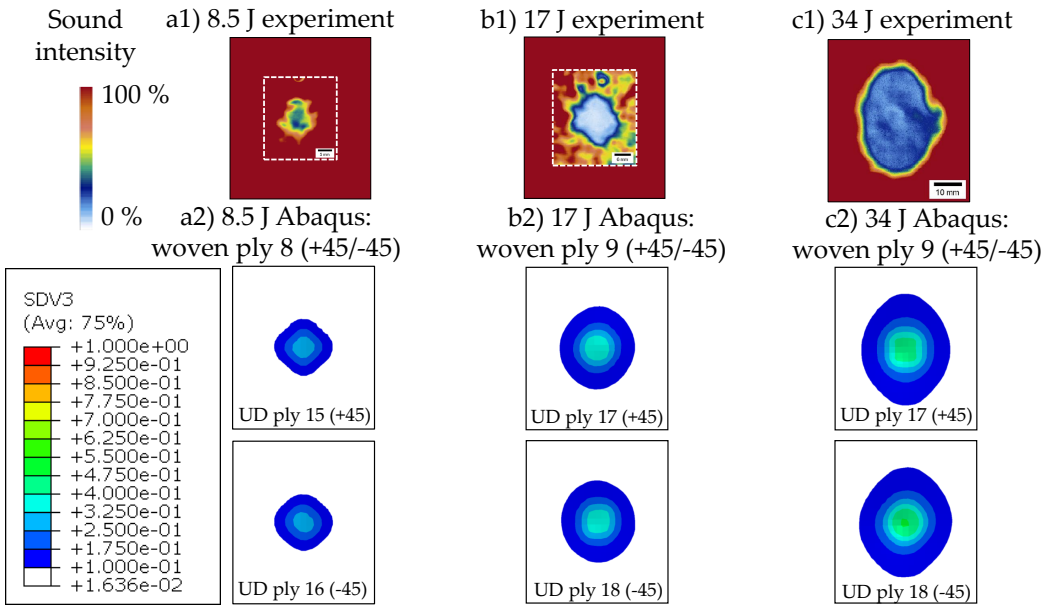

Figure 5.15: Comparison of effective damage variable ϕ_{eff} distribution with experimental C-scans after the healing process. One woven ply is represented with two UD plies. C-scans reprinted from [Cohades and Michaud, 2017b], with permission from Elsevier.

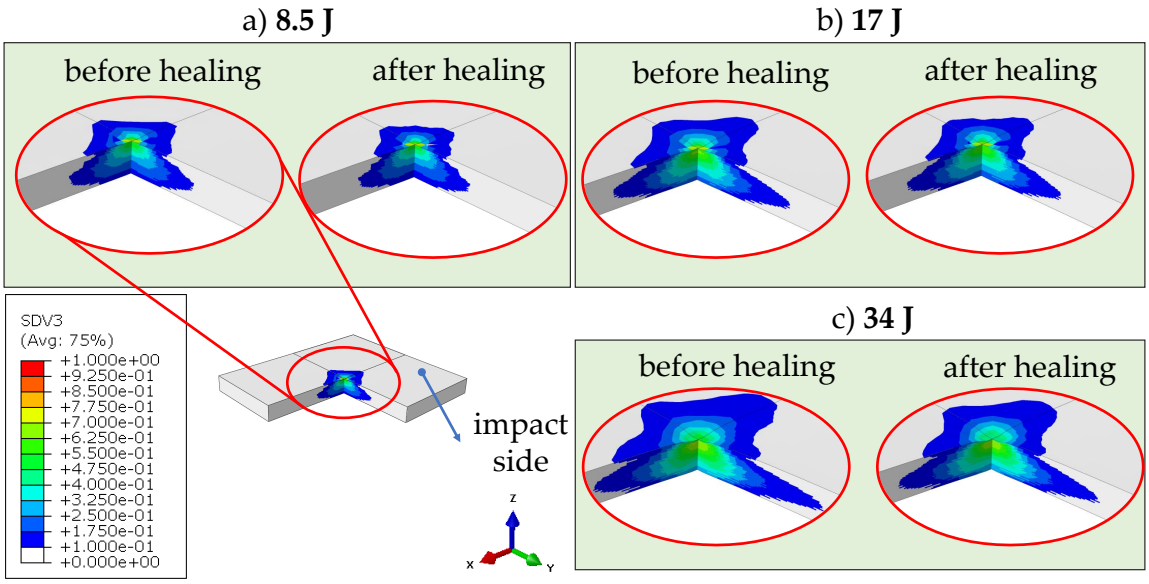

Figure 5.16: Distribution of the effective damage variable, ϕ_{eff}, in the impact area with finer mesh (50x57 mm), shown on a 3/4 section view of the specimen; a) 8.5 J impact case; b) 17 J impact case; c) 34 J impact case.

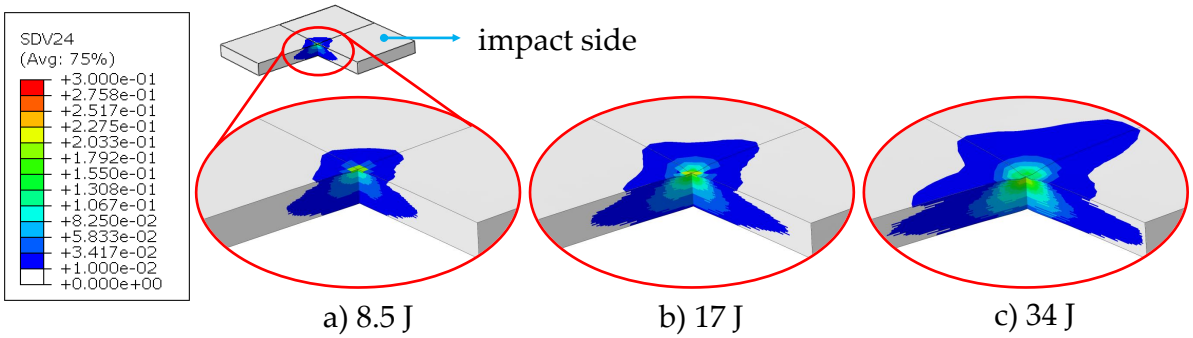

Figure 5.17: Through-thickness distribution of matrix effective plastic strain, p, in the impact area of the specimen (50 x 57 mm); a) 8.5 J impact case; b) 17 J impact case; c) 34 J impact case.

cracks. Furthermore, woven structure of the composite is approximated with UD plies. Thus, the difference between numerical analysis and experimental healing efficiencies is considered justified. However, despite the aforementioned differences, phenomenologically the model predicts that evolution of damage and its reduction during the healing process is consistent with experimental results. Figure 5.17 shows through-thickness distribution of the effective plastic strain of the matrix constituent at the end of the impact predicted in the analysis. Occurrence of fibre damage is predicted in the analysis and compared

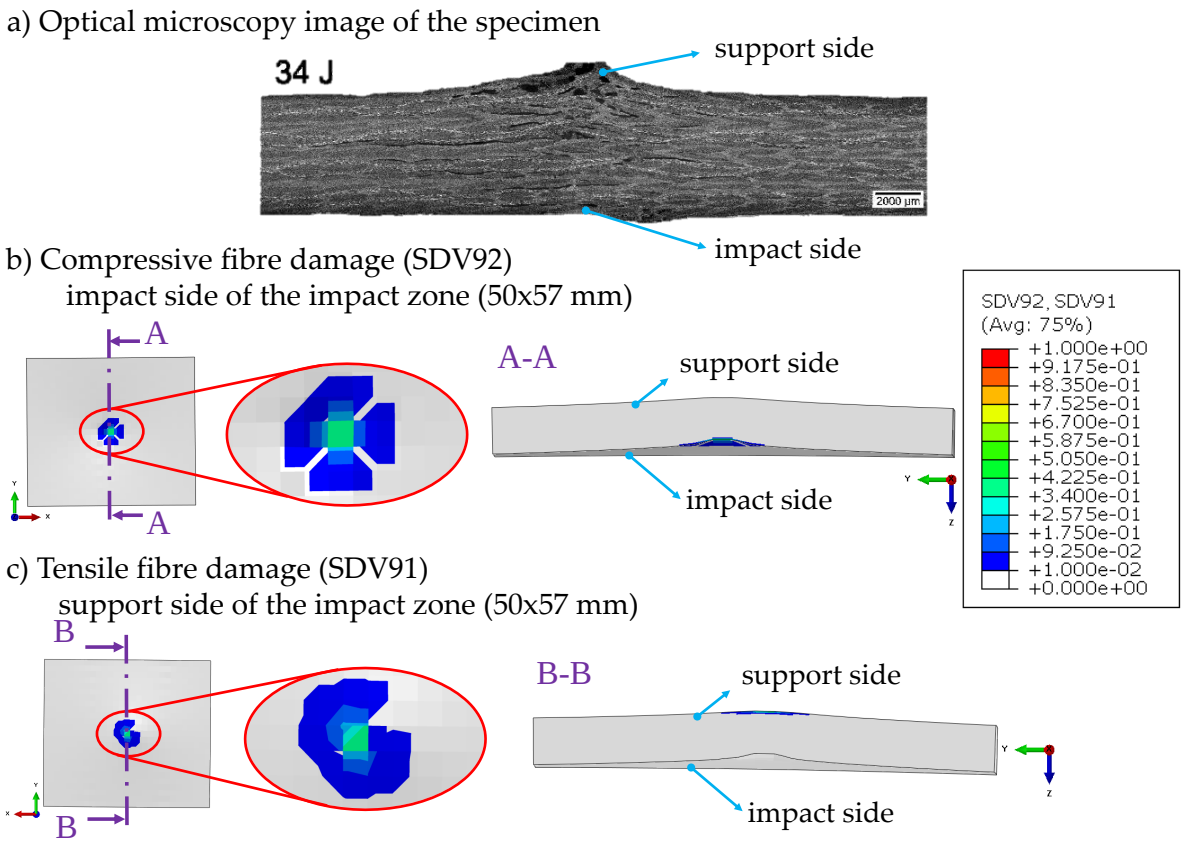

Figure 5.18: Prediction of fibre damage, ϕ_f, for the 34 J impact case; a) optical microscopy image of the specimen reprinted, with permission from Elsevier, from [Cohades and Michaud, 2017b]; b) distribution of compressive fibre damage in the specimen on the impact side and a cross-section view; c) distribution of tensile fibre damage in the specimen on the support side and a cross-section view.

with optical microscopy image of transversally cut impacted specimen, Figure 5.18. The developed constitutive model predicted occurrence of fibre damage in all three impact scenarios, whereas in [Cohades and Michaud, 2017b] fibre damage is documented only for the case of 34 J impact. However, at lower energy impacts, 8.5 J and 17 J, fibre failure has occurred in a single element (compressive fibre damage), whereas more significant fibre damage occurred for the case of 34 J impact. This is consistent with experimental results from [Cohades and Michaud, 2017b]. Slight disagreement with experiments for the cases of 8.5 J and 17 J impact is attributed to the approximation of woven structure with UD plies. Finally, in Figure 5.19 deformation of the specimen impact area (50 x 57 mm) for each impact case is given, a cross-section view. Figure 5.19a shows distribution of the effective plastic strain through the thickness of the specimen for each impact case

at the end of the impact. Figure 5.19b shows maximum magnitude of displacement of the specimen for each impact case.

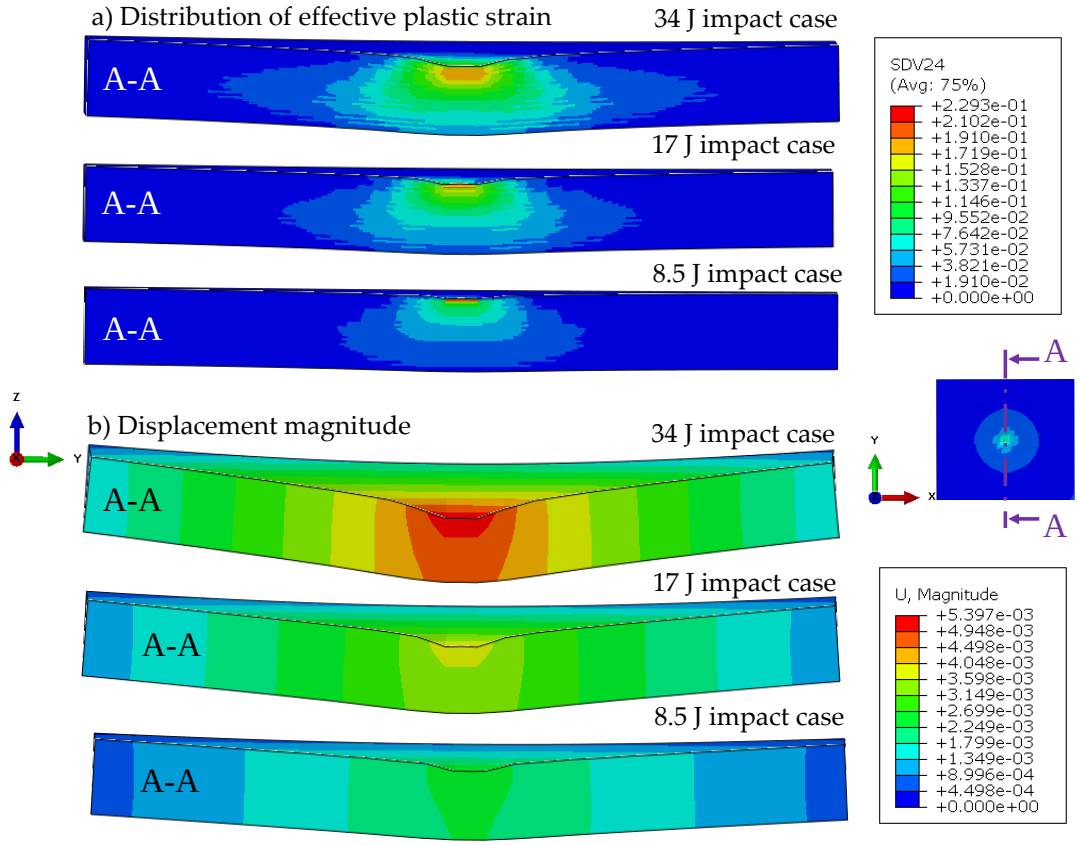

Figure 5.19: Deformation of the specimen for each impact case, A-A cross-section view; deformation scale factor = 1; a) distribution of effective plastic strain in the impact area of the specimen (50 x 57 mm) for each impact case; b) maximum magnitude of displacement [m] of the specimen in the impact area (50 x 57 mm) for each impact case

5.4. CFRP composite wing bird strike

In this section, the developed constitutive model is applied to modelling of bird strike damage and healing in a CFRP composite aircraft wing structure. Conducting of such an experiment was not feasible within this research. Furthermore, in the available literature, there are no experimental results of healing after high velocity impact in an aerospace structure. Thus, this analysis of a bird strike is a numerical experiment which relies on the constitutive model's fidelity and accuracy proved by successful validation for static

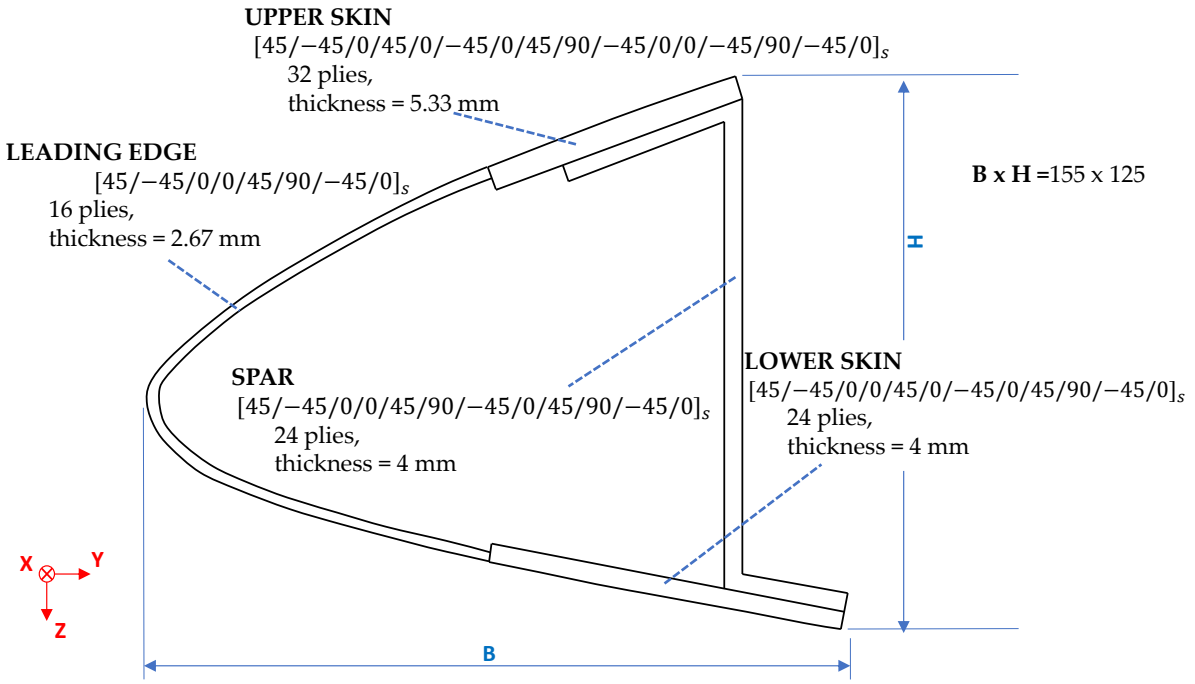

Figure 5.20: Schematic representation of the composite aircraft wing structure, a cross-section with layup sequences and thicknesses, and the main material coordinate system.

and dynamic loading cases. This numerical experiment aims to evaluate the healing efficiency after bird strike and application advantages of intrinsically self-healing FRP composites over conventional FRP composite materials in typical airframe structures. Simplified geometry of the wing structure is taken from [Long et al., 2021]. However, the wing structure in [Long et al., 2021] is not made of a self-healing polymer matrix, but a conventional epoxy matrix material. Thus, only geometry and the reinforcing fibres are taken as in [Long et al., 2021].

As previously mentioned, geometry of the aircraft wing structure is taken from [Long et al., 2021]. In Figure 5.20 a schematic side view of the wing structure with the main material coordinate system is given and layup sequences are denoted. Four characteristic regions with four different layups are designated with thickness of each ply equal to 0.167 mm:

1. leading edge, $[45/\text{-}45/0/0/45/90/\text{-}45/0]_s$,
2. upper skin, $[45/\text{-}45/0/45/0/\text{-}45/0/45/90/\text{-}45/0/0/\text{-}45/90/\text{-}45/0]_s$,
3. lower skin, $[45/\text{-}45/0/0/45/90/\text{-}45/0/45/90/\text{-}45/0]_s$ and
4. spar, $[45/\text{-}45/0/0/45/90/\text{-}45/0/45/90/\text{-}45/0]_s$.

Table 5.6: CFRP constituents' mechanical properties used in Abaqus analyses of healing after bird strike in a CFRP composite aircraft wing structure.

828EL + 25 vol% PCL		**T700 UD carbon fibre**	
E	1.58 GPa	E_{11}	230 GPa
ν	0.4	E_{22}	15 GPa
σ_{y0}	10 MPa	ν_{12}	0.2
ρ_{828EL}	1,340 kg/m^3	ν_{23}	0.4
ρ_{PCL}	1,145 kg/m^3	G_{12}	15 GPa
		G_{23}	7 GPa
		ρ_{T700}	1,800 kg/m^3
		X_f^T	4,900 MPa
		X_f^C	1,470 MPa
$\rho_{CFRP} = 1,535$kg/m^3			
Bird material			
c_0	1,480 m/s		
Γ_0	0		
s	0		
ρ_{bird}	1,010 kg/m^3		

The model of the wing structure is confined to the leading edge and wing skin including the spar to save on computational time. Moreover, this is the region where the effect of impact is expected to be the greatest. The material is a self-healing UD CFRP composite where a blend of Epon$^{\text{TM}}$828EL epoxy resin and 25vol% of poly(ε-caprolactone) (PCL) is used as the matrix constituent, and the T700 UD carbon fibres are used as reinforcements. The aforementioned self-healing polymer blend is opted, since this material has been used in validation of the constitutive model for the case of LVI in Section 5.3.. Fibre volume fraction is set to be $V_f = 48$ %, as in Section 5.3., since it has not been specified in [Long et al., 2021]. The bird is modelled using Smooth Particle Hydrodynamics (SPH) formulation, and with density of 1,010 kg/m^3 which results in bird mass of 0.171 kg. The SPH method is a meshless method, where only a collection of points is required to represent a body. Meshless approach is enabled using a fully Lagrangian modelling scheme which permits discretization of a prescribed set of continuum equations by interpolating the properties directly at a discrete set of points distributed over the solution domain. The SPH method is implemented via the formulation associated with PC3D elements in Abaqus. The material of the bird is defined using the equation of state material model in Abaqus. It is a linear $U_s - U_p$ Hugoniot form, with reference speed of sound, $c_0 = 1,480$

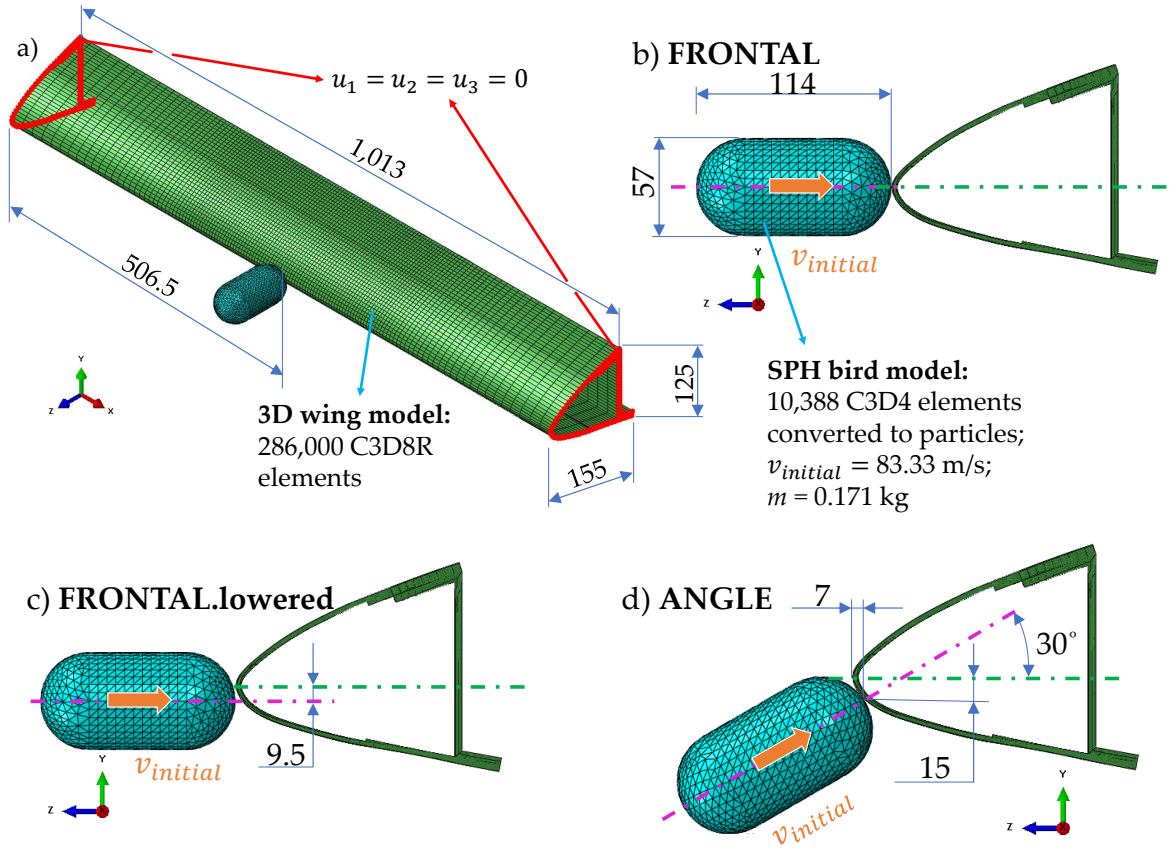

Figure 5.21: Abaqus model of the wing structure and SPH bird model with three different impact cases; dimensions in mm; a) Abaqus model of the impact setup with dimensions of the wing, boundary and initial conditions, and discretization details; b) frontal impact where imaginary axis of the wing profile and axis of symmetry of the bird model coincide (FRONTAL) and discretization details; c) frontal impact with distance between the axes is 9.5 mm (FRONTAL.lowered) and d) impact from below under the angle of 30 degrees (ANGLE).

m/s, Grüneisen ratio, $\Gamma_0 = 0$, and linear coefficient $s = 0$. Specified parameters of the linear $U_s - U_p$ Hugoniot form have provided physically sound results of contact force during bird impact in previously published references, [Smojver and Ivančević, 2010, Smojver and Ivančević, 2011, Smojver and Ivančević, 2012]. Initial velocity of the bird is set to 83.33 m/s (300 km/h) and analyses last 5 ms. Each healing period in analysis lasts 0.1 ms, which corresponds to 30 min of experimental healing time, as described in Section 5.3.. Since the utilised self-healing polymer matrix material is the same as the one in Section 5.3., the same healing model parameters are used. The reduction of healing process duration is a means for saving computational time. Accordingly,

the healing model parameters are artificially increased to match experimental healing periods. Mechanical properties of CFRP constituents and parameters of the linear $U_s - U_p$ Hugoniot form used in analyses are given in Table 5.6.

Several impact cases are investigated and a corresponding name is assigned to each case, which is represented in Figure 5.21:

- FRONTAL = frontal impact where the imaginary axis of the wing profile and the axis of symmetry of the bird model coincide,
- FRONTAL.lowered = frontal impact where distance between the wing profile and bird model axes is 9.5 mm in y-direction, and
- ANGLE = impact from below with angle of 30 degrees between the wing profile and bird model axes, in the yz plane.

In all three cases the bird impacts the wing in the middle with respect to its length. The model of the wing structure is discretized with 286,000 three-dimensional continuum C3D8R elements where each ply is represented with a single element. The bird is discretized with 10,388 C3D4 elements converted to particles, PC3D elements. Constitutive model parameters used in these analyses are given in Table 5.7.

Table 5.7: Constitutive model parameters used in Abaqus analyses of healing after bird strike in a CFRP composite aircraft wing structure.

MATRIX MATERIAL	
Damage model	
Γ^{vd}	$121.05\,\mathrm{s}^{-1}$
Y_{th}	11 MPa
k	1
q	1
Healing model	
Γ^{h}	$52,000\,\mathrm{s}^{-1}$
m_1	1
m_2	1
Plasticity model	
σ_{y0}	10 MPa
H	1,800 MPa

REINFORCING FIBRES	
Damage model	
$\delta_{eq}^{f,T}$	1.2
$\delta_{eq}^{f,C}$	1.2

5.4.1. Results and discussion

As previously mentioned, three impact cases with different initial configurations are simulated. Thus, in the remainder of this section results are shown in the form of comparison between each of the impact cases. In Figure 5.22 a time-lapse of impact analyses is given. Six time-frames, starting from 0.5 ms to the end of analyses, 5 ms, are shown. Based on these results, and as it was expected, the most severe deformation occurs for the case of ANGLE impact.

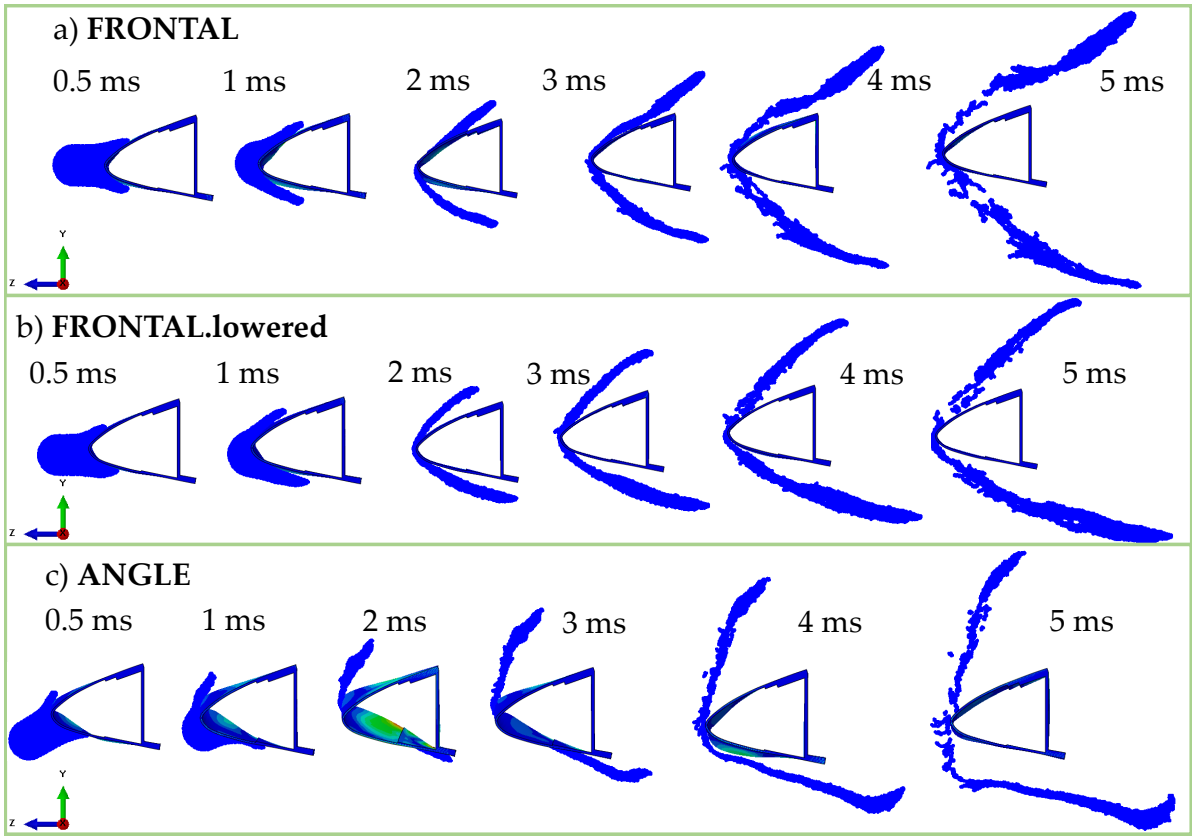

Figure 5.22: Time-lapse of the bird impact in a self-healing composite aircraft wing structure from 0.5 ms - 5 ms; deformation scale factor = 1; a) FRONTAL impact case; b) FRONTAL.lower impact case and c) ANGLE impact case.

Furthermore, Figures 5.23 and 5.24 represent distribution of the matrix effective damage variable in the composite aircraft wing structure, first outer ply (45°), front view. Figure 5.23 shows distribution of the effective damage variable prior to the healing process, whereas Figure 5.24 shows the state after the healing process. Identical healing model parameters, as defined in Table 5.7, are used for healing after all three impact

cases. As expected, the wing structure suffered the most severe damage for the case of ANGLE impact, and thus, the structure was not able to heal most of the damage that

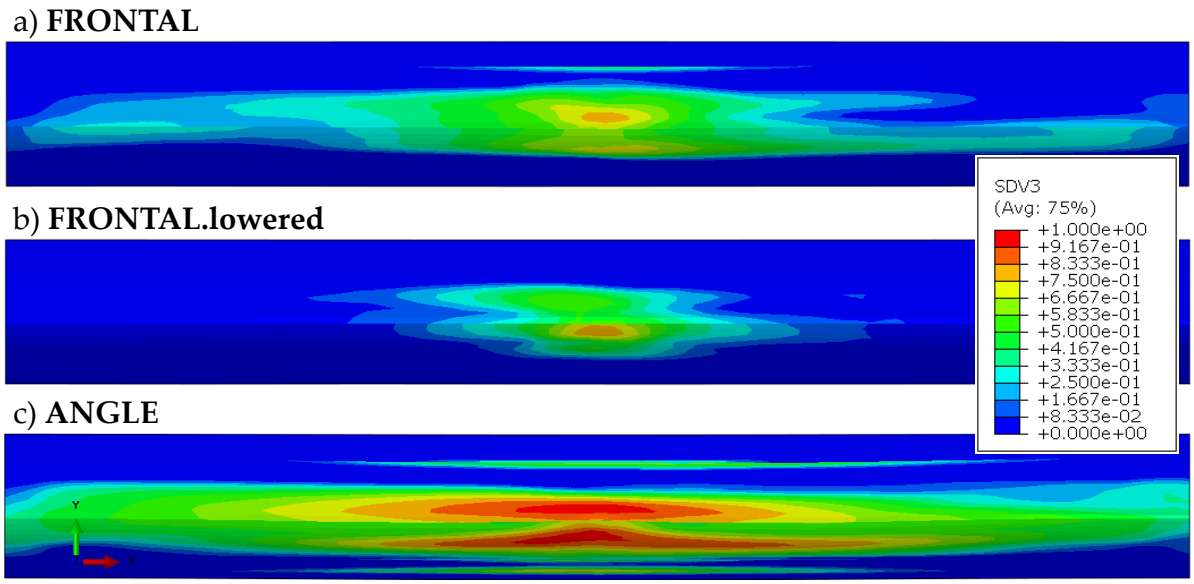

Figure 5.23: Distribution of the matrix effective damage variable, ϕ_{eff}, in the aircraft wing structure before the healing process; first outer ply, 45°; front view; a) FRONTAL impact case; b) FRONTAL.lowered impact case and c) ANGLE impact case.

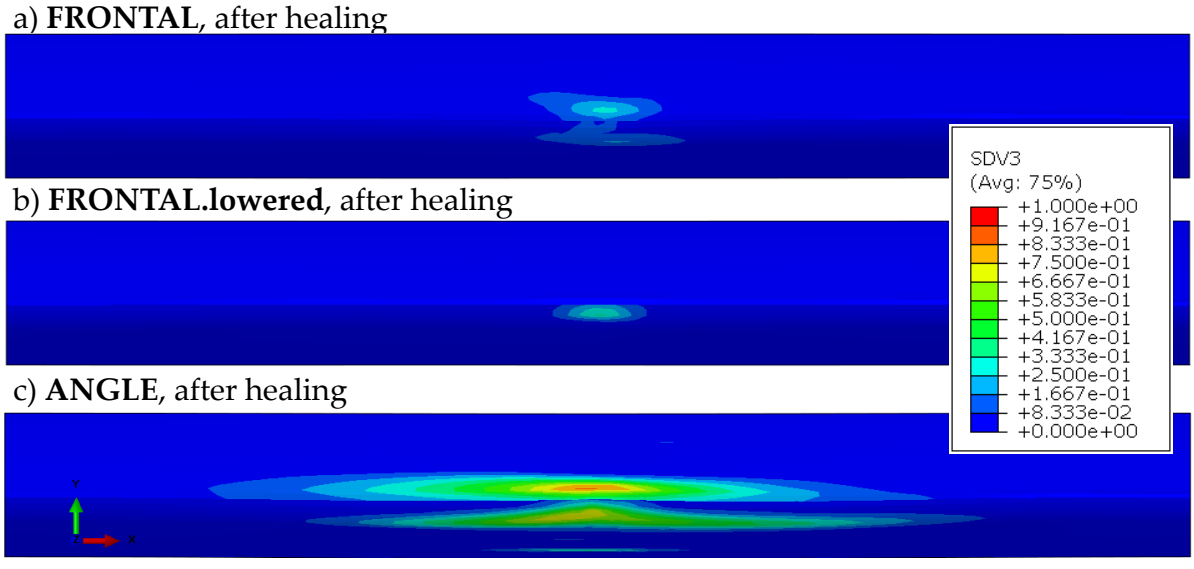

Figure 5.24: Distribution of the matrix effective damage variable, ϕ_{eff}, in the aircraft wing structure after the healing process; first outer ply, 45°; front view; a) FRONTAL impact case; b) FRONTAL.lowered impact case and c) ANGLE impact case.

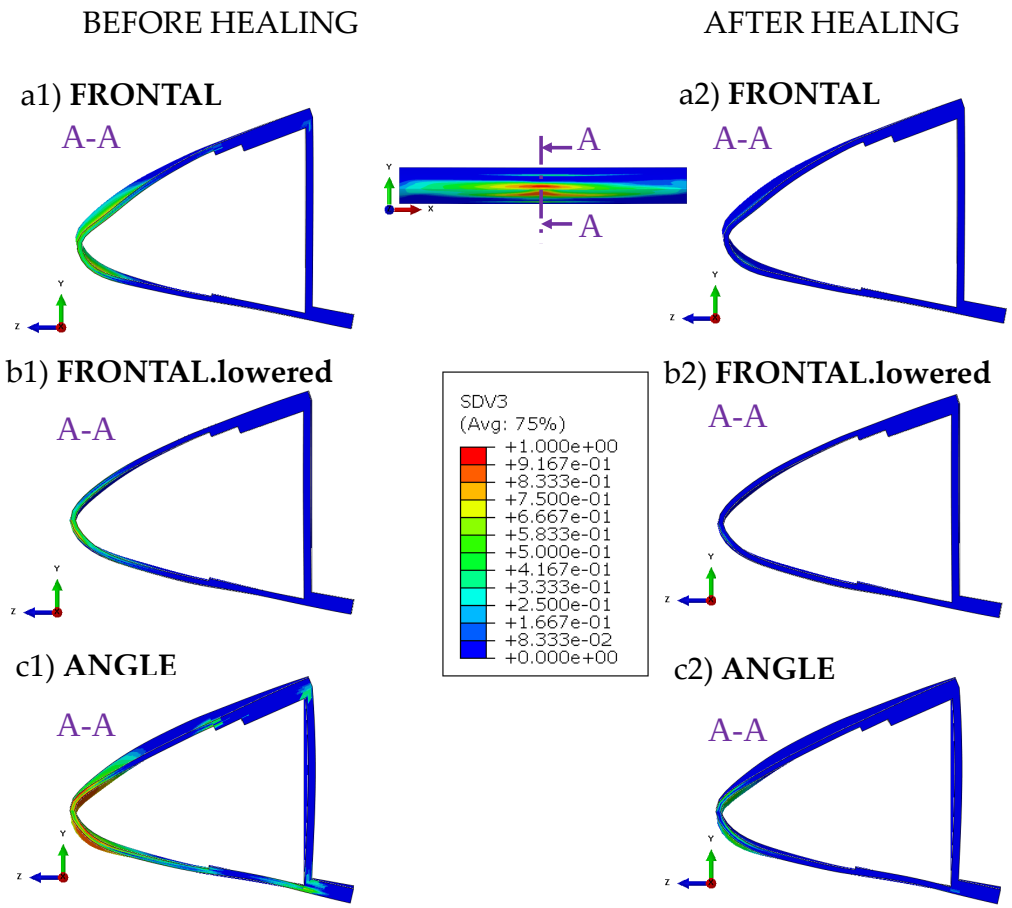

Figure 5.25: Distribution of the matrix effective damage variable, ϕ_{eff}, in the aircraft wing structure before and after the healing process, side cross-section view; a1) FRONTAL impact case before and a2) after the healing process; b1) FRONTAL.lowered impact case before and b2) after the healing process; c1) ANGLE impact case before and c2) after the healing process.

occurred during the impact. On the other hand, in cases of FRONTAL.lowered and FRONTAL impact case the structure healed almost completely. This can also be observed in Figure 5.25, where distribution of the effective damage variable is shown in a cross section of the wing structure. Furthermore, it can be seen that in the case of ANGLE impact, matrix damage is not constrained to the tip of the leading edge. It also occurs in regions of geometry discontinuation, where laminate thickness changes. This is physically sound, since geometry discontinuations cause stress concentration. After the healing process, the matrix damage in these regions is almost completely healed. Except in the case of ANGLE impact - in the joint of spar and lower skin, there is still considerable

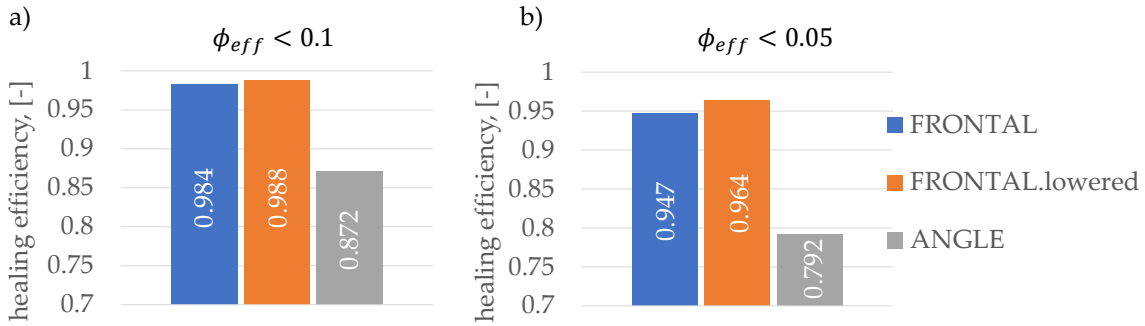

Figure 5.26: Healing efficiencies calculated by means of Eq. 1.1 and using the number of finite elements with values of matrix effective damage variable, ϕ_{eff}, within specified interval; a) efficiencies calculated considering elements with $\phi_{eff} < 0.1$ and for each impact case; b) efficiencies calculated considering elements with $\phi_{eff} < 0.05$ and for each impact case.

matrix damage. This is due to the fact that in this region, fibre rupture occurred and as a result, multiple elements were deleted in the analysis, which caused increased stress intensity. Healing efficiencies are quantified and represented using bar charts in Figure 5.26. Calculation is performed using the adjusted form of equation 1.1

$$\eta = \frac{N_{el}^{healed} - N_{el}^{damaged}}{N_{el}^{total} - f_{el}^{damaged}}, \tag{5.30}$$

where

N_{el}^{healed} is the number of finite elements with values of matrix effective damage variable, ϕ_{eff}, within specified interval, after the healing process;

$N_{el}^{damaged}$ is the number of finite elements with values of matrix effective damage variable, ϕ_{eff}, within specified interval, before the healing process and

N_{el}^{total} is the total number of finite elements in the model.

Specifically, in the first case, the interval for ϕ_{eff} is $\phi_{eff} < 0.1$, whereas in the second case the interval is $\phi_{eff} < 0.05$. The total number of finite elements in the wing structure model is 286,000, as defined in Figure 5.21. Finite elements with values of matrix effective damage variable within the specified interval are displayed using the *Create Display Group*, *Item: Elements*, *Method: Result Value*, option in Abaqus. Elements in the display group are counted using the *XY Data from ODB Field Output* and *Pick from viewport* option. The results are in good agreement with visual distribution of the effective damage variable, given in Figures 5.23, 5.24 and 5.25. Lowering the limit value of ϕ_{eff} means that more rigorous healing is requested and thus, the healing efficiencies

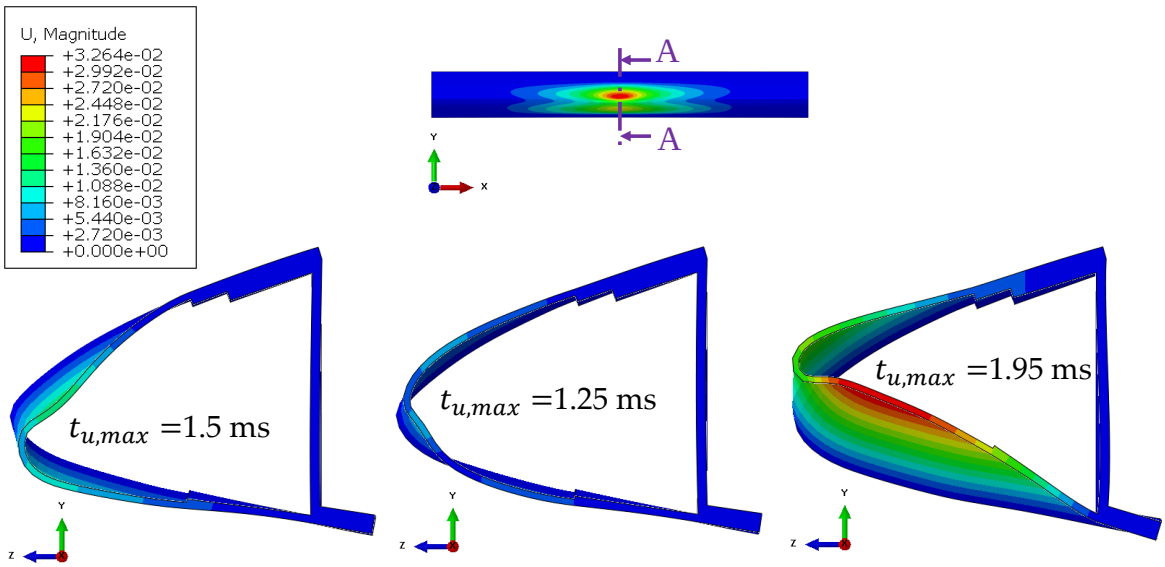

Figure 5.27: Displacements of the wing structure during the impact, deformation scale factor = 1; displacements in m; for each impact case, the time-frame with maximum displacement is shown, $t_{u,max}$; a)FRONTAL impact case, $t_{u,max}$ = 1.5 ms; b)FRONTAL.lowered impact case, $t_{u,max}$ = 1.25 ms; c)ANGLE impact case, $t_{u,max}$ = 1.95 ms.

decrease. The lowest healing efficiency is achieved for the case of ANGLE impact, since the structure suffered severe damage. Additionally, failed (deleted) elements, which had fibre rupture, contribute to decreasing the healing efficiency. For cases of FRONTAL and FRONTAL.lowered impact, healing efficiencies are similar both when $\phi_{eff} < 0.1$ and $\phi_{eff} < 0.05$ which indicates that in these cases structure suffered similar levels of matrix damage.

Comparison of maximum displacements of the aircraft wing structure for each impact case is depicted in Figure 5.27. Cross-section view of the wing structure, as designated in Figure 5.27, with deformation scale factor = 1 is given. Maximum displacement for the FRONTAL impact case is reached after 1.5 ms, Figure 5.27a, for the FRONTAL.lowered impact case after 1.25 ms, Figure 5.27b, and for the ANGLE impact case maximum displacement is reached after 1.95 ms.

Figure 5.28 represents distribution of the matrix effective plastic strain in the aircraft wing structure for each of the impact cases, front view, first outer ply, 45°. Moreover, a cross-section view for each impact case is provided giving an insight into through-thickness

distribution of the effective plastic strain.

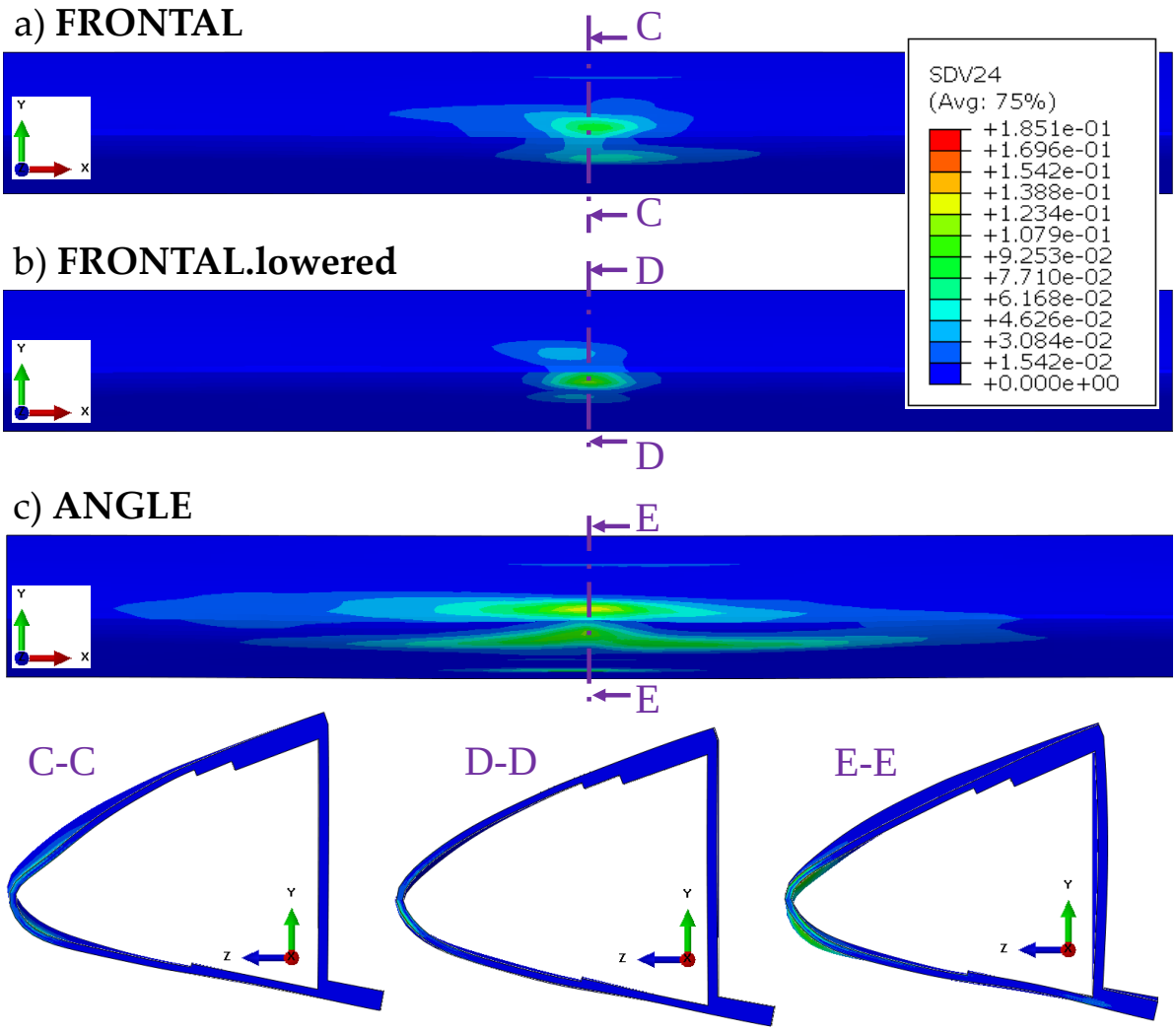

Figure 5.28: Distribution of the matrix effective plastic strain in the aircraft wing structure after the bird strike; first outer ply, 45°; a) FRONTAL impact case, front and side cross-section view; b) FRONTAL.lowered impact case, front and side cross-section view; and c) ANGLE impact case, front and side cross-section view.

Interesting observations can be made by analysing distribution of fibre damage in the aircraft wing structure after the impact. Firstly, tensile fibre damage is not present in the model, which is not the case for compressive fibre damage. In the first two plies, counting from the impact surface, fibre damage is not present in any of the impact cases. Distribution of compressive fibre damage in specific plies of the composite aircraft structure can be observed in Figure 5.29. In the FRONTAL impact case, compressive fibre

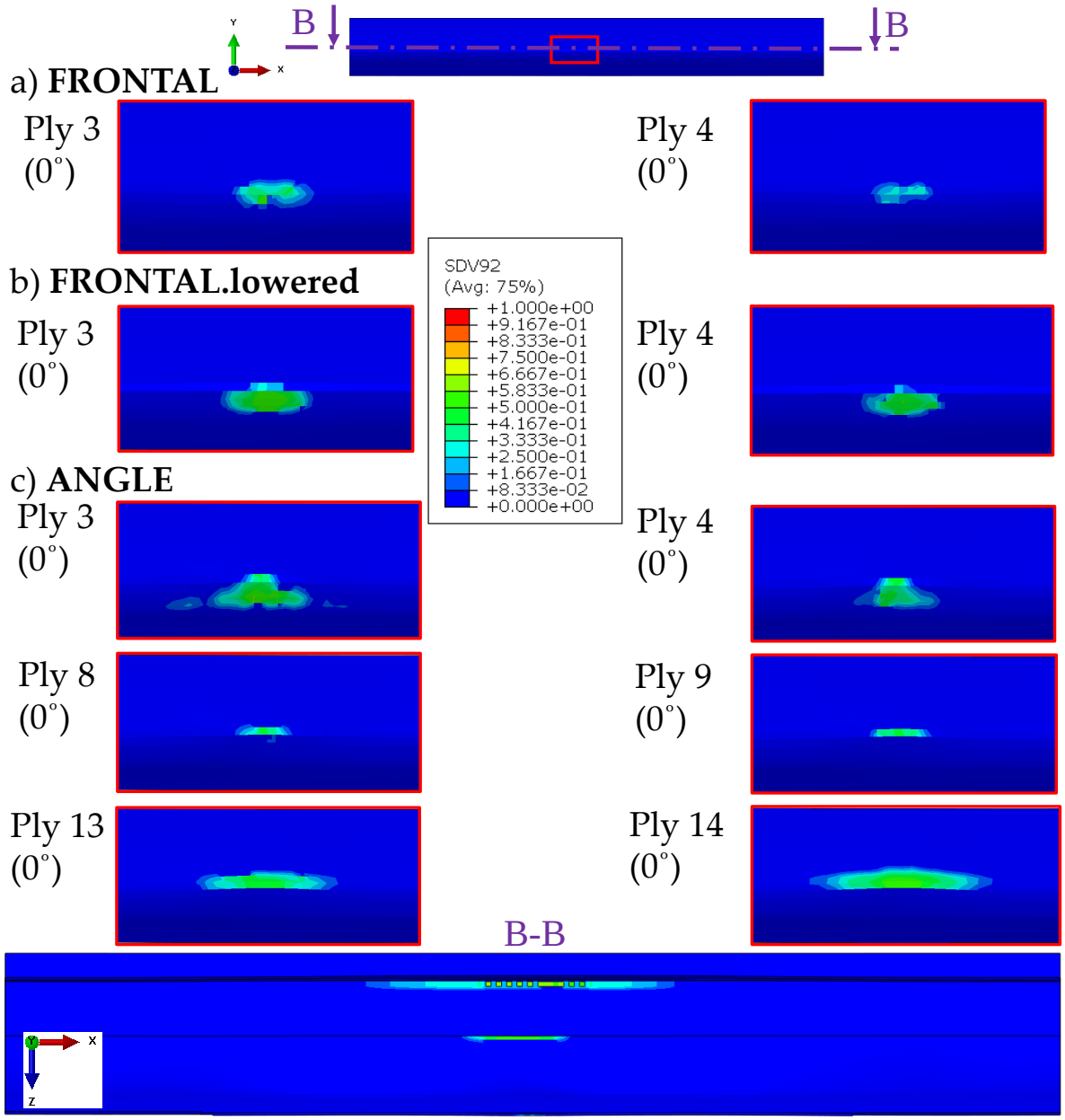

Figure 5.29: Distribution of compressive fibre damage variable in the aircraft wing structure after the bird strike; a) FRONTAL impact case, plies 3 and 4, detailed front view; b) FRONTAL.lowered impact case, plies 3 and 4, detailed front view and c) ANGLE impact case, plies 3, 4, 8, 9, 13 and 14, detailed front view, and longitudinal section view showing presence of fibre damage in regions where laminate thickness changes; rupture, deletion of elements present in the joint of lower skin and spar.

damage occurred in plies 3 and 4, counted from the impact surface, Figure 5.29a. The same situation is with the FRONTAL.lowered impact case, Figure 5.29b. As expected, in the case of ANGLE impact, compressive fibre damage occurred in plies 3, 4, 8, 9, 13 and 14, Figure 5.29c. All these plies are of the same orientation, 0-degree. In case of FRONTAL and FRONTAL.lowered impact cases, only the two 0-degree plies closest to the impact surface suffered fibre damage. Moreover, in case of critical ANGLE impact scenario, all 0-degree plies through the thickness of the laminate have suffered fibre damage. Thus, it can be concluded that 0-degree orientation plies are the most vulnerable to impact damage. Furthermore, section B-B shows regions with the aforementioned geometry discontinuations where compressive fibre damage is present. These regions are: (1) joint of the leading edge and lower skin, and (2) joint of the lower skin and the spar. In addition, the latter joint suffered fibre rupture which is, in analysis, physically represented as element deletion.

6 Conclusion

In Chapter 4. a CDHM based constitutive model for a self-healing composite matrix material is proposed. The model resulted from combining the damage variable evolution equation from [Darabi et al., 2011], healing variable evolution equation from [Abu Al-Rub et al., 2010] and the von Mises linear isotropic hardening plasticity model. Introduction of the healing configuration from [Abu Al-Rub et al., 2010] and application of the strain equivalence hypothesis streamlined numerical implementation of the developed model. The proposed constitutive model proved its applicability to describing the behaviour of a self-healing composite matrix polymer material by successful validation using static tensile and cyclic tensile loading tests. The aforementioned experiments were conducted on pure Surlyn® 8940 coupons. A detailed outline and parameters of these experimental procedures, necessary for validation of the model, are given in this Chapter. Successful coupling of the damage-healing model with the plasticity model resulted in non-linear behaviour of the effective plastic strain. Furthermore, the von Mises linear isotropic hardening plasticity model enables accurate prediction of plastic strain after successful coupling with damage and healing models. The aforementioned very good agreement with experimental results justifies the usage of this model. Finally, the model can simulate the healing phenomenon of the Surlyn® 8940 which causes the stiffness recovery between the two cycles.

In Chapter 5. micromechanical constitutive model of intrinsically self-healing UD CFRP composite is presented and successfully validated for static and dynamic loading cases. At the microscale, plastic behaviour, micro-damaging and healing mechanisms of the isotropic matrix material are described using the constitutive model presented

and validated in Chapter 4.. On the other hand, the reinforcing fibres are modelled as transversely isotropic linear elastic material with maximum stress failure criterion and applying progressive damage model from [Lapczyk and Hurtado, 2007]. Homogenised mechanical properties of the composite are calculated using the ROM expressions. Localisation is performed using the Voigt iso-strain and Reuss iso-stress assumptions.

Firstly, the developed constitutive model is validated for static loading cases using experimental results of three point flexural tests from [Park et al., 2010]. It is shown that the model can accurately describe the micro-damaging mechanism in bis-maleimide tetrafuran (2MEP4F) UD CFRP composite. Moreover, the healing phenomenon, i.e. the regain of flexural stiffness during the healing process can be accurately predicted using the developed constitutive model.

Secondly, the model is validated for the case of dynamic loading. The proposed multi-scale framework for intrinsically self-healing UD FRP composites is applied to modelling of intrinsically self-healing woven GFRP (Glass Fibre Reinforced Polymer) composites by approximating a single woven ply with two UD plies. The model's application to woven intrinsically self-healing GFRP composites is successfully validated using the experimental results of low velocity impact tests from [Cohades and Michaud, 2017b]. An excellent agreement of experimental and analyses results is achieved when comparing contact forces. This implies that coupling of the applied matrix and fibre damage models accurately predicts the damaging mechanisms in specimens. Furthermore, C-scans and plies with maximum damaged area are compared. Here it is concluded that the developed model phenomenologically predicts evolution of matrix micro-damage and its reduction consistent with experimental ultrasonic measurements. Moreover, fibre damage model used in this work precisely simulated occurrence of fibre damage in the 34 J impacted specimen. Based on the results, it is concluded that the developed model's application to simulation of woven FRP composites during low velocity impact and post-impact healing is successfully validated. Finally, it is considered that with introduction of certain valid approximations and with setting proper values of model parameters, the developed numerical methodology can be used to accurately predict micro-damaging and healing of FRP composites.

Experiments used in this Thesis:

1. static tensile tests - self-healing polymer,

2. cyclic tensile tests - self-healing polymer,

3. three point bending tests - self-healing composite and

4. low velocity impact tests - self-healing composite,

form a set of experimental procedures for validation of a constitutive model for intrinsically self-healing FRP composites. Thereby, firstly a constitutive model for the polymer matrix material is validated using experiments 1) and 2). Afterwards, the constitutive model of a self-healing composite is validated using experiment 3) for static loading cases and experiment 4) for dynamic loading cases.

Finally, after successful validation for both static and dynamic loading conditions, the developed constitutive model is applied to simulate damaging of composite aircraft wing structure during the bird strike event, and post-impact healing. Three different initial configurations are analysed: FRONTAL, FRONTAL.lowered and ANGLE, as represented in Figure 5.21. Analyses predicted physically sound displacements and extent of damage, and in agreement with expectations - ANGLE impact case, where the bird impacts the wing from beneath it and under an angle of 30 degrees, is the critical impact case for mechanical integrity of the structure. Furthermore, results have shown that 0-degree plies are the most vulnerable to impact damage, since they suffered serious compressive fibre damage. In case of FRONTAL and FRONTAL.lowered impact cases, fibre damage and severe matrix damage occur in the leading edge. However, in case of ANGLE impact, regions with changes in laminate thickness also suffered fibre and matrix damage. Critical are 0-degree plies in vicinity of a joint of a spar with a lower skin, which suffered fibre rupture. Thus, layup sequence should be carefully examined when designing composite aerospace structures subject to impact loading conditions. Finally, matrix damage is successfully mended during the healing process, which proves that intrinsically self-healing composite structures could successfully tackle matrix damage induced during a HVI impact. In this way, service lifetime of such structures could be prolonged since propagation rate of delamination and matrix micro-cracks would be reduced.

Prospective applications of self-healing materials in aircraft composite structures are numerous, since damage phenomena such as delamination, matrix failure or BVID (Barely Visible Impact Damage) could be successfully dealt with. The successful future development of self-healing composites applications could significantly increase the safety

of aerospace structures, as well as revolutionize the principles and approaches in their maintenance. Furthermore, matrix damage recovery using self-healing structures would finally result in more sustainable composite aerospace structures, since their exploitation period would be prolonged. A reliable and accurate constitutive model for such materials will play a significant role in this, since it will enable extensive testing of aerospace structures without the need for a wide range of experimental tests.

6.1. Original scientific contribution

1. Development of a new constitutive model for modelling of damage and healing phenomena in fibre reinforced polymer composite structures where the matrix constituent exhibits intrinsic self-healing ability. The evolution of the damage variable depends on strain rate and level, and accumulated damage, whereas the healing variable evolution depends on time during which healing process takes place. Furthermore, numerical simulation of damage at previously healed portions of material is enabled.
2. Validation of developed constitutive model for a pure self-healing polymer, static tensile and cyclic tensile loading.
3. Validation of developed constitutive model for a self-healing FRP composite in static loading conditions - a three point bending test.
4. Validation of developed constitutive model for a self-healing FRP composite in dynamic loading conditions - a low velocity impact test.
5. Experimental procedures for validation of developed constitutive model.
6. Simulation of a bird strike and post-impact healing of a self-healing composite aircraft wing structure. Evaluation of healing efficiency and assessment of application advantages of self-healing FRP composite structures over conventional ones.

6.2. Recommendation for further research

Proposed methodology proved to be accurate in describing damaging and healing phenomena in intrinsically self-healing polymers and FRP composites. The model implements plasticity and rate-dependant damage and healing models. Furthermore, in this Thesis uncoupled healing is assumed, i.e. healing and damage processes do not

occur simultaneously. As mentioned in the introductory part of this Thesis, many other factors influence the damaging and healing phenomena in self-healing polymers and FRP composites. The healing process is greatly affected by temperature and pressure. Further improvement of the model would include these two factors. Extensive experimental research is necessary for the aforementioned improvement of the model, to quantitatively determine the influence of temperature and pressure for a specific intrinsically self-healing polymer. Furthermore, the hypothesis of uncoupled healing has to be tested in situ, which again requires extensive experimental testing. It is concluded that detailed modelling of the healing phenomenon of a specific material requires extensive experimental testing. Newly defined experiments would be added to the procedure defined in the previous section, thus making it an even more comprehensive experimental procedure for validation of the constitutive model for intrinsically self-healing FRP composites. Moreover, implementation of a different micromechanical model is recommended to evaluate the obtained results.

Additionally, during the making of this dissertation, results of extensive experimental research on a new class of polymers - vitrimers, have been published in the literature. These results encompass their processability, formability, bonding capability and repairability. Vitrimers are epoxy networks that can rearrange their topology by exchange reactions without depolymerization. However, at this point, thermo-mechanical, elasto-plastic, damage and healing properties have not been sufficiently investigated to enable numerical modelling of their behaviour using the developed constitutive model. Since vitrimers exhibit properties such as elasticity modulus and glass transition temperature close to the ones of epoxy-based systems, they present a prospective alternative to epoxy resins in FRP composites. Furthermore, their exceptional reprocessability, healing properties and bonding capability make them superior to conventional matrix systems. Thus, numerical modelling of damage-healing behaviour of vitrimers presents another application niche for the developed constitutive model.

Finally, the ultimate extension of the proposed methodology would be simulation of puncture sealing and subsequent healing. Sealing here refers to closure of the puncture which occurred due to the high velocity impact, whereas the healing means restoration of the elasticity modulus. This is especially interesting for modelling of high velocity and space debris impact protection.

To sum up, this Thesis laid foundations for further research on numerical modelling

of intrinsically self-healing FRP composites, which is a vast research field. Moreover, applications of such materials are numerous, one of which is the aircraft wing structure, analysed in this Thesis. Number of future applications of such materials implies the opportunities and needs for improvement of the developed methodology.

Biography

Personal data:	Dominik Brezetić was born on May 6, 1994 in Karlovac, where he attended primary school. He graduated from Karlovac High School, a math-intensive programme. In 2013, he enrolled in the Study of Mechanical Engineering at the Faculty of Mechanical Engineering and Naval Architecture (FMENA), University of Zagreb. He is a proficient user of English and German, and a basic user of French.
Education:	
2019-2023	PhD student at the Faculty of Mechanical Engineering and Naval Architecture, University of Zagreb
2019	Master's Degree in Mechanical Engineering
2013-2019	Undergraduate and graduate studies in Mechanical Engineering at the Faculty of Mechanical Engineering and Naval Architecture, University of Zagreb
Employment:	
since 2019	Research assistant at the Department of Aeronautical Engineering, Faculty of Mechanical Engineering and Naval Architecture, University of Zagreb
Awards:	
2017	Medal of FMENA for achievement during studies
2017	"Končar - električna vozila" award
2016	"Davorin Bazjanac" award
List of publications:	www.bib.irb.hr/profile/35605

Životopis

Osobni podaci:	Dominik Brezetić je rođen 6. svibnja 1994. godine u Karlovcu gdje je pohađao i osnovnu školu. Srednjoškolsko obrazovanje je stekao u Gimnaziji Karlovac, prirodoslovno-matematički smjer. Studij strojarstva na Fakultetu strojarstva i brodogradnje Sveučilišta u Zagrebu upisao je 2013. godine. Aktivno se služi engleskim i njemačkim jezikom, a osnovni je korisnik i francuskog jezika.
Obrazovanje:	
2019. - 2023.	Student na poslijediplomskom doktorskom studiju Fakulteta strojarstva i brodogradnje, Sveučilišta u Zagrebu.
2019.	Magistar inženjer strojarstva.
2013. - 2019.	Preddiplomski i diplomski studij strojarstva na Fakultetu strojarstva i brodogradnje, Sveučilišta u Zagrebu.
Zaposlenja:	
2019. -	Istraživač na projektu HRZZ-a na Zavodu za zrakoplovstvo, Fakulteta strojarstva i brodogradnje, Sveučilišta u Zagrebu.
Nagrade:	
2017	Medalja Fakulteta strojarstva i brodogradnje Sveučilišta u Zagrebu za uspjeh tijekom preddiplomskog studija.
2017	Nagrada "Končar - električna vozila" za uzoran uspjeh na četvrtoj godini preddiplomskog studija
2016	Nagrada "Davorin Bazjanac" za uzoran uspjeh na trećoj godini preddiplomskog studija
Popis publikacija:	www.bib.irb.hr/profile/35605

Bibliography

[Abu Al-Rub and Darabi, 2012] Abu Al-Rub, R. K. and Darabi, M. K. (2012). A thermodynamic framework for constitutive modeling of time- and rate-dependent materials. part i: Theory. *International Journal of Plasticity*, 34:61–92.

[Abu Al-Rub et al., 2010] Abu Al-Rub, R. K., Darabi, M. K., Little, D. N., and Masad, E. A. (2010). A micro-damage healing model that improves prediction of fatigue life in asphalt mixes. *International Journal of Engineering Science*, 48(11):966–990.

[Alsheghri and Abu Al-Rub, 2015] Alsheghri, A. A. and Abu Al-Rub, R. K. (2015). Thermodynamic-based cohesive zone healing model for self-healing materials. *Mechanics Research Communications*, 70:102–113.

[An et al., 2021] An, S., Yoon, S. S., and Lee, M. W. (2021). Self-healing structural materials. *Polymers*, 13(14).

[Azevedo do Nascimento et al., 2020] Azevedo do Nascimento, A., Fernandez, F., S. da Silva, F., P.C. Ferreira, E., D. Melo, J. D., and Cysne Barbosa, A. P. (2020). Addition of poly (ethylene-co-methacrylic acid) (emaa) as self-healing agent to carbon-epoxy composites. *Composites Part A: Applied Science and Manufacturing*, 137:106016.

[Barbero and Ford, 2007] Barbero, E. J. and Ford, K. J. (2007). Characterization of self-healing fiber-reinforced polymer-matrix composite with distributed damage. *Journal of Advanced Materials*, 39(4):20–27.

[Barbero et al., 2005] Barbero, E. J., Greco, F., and Lonetti, P. (2005). Continuum damage-healing mechanics with application to self-healing composites. *International Journal of Damage Mechanics*, 14(1):51–81.

[Batra et al., 2012] Batra, R. C., Gopinath, G., and Zheng, J. Q. (2012). Material parameters for pressure-dependent yielding of unidirectional fiber-reinforced polymeric composites. *Composites Part B: Engineering*, 43(6):2594–2604.

[Bierwagen and Tallman, 2001] Bierwagen, G. and Tallman, D. (2001). Choice and measurement of crucial aircraft coatings system properties. *Progress in Organic Coatings*, 41(4):201–216.

[Blaiszik et al., 2010] Blaiszik, B. J., Kramer, S., Olugebefola, S. C., Moore, J. S., Sottos, N. R., and White, S. R. (2010). Self-healing polymers and composites. *Annual Review of Materials Research*, 40(1):179–211.

[Builes Cárdenas et al., 2022] Builes Cárdenas, C., Gayraud, V., Rodriguez, M. E., Costa, J., Salaberria, A. M., Ruiz de Luzuriaga, A., Markaide, N., Dasan Keeryadath, P., and Calderón Zapatería, D. (2022). Study into the mechanical properties of a new aeronautic-grade epoxy-based carbon-fiber-reinforced vitrimer. *Polymers*, 14(6).

[Calderón-Villajos et al., 2019] Calderón-Villajos, R., López, A. J., Peponi, L., Manzano-Santamaría, J., and Ureña, A. (2019). 3d-printed self-healing composite polymer reinforced with carbon nanotubes. *Materials Letters*, 249:91–94.

[Chen et al., 2003] Chen, X., Wudl, F., Mal, A. K., Shen, H., and Nutt, S. R. (2003). New thermally remendable highly cross-linked polymeric materials. *Macromolecules*, 36(6):1802–1807.

[Cohades et al., 2018] Cohades, A., Branfoot, C., Rae, S., Bond, I., and Michaud, V. (2018). Progress in self-healing fiber-reinforced polymer composites. *Advanced Materials Interfaces*, 5(17):1800177.

[Cohades and Michaud, 2017a] Cohades, A. and Michaud, V. (2017a). Damage recovery after impact in e-glass reinforced poly(ε-caprolactone)/epoxy blends. *Composite Structures*, 180:439–447.

[Cohades and Michaud, 2017b] Cohades, A. and Michaud, V. (2017b). Thermal mending in e-glass reinforced poly(ε-caprolactone)/epoxy blends. *Composites Part A: Applied Science and Manufacturing*, 99:129–138.

[Coope et al., 2016] Coope, T. S., Turkenburg, D. H., Fischer, H. R., Luterbacher, R., van Bracht, H., and Bond, I. P. (2016). Novel diels-alder based self-healing epoxies for aerospace composites. *Smart Materials and Structures*, 25(8):084010.

[Da Via et al., 2022] Da Via, F., Suriano, R., Boumezgane, O., Grande, A. M., Tonelli, C., and Turri, S. (2022). Self–healing behavior in blends of pdms–based polyurethane ionomers. *Polymers for Advanced Technologies*, 33(2):556–565.

[Darabi et al., 2012a] Darabi, M. K., Abu Al-Rub, R. K., and Little, D. N. (2012a). A continuum damage mechanics framework for modeling micro-damage healing. *International Journal of Solids and Structures*, 49(3-4):492–513.

[Darabi et al., 2011] Darabi, M. K., Abu Al-Rub, R. K., Masad, E. A., Huang, C.-W., and Little, D. N. (2011). A thermo-viscoelastic–viscoplastic–viscodamage constitutive model for asphaltic materials. *International Journal of Solids and Structures*, 48(1):191–207.

[Darabi et al., 2012b] Darabi, M. K., Abu Al-Rub, R. K., Masad, E. A., and Little, D. N. (2012b). A thermodynamic framework for constitutive modeling of time- and rate-dependent materials. part ii: Numerical aspects and application to asphalt concrete. *International Journal of Plasticity*, 35:67–99.

[Darabi et al., 2012c] Darabi, M. K., Al-Rub, R. K. A., Masad, E. A., and Little, D. N. (2012c). Thermodynamic-based model for coupling temperature-dependent viscoelastic, viscoplastic, and viscodamage constitutive behavior of asphalt mixtures. *International Journal for Numerical and Analytical Methods in Geomechanics*, 36(7):817–854.

[Davies and Jefferson, 2017] Davies, R. and Jefferson, A. (2017). Micromechanical modelling of self-healing cementitious materials. *International Journal of Solids and Structures*, 113-114:180–191.

[Deschanel et al., 2009] Deschanel, S., Greviskes, B. P., Bertoldi, K., Sarva, S. S., Chen, W., Samuels, S. L., Cohen, R. E., and Boyce, M. C. (2009). Rate dependent finite

deformation stress–strain behavior of an ethylene methacrylic acid copolymer and an ethylene methacrylic acid butyl acrylate copolymer. *Polymer*, 50(1):227–235.

[Doghri et al., 2011] Doghri, I., Brassart, L., Adam, L., and Gérard, J.-S. (2011). A second-moment incremental formulation for the mean-field homogenization of elasto-plastic composites. *International Journal of Plasticity*, 27(3):352–371.

[European Space Agency, 2021] European Space Agency, . (2021.). About space debris.

[Fakirov, 2021] Fakirov, S. (2021). Once more on the proper use of terms and definitions: this time about the term 'self-healing'. *Express Polymer Letters*, 15(2):88.

[Feng and Li, 2021] Feng, X. and Li, G. (2021). Room-temperature self-healable and mechanically robust thermoset polymers for healing delamination and recycling carbon fibers. *ACS applied materials & interfaces*.

[Francesconi et al., 2013] Francesconi, A., Giacomuzzo, C., Grande, A. M., Mudric, T., Zaccariotto, M., Etemadi, E., Di Landro, L., and Galvanetto, U. (2013). Comparison of self-healing ionomer to aluminium-alloy bumpers for protecting spacecraft equipment from space debris impacts. *Advances in Space Research*, 51(5):930–940.

[Garcia, 2014] Garcia, S. J. (2014). Effect of polymer architecture on the intrinsic self-healing character of polymers. *European Polymer Journal*, 53:118–125.

[Goldberg, 1999] Goldberg, R. K. (1999). *Strain Rate Dependent Deformation and Strength Modeling of a Polymer Matrix Composite Utilizing a Micromechanics Approach*. Phd thesis, NASA Glenn Research Center Cleveland, Cleveland, Ohio.

[Gordon et al., 2016] Gordon, K., Smith, R. W., Working, D. C., and Siochi, E. J. (2016). Engineering polymer blends for impact damage mitigation. page 46.

[Guadagno et al., 2010] Guadagno, L., Longo, P., Raimondo, M., Naddeo, C., Mariconda, A., Sorrentino, A., Vittoria, V., Iannuzzo, G., and Russo, S. (2010). Cure behavior and mechanical properties of structural self-healing epoxy resins. *Journal of Polymer Science Part B: Polymer Physics*, 48(23):2413–2423.

[Guo et al., 2016] Guo, W., Jia, Y., Tian, K., Xu, Z., Jiao, J., Li, R., Wu, Y., Cao, L., and Wang, H. (2016). Uv-triggered self-healing of a single robust sio2 microcapsule

based on cationic polymerization for potential application in aerospace coatings. *ACS applied materials & interfaces*, 8(32):21046–21054.

[Haddad et al., 2019] Haddad, E., Zhao, Y., Celikin, M., Basti, M., Tagziria, K., Wallach, E., Semprimoschnig, C., Lafont, U., and McKenzie, I. (7122019). Mitigating the effect of space small debris on copv in space with fiber sensors monitoring and self–repairing materials. In Karafolas, N., Sodnik, Z., and Cugny, B., editors, *International Conference on Space Optics — ICSO 2018*, page 263. SPIE.

[Haramina et al., 2021] Haramina, T., Pugar, D., Ivančević, D., and Smojver, I. (2021). Mechanical properties of poly(ethylene-co-methacrylic acid) reinforced with carbon fibers. *Polymers*, 13(1).

[Hayes et al., 2007] Hayes, S. A., Zhang, W., Branthwaite, M., and Jones, F. R. (2007). Self-healing of damage in fibre-reinforced polymer-matrix composites. *Journal of the Royal Society, Interface*, 4(13):381–387.

[Hexcel, 2021] Hexcel (accessed on 6 April 2021.). http://www.lookpolymers.com/pdf/hexcel-hexforce-ga045-carbon-fabric.pdf.

[Inamuddin et al., 2021] Inamuddin, M. I. A., Rajender Boddula, and Tariq Altalhi, editors (2021). *Self–Healing Smart Materials and Allied Applications: Self-Healing Materials in Aerospace Applications*. Scrivener Publishing LLC.

[Janszen et al., 2019] Janszen, G., Capezzera, G., Grande, A., and Di Landro, L. (2019). Mitigation of impact damage with self-healing and anti-sloshing materials in aerospace fuel tanks. *Aerospace*, 6(2):14.

[K. Gordon, R. Penner, P. Bogert, W.T. Yost and E. Siochi, 2011] K. Gordon, R. Penner, P. Bogert, W.T. Yost and E. Siochi, editor (2011). *Puncture Self-healing Polymers for Aerospace Applications*.

[Kachanov, 1958] Kachanov, L. M. (1958). Rupture time under creep conditions. *International Journal of Fracture*, 97(1/4):11–18.

[Kalista and Ward, 2007] Kalista, S. J. and Ward, T. C. (2007). Thermal characteristics of the self-healing response in poly(ethylene-co-methacrylic acid) copolymers. *Journal of the Royal Society, Interface*, 4(13):405–411.

[Kanu et al., 2019] Kanu, N. J., Gupta, E., Vates, U. K., and Singh, G. K. (2019). Self-healing composites: A state-of-the-art review. *Composites Part A: Applied Science and Manufacturing*, 121:474–486.

[Keller and Crall, 2018] Keller, M. W. and Crall, M. D. (2018). 6.15 self-healing composite materials. In *Comprehensive Composite Materials II*, pages 431–453. Elsevier.

[Kostopoulos et al., 2020] Kostopoulos, V., Kotrotsos, A., Geitona, A., and Tsantzalis, S. (2020). Low velocity impact response and post impact assessment of carbon fiber/epoxy composites modified with diels-alder based healing agent. a novel approach. *Composites Part A: Applied Science and Manufacturing*, 140:106151.

[Kostopoulos et al., 2019] Kostopoulos, V., Kotrotsos, A., Sousanis, A., and Sotiriadis, G. (2019). Fatigue behaviour of open-hole carbon fibre/epoxy composites containing bis-maleimide based polymer blend interleaves as self-healing agent. *Composites Science and Technology*, 171:86–93.

[Kostopoulos et al., 2016a] Kostopoulos, V., Kotrotsos, A., Tsantzalis, S., Tsokanas, P., Christopoulos, A. C., and Loutas, T. (2016a). Toughening and healing of continuous fibre reinforced composites with bis-maleimide based pre-pregs. *Smart Materials and Structures*, 25(8):1–12.

[Kostopoulos et al., 2016b] Kostopoulos, V., Kotrotsos, A., Tsantzalis, S., Tsokanas, P., Loutas, T., and Bosman, A. W. (2016b). Toughening and healing of continuous fibre reinforced composites by supramolecular polymers. *Composites Science and Technology*, 128:84–93.

[Kostopoulos et al., 2018] Kostopoulos, V., Kotrotsos, A., Tsokanas, P., and Tsantzalis, S. (2018). Toughening and healing of composites by cnts reinforced copolymer nylon micro-particles. *Materials Research Express*, 5(2):1–14.

[Kotrotsos et al., 2019] Kotrotsos, A., Tsokanas, P., Tsantzalis, S., and Kostopoulos, V. (2019). Healing of carbon fiber reinforced plastics by diels–alder based polymers: Effects of healing agent concentration and curing cycle. *Journal of Applied Polymer Science*, 136(19):1–12.

[Kumar et al., 2006] Kumar, A., Stephenson, L. D., and Murray, J. N. (2006). Self-healing coatings for steel. *Progress in Organic Coatings*, 55(3):244–253.

[Lapczyk and Hurtado, 2007] Lapczyk, I. and Hurtado, J. A. (2007). Progressive damage modeling in fiber-reinforced materials. *Composites Part A: Applied Science and Manufacturing*, 38(11):2333–2341.

[László P. Kollár, George S. Springer, 2003] László P. Kollár, George S. Springer (2003). *Mechanics of composite Structures*. Cambridge University Press.

[Long et al., 2021] Long, S., Mu, X., Liu, Y., Wang, H., Zhang, X., and Yao, X. (2021). Failure modeling of composite wing leading edge under bird strike. *Composite Structures*, 255:113005.

[Lumley et al., 2002] Lumley, R. N., Morton, A. J., and Polmear, I. J. (2002). Enhanced creep performance in an al–cu–mg–ag alloy through underageing. *Acta Materialia*, 50(14):3597–3608.

[Michele Viola Manuel, 2007] Michele Viola Manuel (2007). *Design of a Biomimetic Self-Healing Alloy Composite*. PhD thesis, NORTHWESTERN UNIVERSITY, EVANSTON, ILLINOIS.

[Miqoi et al., 2021] Miqoi, N., Pomarede, P., Meraghni, F., Declercq, N. F., Guillaumat, L., Le Coz, G., and Delalande, S. (2021). Detection and evaluation of barely visible impact damage in woven glass fabric reinforced polyamide 6.6/6 composite using ultrasonic imaging, x-ray tomography and optical profilometry. *International Journal of Damage Mechanics*, 30(3):323–348.

[Nakao, 2013] Nakao, W., editor (2013). *Advanced Self-Healing Ceramics for Turbine Blade*. American Society of Mechanical Engineers.

[Oucif et al., 2019] Oucif, C., Voyiadjis, G. Z., Kattan, P. I., and Rabczuk, T. (2019). Investigation of the super healing theory in continuum damage and healing mechanics. *International Journal of Damage Mechanics*, 28(6):896–917.

[Paladugu et al., 2022] Paladugu, S. R. M., Sreekanth, P. S. R., Sahu, S. K., Naresh, K., Karthick, S. A., Venkateshwaran, N., Ramoni, M., Mensah, R. A., Das, O., and

Shanmugam, R. (2022). A comprehensive review of self-healing polymer, metal, and ceramic matrix composites and their modeling aspects for aerospace applications. *Materials (Basel, Switzerland)*, 15(23).

[Paolillo et al., 2021] Paolillo, S., Bose, R. K., Santana, M. H., and Grande, A. M. (2021). Intrinsic self-healing epoxies in polymer matrix composites (pmcs) for aerospace applications. *Polymers*, 13(2).

[Park et al., 2010] Park, J. S., Darlington, T., Starr, A. F., Takahashi, K., Riendeau, J., and Thomas Hahn, H. (2010). Multiple healing effect of thermally activated self-healing composites based on diels–alder reaction. *Composites Science and Technology*, 70(15):2154–2159.

[Pernigoni and Grande, 2020] Pernigoni, L. and Grande, A. M. (2020). Development of a supramolecular polymer based self-healing multilayer system for inflatable structures. *Acta Astronautica*, 177:697–706.

[Pernigoni et al., 2021] Pernigoni, L., Lafont, U., and Grande, A. M. (2021). Self-healing materials for space applications: overview of present development and major limitations. *CEAS Space Journal*, 13(3):341–352.

[Pingkarawat et al., 2012] Pingkarawat, K., Wang, C. H., Varley, R. J., and Mouritz, A. P. (2012). Self-healing of delamination cracks in mendable epoxy matrix laminates using poly[ethylene-co-(methacrylic acid)] thermoplastic. *Composites Part A: Applied Science and Manufacturing*, 43(8):1301–1307.

[Post et al., 2017] Post, W., Cohades, A., Michaud, V., van der Zwaag, S., and Garcia, S. J. (2017). Healing of a glass fibre reinforced composite with a disulphide containing organic-inorganic epoxy matrix. *Composites Science and Technology*, 152:85–93.

[Raimondo et al., 2016] Raimondo, M., de Nicola, F., Volponi, R., Binder, W., Michael, P., Russo, S., and Guadagno, L. (2016). Self-repairing cfrps targeted towards structural aerospace applications. *International Journal of Structural Integrity*, 7(5):656–670.

[Rana and Fangueiro, 2016] Rana, S. and Fangueiro, R., editors (2016). *Advanced Composite Materials for Aerospace Engineering: Processing, Properties and Applications*,

volume number 62 of *Woodhead Publishing series in composites science and engineering*. Elsevier/WP Woodhead Publishing, Amsterdam and Boston and Cambridge.

[Reynolds, 2011] Reynolds, P. J. (2011). *A Surlyn® Ionomer as a Self-Healing and Self-Sensing Composite*. Mres thesis, University of Birmingham, Birmingham, United Kingdom.

[Sanz-Herrera et al., 2019] Sanz-Herrera, J. A., Aliko-Benitez, A., and Fadrique-Contreras, A. M. (2019). Numerical investigation of the coupled mechanical behavior of self-healing materials under cyclic loading. *International Journal of Solids and Structures*, 160:232–246.

[Shabani et al., 2020] Shabani, P., Shokrieh, M. M., and Saeedi, A. (2020). A novel model to simulate the formation and healing of cracks in self-healing cross-ply composites under flexural loading. *Composite Structures*, 235:1–11.

[Smojver et al., 2022a] Smojver, I., Brezetić, D., and Ivančević, D. (2022a). Explicit multi-scale modelling of intrinsic self-healing after low-velocity impact in gfrp composites. *Composite Structures*, 302:116213.

[Smojver and Ivančević, 2010] Smojver, I. and Ivančević, D. (2010). Numerical simulation of bird strike damage prediction in airplane flap structure. *Composite Structures*, 92(9):2016–2026.

[Smojver and Ivančević, 2011] Smojver, I. and Ivančević, D. (2011). Bird strike damage analysis in aircraft structures using abaqus/explicit and coupled eulerian lagrangian approach. *Composites Science and Technology*, 71(4):489–498.

[Smojver and Ivančević, 2012] Smojver, I. and Ivančević, D. (2012). Advanced modelling of bird strike on high lift devices using hybrid eulerian–lagrangian formulation. *Aerospace Science and Technology*, 23(1):224–232.

[Smojver et al., 2022b] Smojver, I., Ivančević, D., and Brezetić, D. (2022b). Modelling of micro-damage and intrinsic self-healing in unidirectional cfrp composite structures. *Composite Structures*, 286:115266.

[Smojver et al., 2022c] Smojver, I., Ivančević, D., Brezetić, D., and Haramina, T. (2022c). Constitutive modelling of a self-healing composite matrix polymer material. *International Journal of Damage Mechanics*, page 105678952210956.

[Sordo and Michaud, 2016] Sordo, F. and Michaud, V. (2016). Processing and damage recovery of intrinsic self-healing glass fiber reinforced composites. *Smart Materials and Structures*, 25(8):084012.

[Subramanian and Mulay, 2020] Subramanian, H. and Mulay, S. S. (2020). Continuum damage–healing-based constitutive modelling for self-healing materials: application to one-dimensional cyclic loading cases. *International Journal of Advances in Engineering Sciences and Applied Mathematics*, 12(1-2):3–18.

[Swapan Kumar Ghosh, 2009] Swapan Kumar Ghosh, editor (2009). *Self-healing Materials - Fundamentals, Design Strategies and Applications*. Wiley-VCH, Weinheim.

[Teoh et al., 2010] Teoh, S. H., Chia, H. Y., Lee, M. S., Nasyitah, A. J. N., Luqman, H. B. S. M., Nurhidayah, S., and Tan, W. C. K. (2010). Self healing composite for aircraft's structural application. *International Journal of Modern Physics B*, 24(01n02):157–163.

[Udhayaraman et al., 2020] Udhayaraman, R., Subramanian, H., Mulay, S. S., and Venkatachalam, S. (2020). Multi-scale approach-based studies on the damage-healing and fracture behavior of plain woven textile composite. *Mechanics of Advanced Materials and Structures*, pages 1–26.

[Varley and van der Zwaag, 2008] Varley, R. J. and van der Zwaag, S. (2008). Towards an understanding of thermally activated self-healing of an ionomer system during ballistic penetration. *Acta Materialia*, 56(19):5737–5750.

[Voyiadjis et al., 2020] Voyiadjis, G. Z., Oucif, C., Kattan, P. I., and Rabczuk, T. (2020). Damage and healing mechanics in plane stress, plane strain, and isotropic elasticity. *International Journal of Damage Mechanics*, 29(8):1246–1270.

[Voyiadjis et al., 2011] Voyiadjis, G. Z., Shojaei, A., and Li, G. (2011). A thermodynamic consistent damage and healing model for self healing materials. *International Journal of Plasticity*, 27(7):1025–1044.

[Voyiadjis et al., 2012a] Voyiadjis, G. Z., Shojaei, A., and Li, G. (2012a). A generalized coupled viscoplastic–viscodamage–viscohealing theory for glassy polymers. *International Journal of Plasticity*, 28(1):21–45.

[Voyiadjis et al., 2012b] Voyiadjis, G. Z., Shojaei, A., Li, G., and Kattan, P. I. (2012b). A theory of anisotropic healing and damage mechanics of materials. *Proceedings of the Royal Society A: Mathematical, Physical and Engineering Sciences*, 468(2137):163–183.

[Wang et al., 2012] Wang, C. H., Sidhu, K., Yang, T., Zhang, J., and Shanks, R. (2012). Interlayer self-healing and toughening of carbon fibre/epoxy composites using copolymer films. *Composites Part A: Applied Science and Manufacturing*, 43(3):512–518.

[Wang et al., 2021] Wang, S., Fu, D., Wang, X., Pu, W., Martone, A., Lu, X., Lavorgna, M., Wang, Z., Amendola, E., and Xia, H. (2021). High performance dynamic covalent crosslinked polyacylsemicarbazide composites with self-healing and recycling capabilities. *Journal of Materials Chemistry A*, 9(7):4055–4065.

[Wang et al., 2018] Wang, X., Li, Y., Qian, Y., Qi, H., Li, J., and Sun, J. (2018). Mechanically robust atomic oxygen-resistant coatings capable of autonomously healing damage in low earth orbit space environment. *Advanced materials (Deerfield Beach, Fla.)*, page e1803854.

[Williams, 2017] Williams, M. K. (February 22-24, 2017). Self-healing technologies for wiring and surfaces in aerospace and deep space exploration applications.

[Wu et al., 2022] Wu, X. S., Chen, T. Z., Wang, B. J., Song, Y. J., Huang, Q., and Huang, Z. R. (2022). Preparation of self-healing cf/sibcn(o) composite using a novel polyborosilazane. *Ceramics International*, 48(21):31738–31745.

[Yang et al., 2020] Yang, X., Guo, L., Xu, X., Shang, S., and Liu, H. (2020). A fully bio-based epoxy vitrimer: Self-healing, triple-shape memory and reprocessing triggered by dynamic covalent bond exchange. *Materials & Design*, 186:108248.

[Zhang et al., 2018] Zhang, L., Tian, X., Malakooti, M. H., and Sodano, H. A. (2018). Novel self-healing cfrp composites with high glass transition temperatures. *Composites Science and Technology*, 168:96–103.

[Zhao et al., 2019] Zhao, Y. Q., Zhou, Y., Huang, Z. M., and Batra, R. C. (2019). Experimental and micromechanical investigation of t300/7901 unidirectional composite strength. *Polymer Composites*, 40(7):2639–2652.

[Zhu et al., 2019] Zhu, Y., Cao, K., Chen, M., and Wu, L. (2019). Synthesis of uv-responsive self-healing microcapsules and their potential application in aerospace coatings. *ACS applied materials & interfaces*, 11(36):33314–33322.